Experimental Study of Ultra-Wideband Radio Propagation for Wireless Body Area Networks

ワイヤレスボディエリアネットワークのための超広帯域電波伝搬の実験的研究

A dissertation submitted in partial fulfillment of the requirement for the degree of

doctor of engineering

at

Tokyo Denki University

by

Hironobu YAMAMOTO

山本　浩延

March 2015

Contents

List of Abbreviations

AIC	-	Akaike information criterion
APDP	-	average power delay profile
CDF	-	cumulative density function
EIRP	-	effective isotropic radiation power
FCC	-	Federal Communications Commission
ICT	-	information and communication technology
IEEE	-	the Institute of Electrical and Electronics Engineers
IFT	-	inverse Fourier transform
LOS	-	line-of-sight
NLOS	-	non-line-of-sight
PHY	-	physical layer
RFID	-	radio frequency identifier
rms	-	root mean square
Rx	-	receiver
SAR	-	specific absorption rate
SV	-	Saleh-Valenzuela
TE	-	transverse-electric
TM	-	transverse-magnetic
Tx	-	transmitter
USB	-	universal serial bus
UWB	-	ultra-wideband
VNA	-	vector network analyzer
VSWR	-	voltage standing wave ratio
WBAN	-	wireless body area network
WLAN		wireless local area network
WPAN	-	wireless personal area network

Chapter 1
Introduction

1.1   Overview of UWB Technology

Ultra-wideband (UWB) technology is a candidate for use in short-range wireless systems providing connectivity by employing different types of communication links, services, and applications [1]-[3]. A generic definition used in the FCC's *First Report and Order* [4] defines a UWB device as any device emitting signals with a fractional bandwidth greater than 0.2 or a bandwidth of at least 500 MHz at all times of transmission. The fractional bandwidth is defined as

$$\frac{2(f_H - f_L)}{f_H + f_L} \times 100 > 20 \ [\%], \tag{1.1}$$

where f_H and f_L are the upper and the lower frequencies at the -10 dB emission point. At the physical layer (PHY) level, UWB communication systems operate by spreading smaller amounts of average effective isotropic radiation power (EIRP) across a very wide band of frequencies relative to the center frequency. The EIRP is always less than 0.56 mW, according to FCC masks. This quantity is easily calculated from the imposed power spectral density limit of -41.3 dBm/MHz between 3.1 GHz and 10.6 GHz. The frequency allocation in Japan was defined by the Ministry of Internal Affairs and Communications in March 2006 [5]. Different countries have adopted somewhat different UWB spectrum masks, as shown in Fig. 1.1. A bandwidth from 3.1 to 10.6 GHz, referred to as a full-band UWB, has been approved in the United States (US) and Singapore. Most countries and regions including Europe and Japan impose stricter regulation than the US: low- and high-band UWB as depicted in Fig. 1.1. The frequency allocation and often the conditions differ slightly from country to country. Inherent in these UWB definitions is a high temporal resolution that not only allows the design of radio systems with much lower fading margins than classical narrowband systems, but also enables precision ranging capabilities combined with data transmission. The effects of multipath fading for UWB Systems can be found in [6] and [7].
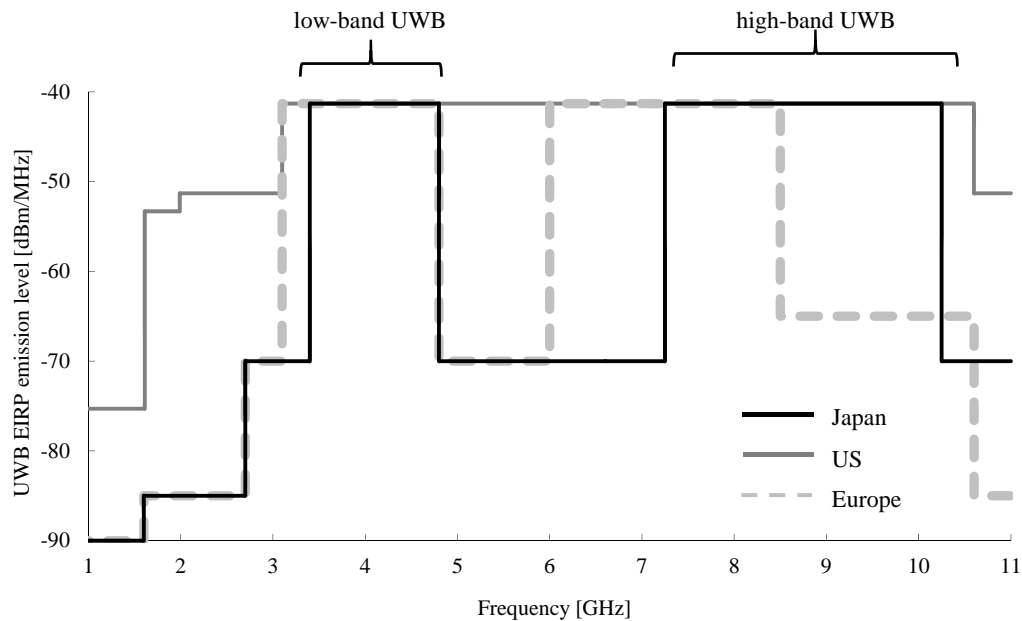
Fig. 1.1.   The UWB spectrum mask.

UWB has been developed as a short-range, ultra-low power technology with an extremely small signal range. It has been claimed that it has an accuracy of between 100 and 300 mm, and that this will have broad applications in the automotive and other industries. There are rivals in this field including Bluetooth Low Energy and the humble radio frequency identifier (RFID). UWB can support higher data rates than these technologies – a decade ago, it offered a promising solution for a standardization of short-range home media networks or wireless universal serial bus (USB) – but many tracking applications requiring micro-location do not need high-speed transmission. There is an expectation that UWB technology will be employed for wireless personal area network (WPAN) standardization, although WPAN standards have shifted toward more conventional approaches like wireless local area networks (WLAN). UWB, however, has retained a presence in military and security markets, where its location awareness is prized and the issues of cost and standardization are less important. In recent years, sensor applications, used, for example, to track assets in warehouses, to analyze the field positions of soccer players, or to improve productivity in assembly lines, etc., have been developed by making use of features of UWB's precise positioning. Now the UWB focus is firmly back on applications which prioritize precise positioning and ultra-low power rather than high data rates. Hence, the IEEE

802.15.6 standard for wireless body area networks (WBAN) has been published to obtain the same range and speed as Bluetooth but with lower power consumption and interference potential.

1.2 Wireless Body Area Networks

It is recognized that the growing global population is also an aging one. This trend, coupled with the daily developments in new diagnostic techniques and other advances in medicine, will place an increasing demand on medical and healthcare resources. In 2010, there were more than 530 million people in the world over the age of 65, a number that will double over the next 30 years [8]. In the US, about 20% of the population will be over 65 by 2030, compared to 13% today [8]. Similarly, about 32% of the Japanese population will be over 65 by 2030, compared to 23% today [8], as shown in Fig. 1.2. Furthermore, developing nations as well as developed ones will become aging societies.

The rapidly growing population of elderly people will result in an increase of chronic diseases and will require more efficient healthcare management. The modern technologies, including electronics, mechanics, semi-conductors, and networks, can provide support in different ways. Among these technologies, information and communication technology (ICT) has potential applications in medical services. As an emerging ICT technology, WBAN has attracted significant attention in recent years and is expected to be able to provide distinct solutions in supporting medical and healthcare services. WBAN refers to human-self and human-to-human networking with the use of wearable and implantable wireless sensors. Skin surface monitors of vital signs are now integrated with wireless communications and medical implants with links to local base stations are being developed [9], [10]. The human body is an uninviting and often hostile environment for a wireless signal. Therefore, performance investigations of antennas and propagation models will be of key importance in developing WBAN systems.

The topic of WBAN can be divided into three domains: 1) communications from the body surface to a nearby base station; 2) transmitting and receiving antennas on the body surface; and 3) the use of at least one antenna in a medical implant within the body. These three domains have been called off-body, on-body, and in-body, respectively. Figure 1.3 describes these WBAN domains. The IEEE Standard for local and metropolitan area networks – Part 15.6: Wireless Body Area Networks (IEEE Std 802.15.6, 2012) was approved in February 2012. In the IEEE Std. 802.15.6-2012, UWB has been defined as one of the main PHYs.
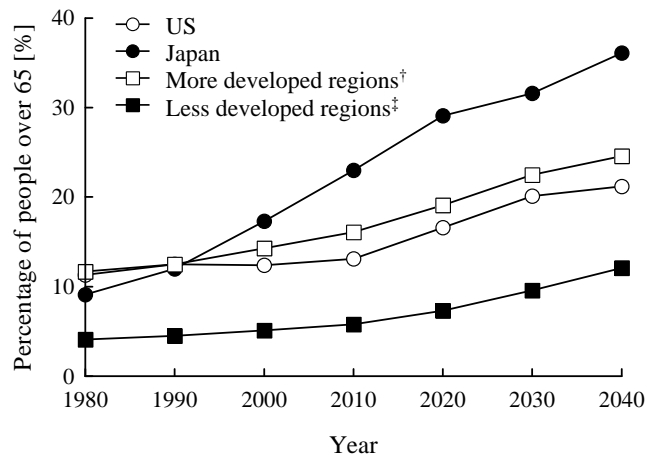
(a)
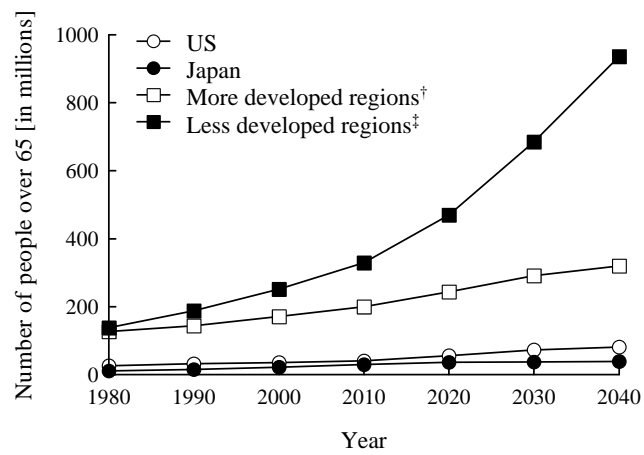
(b)

Fig. 1.2. Diagrams illustrating the growth of the section of the population aged over 65 since 1980 in the US, Japan, more developed, and less developed, regions with projections to 2040: (a) number of people and (b) as a percentage of the population.

†: More developed regions comprise Europe, North America, Australia/New Zealand and Japan.

‡: Less developed regions comprise all the regions of Africa, Asia (except Japan), Latin America and the Caribbean plus Melanesia, Micronesia and Polynesia.
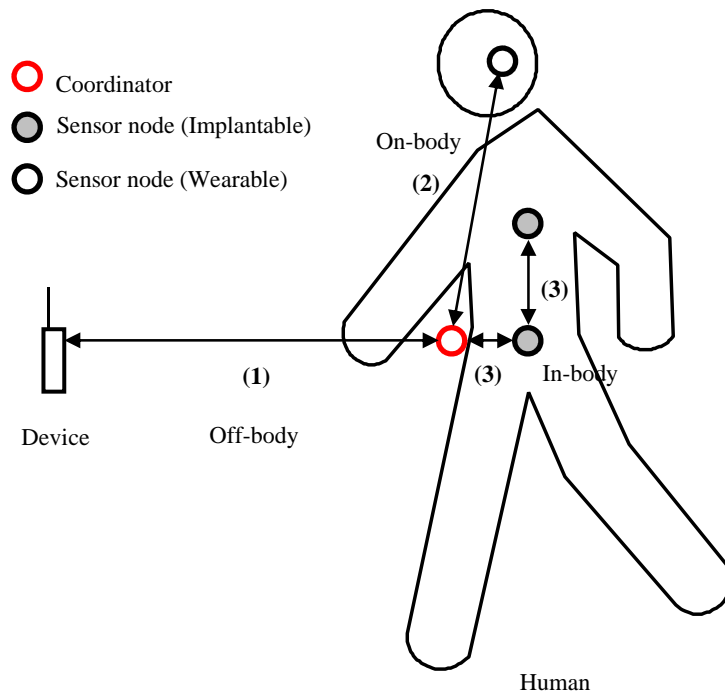
4

Fig. 1.3.   The domains of WBAN; 1) communications from the body surface to a nearby base station; 2) both antennas on the body surface; and 3) at least one antenna in a medical implant within the body.

1.3 Historical Perspective of UWB Radio Propagation Envisioned for WBAN

There is an increasing interest in UWB communications for new wireless systems because of their low power consumption and anti-multipath capabilities [11]. One of the most promising systems utilizing UWB is WBAN. WBAN is of vital importance for new medical applications, such as wireless electroencephalography, electrocardiography, and electromyography; and other instances of health care monitoring [10]. Numerous studies have been carried out on UWB propagation characterization and the modeling of indoor UWB communication channels [12]. A number of measurements relating to WBAN have also been performed to characterize UWB radio propagation.

Phantoms, which are models simulating various electrical constants of biological tissues, are used to evaluate the antenna characteristics of mobile terminals as well as to measure the amounts of absorbed electromagnetic energy. Liquid, semi-liquid, and solid electromagnetic phantom materials have been developed in high-frequency to super-high-frequency bands in a relatively narrow bandwidth [13]-[15] for the assessment of specific absorption rates (SAR) by a human body and experimental evaluation of the effect of human bodies on antenna performance and propagation.

Previously, UWB radio propagation performances around the human body have been measured in either a radio anechoic chamber or a specific room type [16]-[27]. Table 1.1 summarizes these publications. A UWB propagation loss model and channel models have been proposed on the basis of these measurement campaigns.

Several papers have so far investigated the in-body channel characteristics for wireless capsule endoscopy [28]-[30]. UWB radio propagation performances through the human chest have been characterized by electromagnetic simulation and the channel model has been investigated [31], [32]. The performances of UWB transmission in a living animal (pig) have also been evaluated [33].

Table 1.1　Previous publications reporting UWB propagation studies for WBAN.

Measurements environment	Reference	Summary
A radio anechoic chamber	[16]	・ UWB on-body channel measurements ・ Tx was placed on trunk (front side of body). Rx was placed on either head, chest or arm. Twenty-two different on-body scenarios applied in the measurement (*e .g.* standing still, body turned left, body leaned forward). ・ Channel models with respect to large scale and delay analysis have been derived from measured parameters.
	[17]	・ UWB on-body radio channel modelling using a sub-band Finite-Difference Time-Domain method and a model combining the uniform geometrical theory of diffraction and raytracing. ・ Tx was placed on trunk (front side of body). Rx was placed on either head, chest or arm.
	[18]	・ Develops a two dimensional statistical-based path-loss model in off-body UWB communication
An indoor environment	[19]	・ On-body UWB communication characterization and channel modeling. ・ The body is in a standing position. ・ Tx is placed on the front of the body and Rx is placed at various positions on the torso at distances of 10 – 45 cm.
	[20]	・ UWB performance and complexity tradeoffs for RAKE receivers evaluated on body area propagation channels.
	[21]	・ On-body propagation statistics and proposes a suitable computer model implementation. ・ Focused on statistics measured due to diffraction around the torso and reflection off the ground.
	[22]	・ Measured path loss around the torso and arm. ・ Measured amount of energy received due to reflections off the ground and surrounding scatters in a typical environment.
A radio anechoic chamber and an indoor environment	[23]	・ Measurements on the front side of the body and measurements around the upper torso ・ Channel parameters as delay spread and path loss are extracted from the measurements and the influence of the body is highlighted. ・ Considers the overall energy consumption of the BAN and gives decision regions for singlehop and multihop links in relation to signal processing energy.
	[24]	・ Measurements on the front side of the body and measurements around the upper torso ・ Return loss and radiation patterns, the transient analysis in free space. ・ Root mean square (RMS) delay spreads were calculated from the measurements in an indoor environment.

1.4   Statement of the Problem

Phantoms are used for performance evaluation of antennas mounted in the vicinity of a human body and channel assessment when a human body blocks a propagation path. Publications on UWB phantoms have been limited to assessments of SAR, and hence there is no phantom with which to evaluate the characteristics of UWB radio propagation. It is necessary to develop a liquid UWB phantom to measure and evaluate the radio propagation characteristics.

Previous UWB propagation loss models and channels are mainly based on measurement campaigns in a radio anechoic chamber, and these studies did not consider the impact of surrounding environments. WBAN devices will be surface-mounted on the body in everyday life, and the major users of WBAN applications will move through different-sized rooms; from large rooms (e.g. a stadium, a museum, and a cathedral) to small rooms (e.g. an elevator, a toilet, and a passenger car). The characteristics of multipath components (mainly reflected from floor, ceiling, and walls) are highly dependent on the environment. It is necessary to evaluate the variation of propagation characteristics in various rooms.

This thesis is, therefore, mainly focused on the following two themes:

· The development of a UWB phantom and the characterization of UWB radio propagation for off-body communications.

· Measurements and modeling of UWB radio propagation around the human body in five different room-sizes.

This research is organized into the following six Chapters.

Chapter 1 provides an outline of UWB technology, WBAN, the historical perspective of UWB radio propagation studies for WBAN, and a statement of the problem.

Chapter 2 presents preliminary studies of the UWB radio propagation measurements envisioned for WBAN; the development of UWB phantom material and a consideration of antenna feeding cable configurations. In WBAN scenarios, a human body often blocks a propagation path, and the effects of human bodies on antenna performance and propagation have become vital concerns. UWB human electromagnetic phantoms are useful for the performance evaluation of antennas installed in the vicinity of a human body.

Electrically small antennas were mostly used since the actual wireless devices for WBAN applications are battery-powered and compact in WBAN campaigns. Such small antennas exhibit a relatively large voltage standing wave ratio (VSWR) and often emit radiation not only from the antennas themselves but also from the outer conductors of the feeding coaxial cables. The effects of the feeding cable configuration on WBAN propagation were measured and a suitable configuration was proposed.

Chapter 3 presents measurements and a characterization of UWB propagation channels between a base station and on-/off-body antennas. First, a desktop environment in which a human arm blocks the radio propagation was considered. Next, the radio propagation characteristics between a base station antenna and an antenna mounted on a human torso were measured and analyzed. Arm and torso phantoms were used for these measurements and evaluated in comparison with a real human body.

Chapter 4 presents measurements and modeling of UWB propagation losses around the human body considering the impact of the volume of the room where WBAN was used. The UWB propagation losses were measured in five different-sized rooms. Propagation losses were found to decrease with decreasing room volume. A larger number of multipath components impinged on the receiving antenna from the nearby floor, walls, and ceiling in smaller rooms. A conventional UWB propagation loss model was modified to include the impact of the room volume and the parameters were derived from the data collected in the five rooms. Probability distributions for the UWB propagation losses around the human body were also considered.

Chapter 5 describes the statistical modeling of UWB propagation channels around the human body in various surrounding environments. Delay profiles were modeled by dividing into two domains: in the first time domain ($0 < t \leq 4$ ns) there is either a direct (for line-of-sight (LOS)) or diffracted (for non-LOS (NLOS)) wave essentially unrelated to room volume, and in the second domain ($t > 4$ ns) there are multipath components that are dominant and dependent on room volume. The first domain was modeled with a conventional power decay law model, and the second domain with a Saleh-Valenzuela (SV) (statistical) model, based on a cluster concept of rays, modified to take account of the room volume. Realizations of the impulse responses are presented on the basis of a composite model of the two domains and compared with the measured average power delay profiles (APDPs).

Finally, **Chapter 6** summarizes the concluding remarks given in the previous chapters and discusses future research topics.

Chapter 2
Preliminary Studies of UWB Radio Propagation Measurements for WBAN

2.1 Development of UWB Phantom Material

Liquid, semi-liquid, and solid electromagnetic phantom materials have been developed in high-frequency to super-high-frequency bands in a relatively narrow bandwidth [13]-[15] for the assessment of SAR in a human body exposed to electromagnetic waves. The series of narrowband commercially-available liquid phantom materials covers a range from 10 MHz to 5.2 GHz [34]. A solid UWB electromagnetic phantom material has been developed for the assessment of SAR within a bandwidth of between 3 and 6 GHz [35]. In a previous study Kobayashi et al. [36] developed a liquid UWB phantom material. These phantom materials simulate the complex relative permittivity $\dot{\varepsilon} = \varepsilon' - j\varepsilon''$ of human body tissues. Human tissues are electromagnetically divided into two categories: high-water-content tissues (skin, muscles, internal organs, and brain) and low-water-content tissues (bones and hair). The ε' and ε'' of high-water-content tissues in the microwave frequency band range from 30 to 50 and from 15 to 25, respectively. These values are significantly higher than those for common dielectrics, and thus are relatively difficult to realize artificially. The liquid phantom materials have been developed to simulate the complex relative permittivity of high-water-content tissues. The effects of errors in realizing $\dot{\varepsilon}$ of muscle were analytically evaluated, by assuming typical shapes for reflecting and scattering objects.

2.1.1 Liquid Phantom Material

Liquid UWB phantom materials simulate the complex relative permittivity $\dot{\varepsilon}$ of high-water-content tissues (for example, muscle), for which data were given by Gabriel et al. [37]. A search was carried out to find the optimal recipe among solutions containing sucrose, sodium chloride, and several monohydric and polyhydric alcohols. A mixture of saline water and ethylene glycol successfully simulates the electric property of high-water-content tissues at narrowband

UHF [13]. According to [13], $\dot{\varepsilon}$ for this recipe was measured with an Agilent 85070D dielectric probe kit (an open-ended coaxial probe [38]) at a bandwidth of 2 to 11 GHz, as shown in Fig. 2.1. The measured values of ε' and ε'' deviated from those for muscle [37], and so this mixture recipe was considered unsuitable for UWB. Among the recipes investigated, an aqueous solution of sucrose ($C_{12}H_{22}O_{11}$, 1.0 mol = 3.4 kg) provided the best results within a UWB bandwidth of 3.1 to 10.6 GHz [36], as shown in Fig. 2.2. Typical measurement accuracy was within 5%. The repeatability of the measurement results was typically less than 2%. This material can be easily and inexpensively produced. It can also be disposed of as domestic waste because it contains no toxic agents.
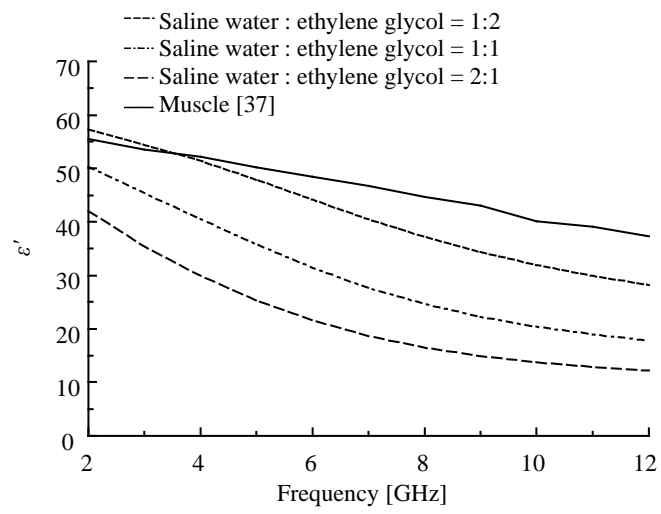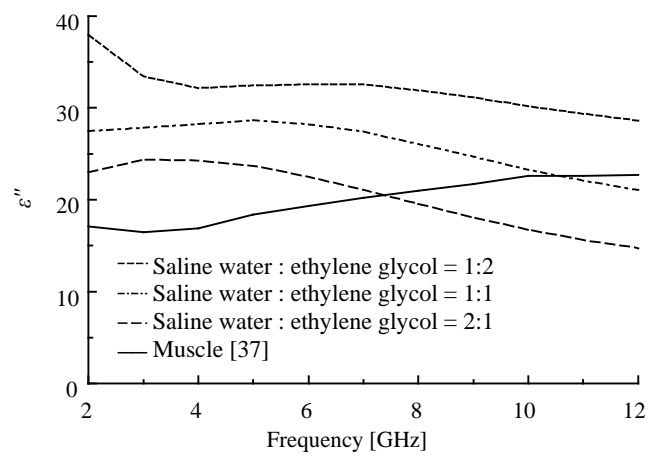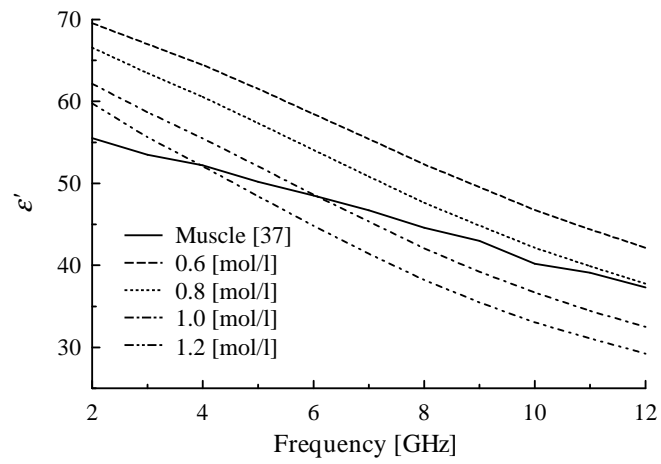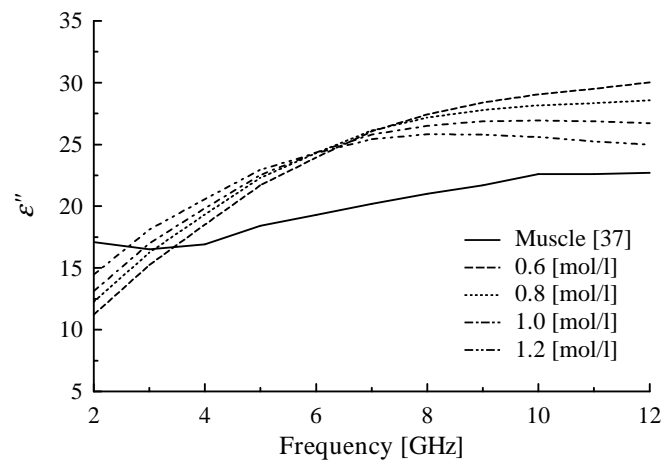
Fig. 2.1. Complex relative permittivity of muscle and a mixture of saline water (1.0 mol/l) and ethylene glycol: (a) ε' and (b) ε''.

(a)

(b)

Fig. 2.2. Complex relative permittivity of muscle and aqueous solution of sucrose: (a) ε' and (b) ε''.

2.1.2 Evaluation of the Liquid Material

The errors in ε' and ε'' for the 1.0-mol/l aqueous solution of sucrose were evaluated in comparison with those for muscle [37]. The error at frequencies of between 2 and 12 GHz is given by

$$e_y(x_i) = \frac{y_{\text{phantom}}(x_i) - y_{\text{muscle}}(x_i)}{y_{\text{phantom}}(x_i)} \times 100 \, [\%], \qquad (2.1)$$

where y is either ε' or ε'' and x_i is i-th f_i ($2 \leq f_i \leq 12$ GHz). The rms errors over a specified bandwidth are given by

$$e_{y,\text{rms}} = \sqrt{\frac{1}{N} \sum_{i=1}^{N} |e_y(x_i)|^2}, \qquad (2.2)$$

where y is either ε' or ε'', x_i is i-th f_i ($2 \leq f_i \leq 12$ GHz), and N is the number of samples.

The maximum and rms errors between 2 and 12 GHz were 12% maximal at 2.0 GHz and 8.5% rms in ε'; and 28% maximal at 7.0 GHz and 21.5% rms in ε''. Although the maximum errors were relatively large, the rms errors were found to be tolerably small, considering the typical measurement accuracies of around 5%.

Reflection and scattering from homogeneous dielectric media in typical shapes (an infinite plane, a sphere, and an infinite cylinder) were calculated to evaluate the effect of these errors on the phantom performances, assuming a plane wave (either transverse-electric (TE) or transverse-magnetic (TM)) incidence. If a spherical wave and/or near-field incidence is assumed, the radiation characteristics and position of the antenna should be specified, and this may reduce the generality. Therefore, a simple plane wave incidence was assumed in this evaluation.

The UWB power reflection coefficient [36] from an infinite plane is defined by

$$|R_{\text{UWB}}(\theta)|^2 = \frac{1}{f_h - f_l} \int_{f_l}^{f_h} |\dot{R}(\theta, f)|^2 \, df, \qquad (2.3)$$

where $\dot{R}(\theta, f)$ is the complex Fresnel reflection coefficient at an incident angle of θ and at a frequency of f, and f_l and f_h are the lowest and highest frequencies. Note that $0 \leq |R_{\text{UWB}}(\theta)|^2 \leq 1$. The effects of typical errors in the complex relative permittivity on the reflection behaviors were numerically evaluated [36]. The maximum and rms errors in the UWB reflection coefficients were almost negligible when the errors in $\dot{\varepsilon}$ were within 30% (see Appendix A).

The UWB power scattering coefficient [36] from a sphere or a cylinder is defined by

$$S_{\text{UWB}}(\phi) = \frac{\int_{f_l}^{f_h} \left| \dot{S}(\phi, f) \right|^2 df}{\int_{f_l}^{f_h} \left| \dot{S}(180°, f) \right|^2 df} \, ,$$
(2.4)

where $\dot{S}(\phi, f)$ is the complex scattering amplitude at a scattering angle of ϕ and at a frequency of f. The UWB power scattering coefficient $\dot{S}$ is normalized by the UWB backscattering power ($\phi = 180°$), so that $0 \leq S_{\text{UWB}}(\phi) \leq 1$.

The UWB power reflection coefficients from an infinite planar media having the complex permittivities of the liquid material and muscle are shown in Figs. 2.3 (a) and (b). The error and the rms error in the reflection coefficients between muscle and phantom were also evaluated by Eqs. (2.1) and (2.2), where y is either $R_{\text{UWB, TE}}$ or $R_{\text{UWB, TM}}$ and x is the incident angle θ_i ($0° \leq \theta_i \leq 90°$). Around $\theta = 82°$ (Brewster angle), the error in UWB power reflection coefficients for TE incidence exceeded 100%, since $R_{\text{UWB, TE}}(82°)$ for muscle was very small ($< 4.0 \times 10^{-4}$), but the rms error over the incident angle θ was 15%. The maximum and rms errors for TM incidence were 0.7% at $\theta = 2°$ and 0.5% rms.

The UWB scattering coefficients from a dielectric sphere with a diameter of 200 mm and an infinite dielectric cylinder with a diameter of 64 mm are shown in Figs. 2.3 (c), (d) (TE), and (e) (TM). The sphere was supposed to represent a human head and the cylinder a human arm. The error and the rms error in the scattering coefficients from the sphere or the cylinder were again evaluated by Eqs. (2.1) and (2.2), where y is either $S_{\text{UWB, sphere}}$ or $S_{\text{UWB, cylinder}}$ and x is the scattering angle ϕ_i ($0° \leq \phi_i \leq 180°$). The errors in the UWB scattering coefficients from the sphere were 15% maximal at $\phi = 151°$ and 6% rms over the scattering angle ϕ. Similarly, the errors in the UWB power scattering coefficients from the cylinder were 0.2% maximal at $\phi = 17°$ and 0.6% rms for TE incidence; and -4.6% maximal at $\phi = 139°$ and 4% rms for TM incidence. The aqueous solutions, distilled water and physiological saline water were all outperformed by the proposed recipe [40].
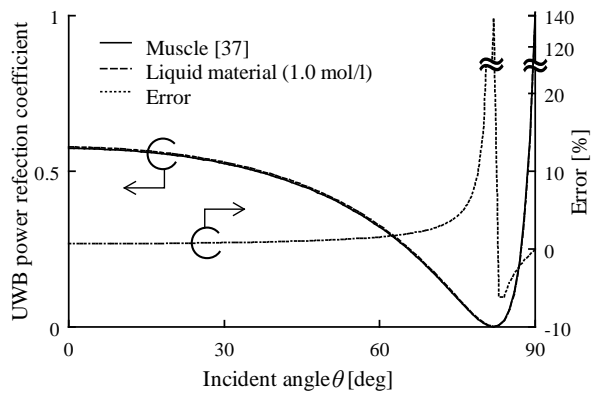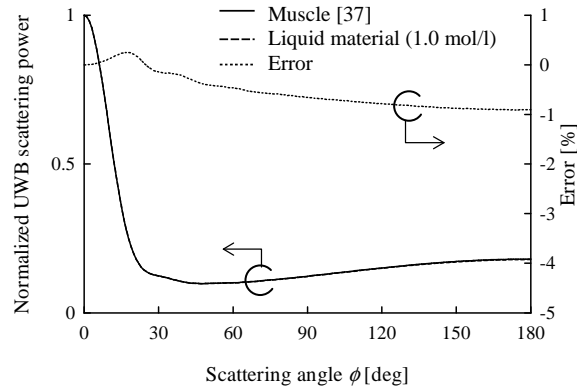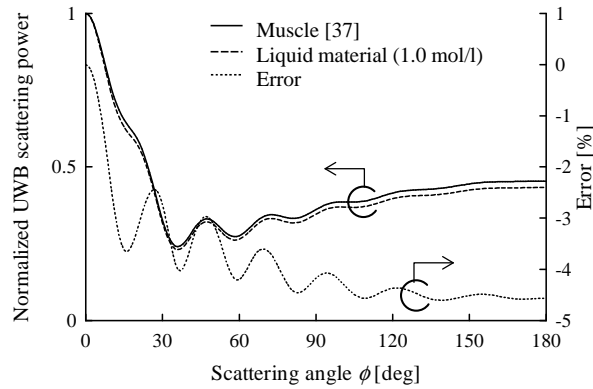
(a)
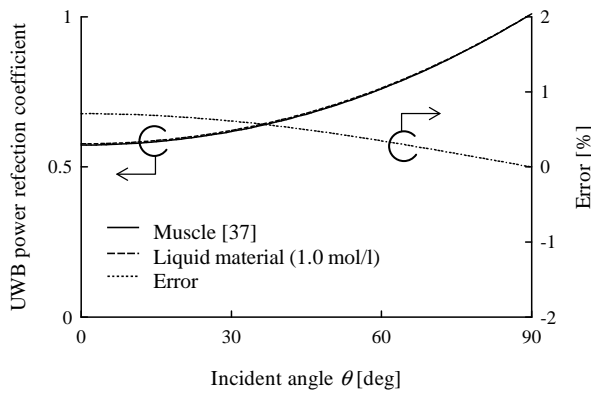
(b)
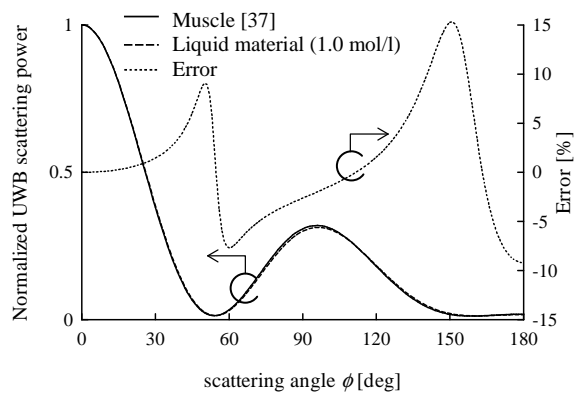
(c)

Fig. 2.3. Evaluation of liquid phantom material (1.0-mol/l aqueous solution of sucrose) in comparison with muscle: reflection coefficient from an infinite plane (a) TE and (b) TM; and scattering coefficient from (c) a sphere, (d) a cylinder (TE), and (e) a cylinder (TM).

(d)

(e)

Fig. 2.3.   Continued.

In addition, the distortion of UWB waveforms reflected from a planar infinite medium [36] and the error performances of an infinite cylinder in $\dot{\varepsilon}$ were numerically analyzed, assuming the incidence of Gaussian modulated impulse occupied 3.1 to 10.6 GHz, as shown in Fig. 2.4. The waveforms were evaluated using different schemes as follows: the incident impulse waveform was Fourier-transformed into the frequency domain; next, the scattered wave was calculated in the frequency domain by using the complex Fresnel reflection coefficient (for the planar medium) or by using a series expansion method [39] (for the cylinder); and then, the scattered wave was inverse Fourier-transformed (IFT) into the time domain. The reflected waveforms from an infinite plane for plane wave (TE and TM) incidence with 45° are shown in Figs. 2.5 (a) and (b). The error and the rms error for the reflected or scattered waveforms were

evaluated by Eqs. (2.1) and (2.2), where y is waveform and x is time t_i (-0.375 $\leq t_i \leq$ 0.375 ns). The errors were 2.0% maximal at -0.35 ns and 0.9% rms over the time of pulse duration for TE incidence, and 3.8% maximal at -0.35 ns and 1.7% rms for TM incidence. The forward scattered waveforms for an infinite cylinder (having a diameter of 64 mm) are shown in Figs. 2.5 (c) and (d). The errors were 145% maximal at -0.30 ns and 12% rms for TE incidence; and -60% maximal at -2.42 ns and 4.2% rms for TM incidence. The correlation coefficients between the reflected waveforms from an infinite plane or an infinite cylinder of our material and muscle were greater than 0.999, and thus the waveform distortions were also negligibly small. From Figs. 2.5 (a) to (d), the solid and broken lines (for muscle and liquid materials, respectively) were almost indistinguishable, expect in the case of Fig. 2.5 (c). The effects of typical errors in $\dot{\varepsilon}$ on the correlation coefficients of waveforms were numerically evaluated. The correlation coefficients were greater than 0.995 when the errors in $\dot{\varepsilon}$ were within 30% (see Appendix A). The distortions of waveforms reflected from distilled water and from physiological saline water were also compared. The effects on the waveform distortion caused by difference in $\dot{\varepsilon}$ were small in comparison with muscle.
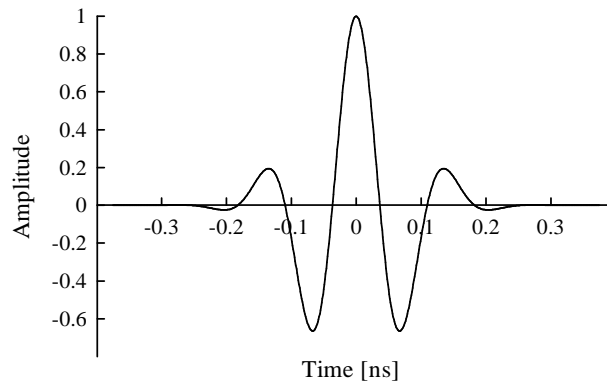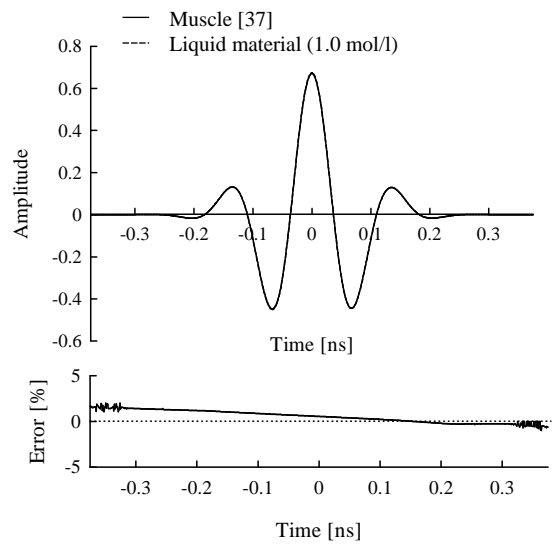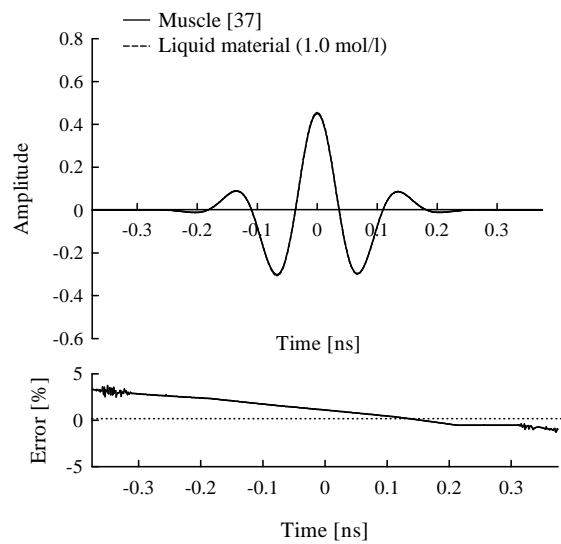
(a)
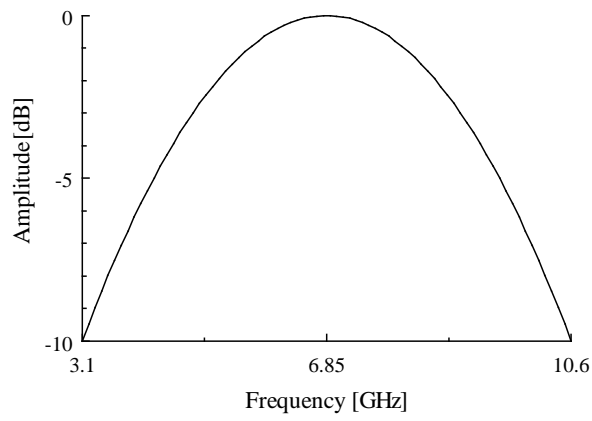
(b)

Fig. 2.4. Gaussian modulated impulse occupying 3.1 to 10.6 GHz: (a) waveform and (b) spectrum.
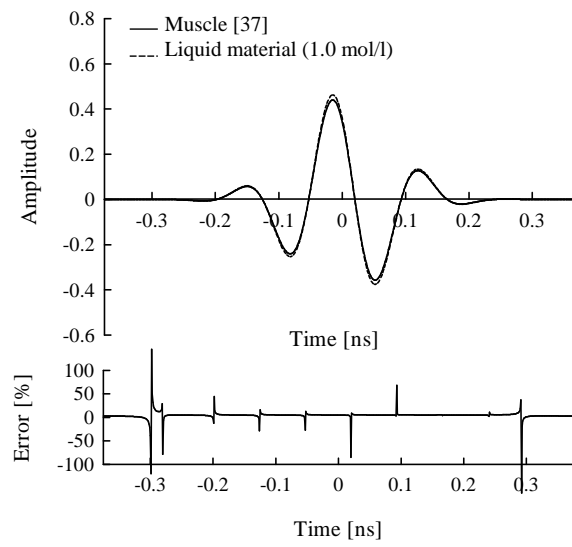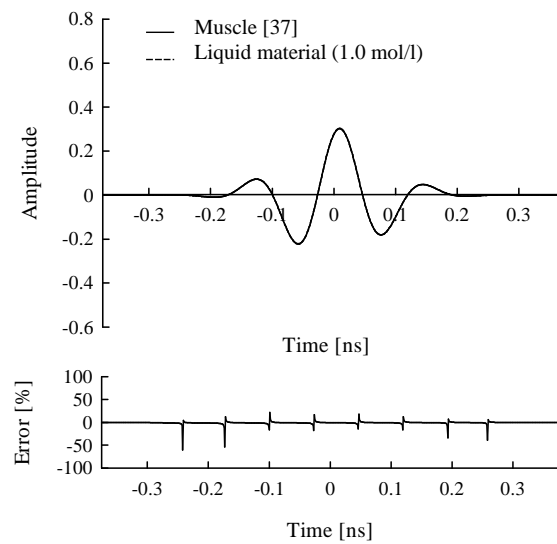
(a)

(b)

Fig. 2.5.   Evaluation of liquid phantom material (1.0-mol/l aqueous solution of sucrose) in comparison with muscle: reflected wave from an infinite plane: (a) TE wave and (b) TM wave; forward scattered waveform from a cylinder: (c) TE wave and (d) TM wave.

(c)

(d)

Fig. 2.5.   Continued.

2.2 Effects of Feeding Cable Configurations on Propagation Measurements between Electrically Small Antennas

In on-body scenarios, transmitting and receiving antennas are placed in proximity to each other (typically less than 500 mm apart) since WBAN devices are placed on body surfaces. The unwanted radiation unavoidably induces unwanted coupling not only between the cables feeding the transmitting and receiving antennas, but also between the antenna and the cable(s). For the above reasons, there are fluctuations in the measured transfer functions. This coupling depends on the geometrical configuration of the cables, but these effects have not been carefully taken into account in the previous experiments. The use of microwave over fiber systems (e.g. [41]) for transmitting antennas mitigates the problem, but makes it impossible to measure the VSWR during operation, and dynamic ranges are also restricted. This section reports the experimental results of the effects of cable configurations on short-range UWB propagation measurements [42] by using the commonly used meanderline antennas [43].

2.2.1 Experimental Set-up

The UWB (from 3.1 to 10.6 GHz) frequency- and time-domain path gains were measured with a vector network analyzer (VNA) between vertically-polarized meanderline antennas (Fig. 2.6 [43]) in a 3-m radio anechoic chamber in the absence of a human body. The VSWR of the meanderline antenna was less than 2.5 from 3.1 to 10.6 GHz and omnidirectionality in the horizontal plane was within 3 dB in free space. The transmitting and receiving antennas were attached to a styrofoam columm (almost transparent to microwaves), and separated horizontally $d_h = 100$ mm and vertically either $d_v = 0$, 100, or 200 mm apart, as shown in Fig. 2.7. In Fig. 2.8, four different set-ups of coaxial cables feeding the transmitting and receiving antennas were verified: vertical and vertical (denoted by VV), horizontal and vertical without crossing (HV), horizontal and vertical with crossing (HVC), or horizontal and horizontal (HH). The feeding cables were flexible and 2 m in length, possessing polyvinyl chloride, silver plated copper braids, low density polytetrafluoroethylene, silver-plated copper, and SMA connectors, as shown in Fig. 2.9. When the cable was placed horizontally with the aid of an L-shape adaptor (Fig. 2.10), the length of the horizontal portion was approximately 500 mm.
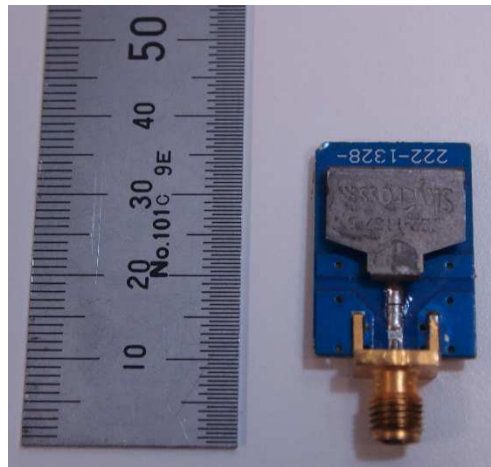
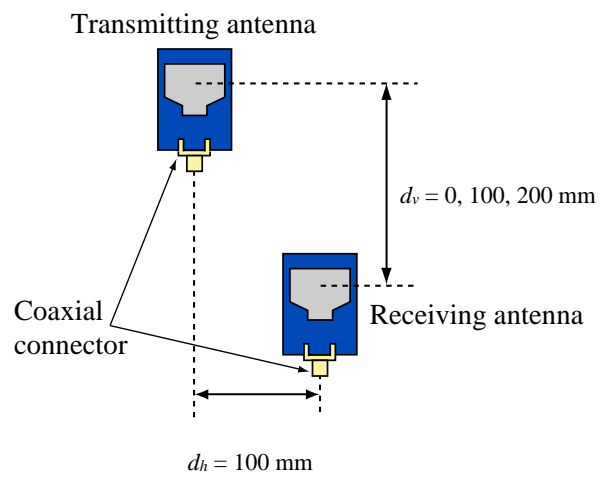Fig. 2.6.   Antenna under test: meanderline antenna [43].
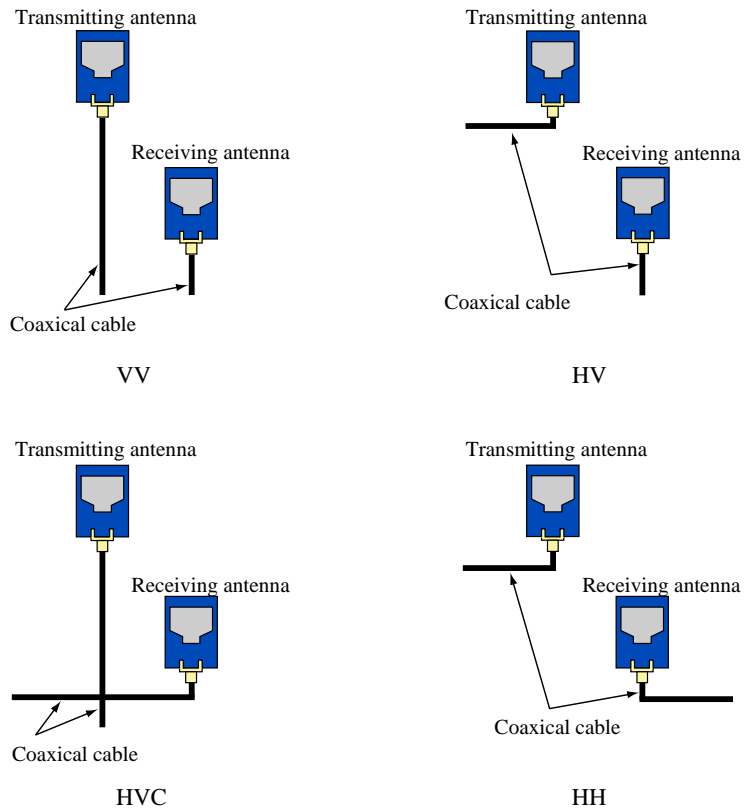

Fig. 2.7.   Experimental set-up.

Fig. 2.8. Cable configurations: vertical and vertical (VV), horizontal and vertical without crossing (HV), vertical and horizontal with crossing (HVC), and horizontal and horizontal (HH).
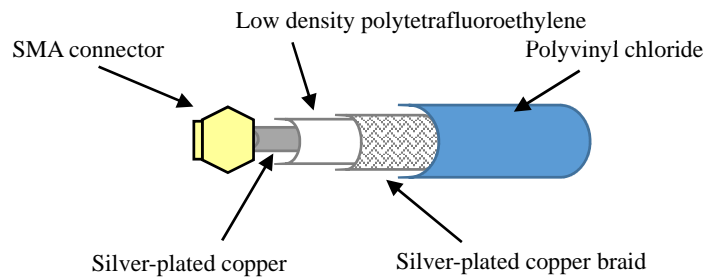

Fig. 2.9. Illustration of the feeding cable.


Fig. 2.10 An L-shape adaptor.

2.2.2 Measurement results

Fluctuations in frequency-domain path gain and delay profiles for the different vertical distances d_v (= 0, 100, and 200 mm) and cable configurations (VV, HV, HVC, and HH) are shown in Figs 2.11 and 2.12. The HV and HVC configurations yielded the least and the greatest oscillating frequency responses, respectively (with VV and HH in between). As shown in Fig. 2.12 (a), (b), and (c), the first waves (marked by *) arrived at the excess delay time of 0.7, 0.8, and 1.0 ns, respectively, depending on the distance between the transmitting and receiving antennas. The HVC configuration resulted in noticeably delayed waves (marked by †) moving toward later times with increasing d_v, which implies that the coupling in the vicinity of the crossing point of the two cables was significant. On the other hand, the HV configuration yielded the least coupling between cables.

Then we calculated the ratios of the power contained in the first waves (the first peak in the delay profiles ±0.25 ns) to the total received power (between 0 and 3 ns) from the measured delay profiles, as shown in Fig. 2.13. The ratios were within -0.5, -0.2, and -0.9 dB for the VV, HV, and HH configurations, respectively, while they decreased significantly (as far as -8 dB) for HVC as d_v increased. This is because while the power of the first waves (marked by * in Fig. 2.12) decreased as d_v increased, the power of the delayed waves (†) remained unchanged.

From these results, it was found that the HV configuration yielded the least coupling. Hence, we opted for an on-body measurement set-up that adopted the HV cable configuration, as shown in Fig. 2.14.

On the other hand, the low-VSWR monopole antennas [44] (Fig. 2.15) having relatively large ground planes showed significantly smaller effects from the cable coupling regardless of the cable configurations, as shown in Figs. 2.16 and 2.17. The variation in frequency-domain path gain was within 3 dB among the four cable configurations. The ratios were also calculated of the power contained in the first waves (for the first peak the delay profiles were ±0.375 ns instead of ±0.25 ns because the antenna size was larger) to the total received power (between 0 and 3 ns) from the delay profiles. The ratios fell within -0.1 dB regardless of the cable configurations. The effects of the coupling between the cables and between the antennas and the cables were, therefore, negligible in the cases of the low-VSWR antennas. Their large ground planes (= 100 mm in diameter), however, are not necessarily suitable for small WBAN devices.
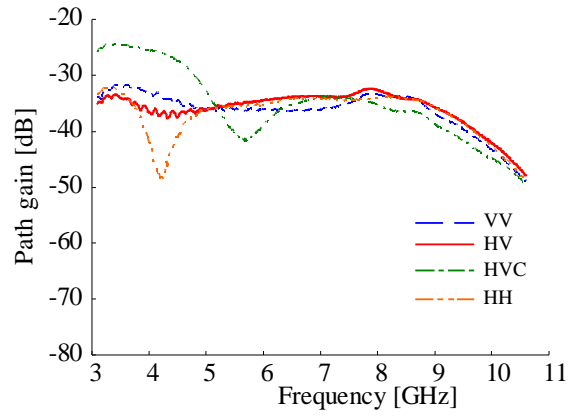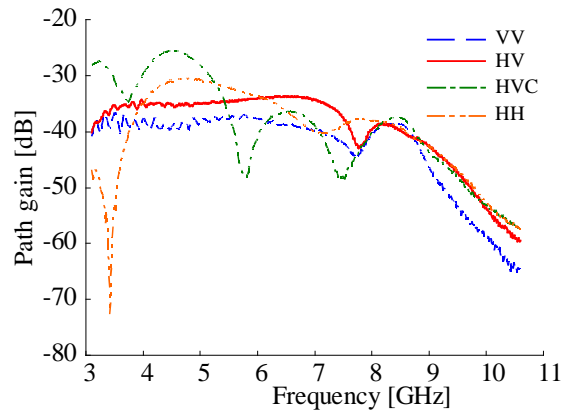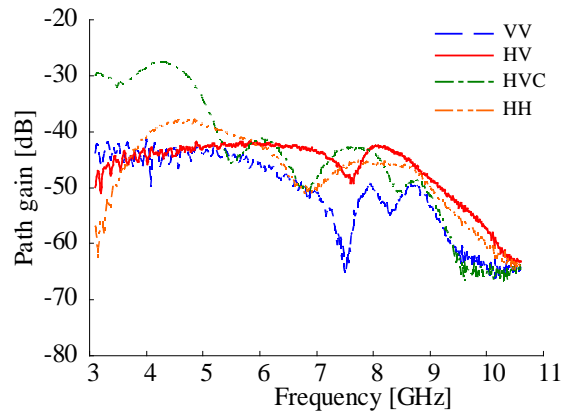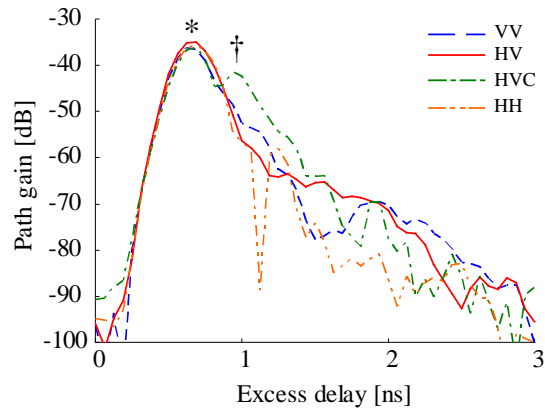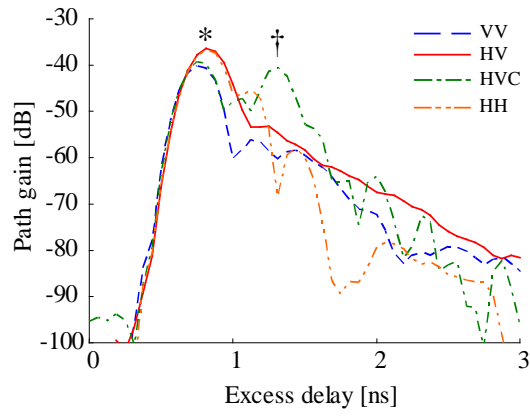
Fig. 2.11.   Frequency-domain path gains between meanderline antennas: (a) $d_v = 0$, (b) 100, and (c) 200 mm.

Fig. 2.12. Time-domain path gains between meanderline antennas: (a) $d_v = 0$, (b) 100, and (c) 200 mm. The first wave was denoted by * and the noticeably delayed wave by †.
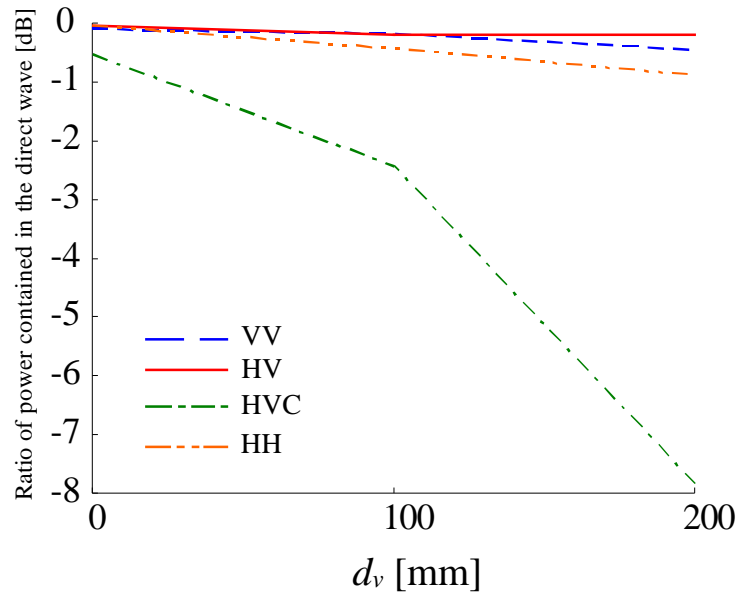
Fig. 2.13.   Ratio of the power contained in the direct wave to the total power.

HV configuration

Rx

Tx

Human

Coaxical cable

VNA
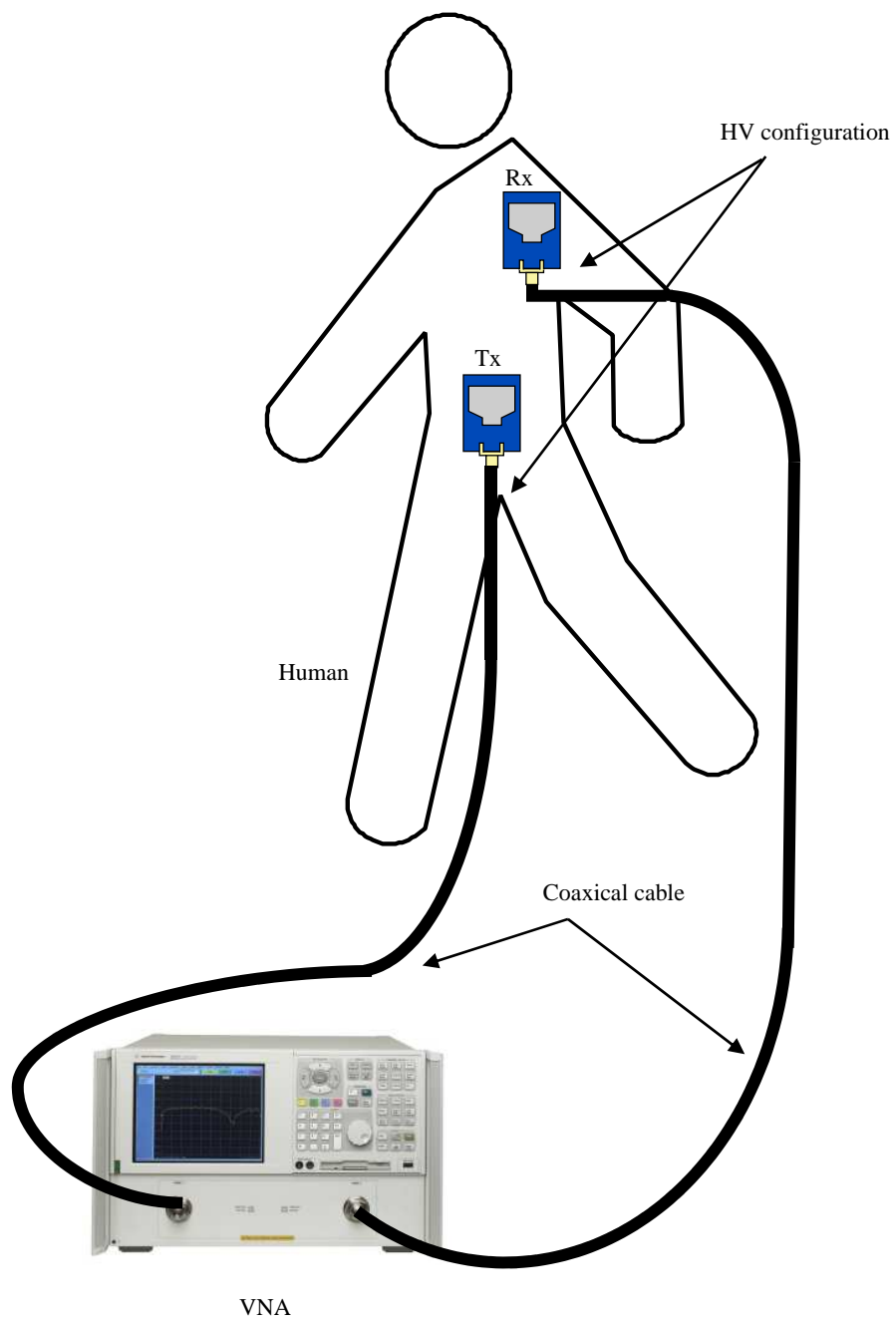
Fig. 2.14.   On-body measurement set-up that adopted the HV cable configuration.
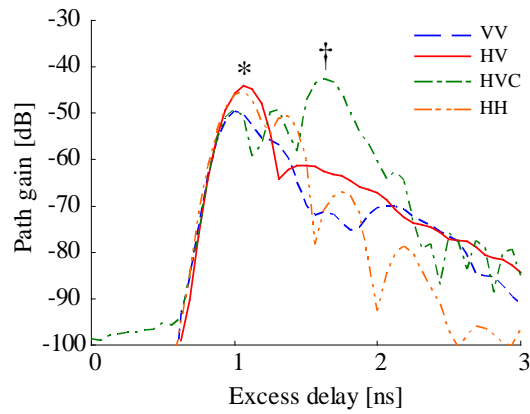
Fig. 2.15.   Antenna under test: low-VSWR monopole antennas [44].

Fig. 2.16. Frequency-domain path gains between monopole antennas: (a) $d_v = 0$, (b) 100, and (c) 200 mm.
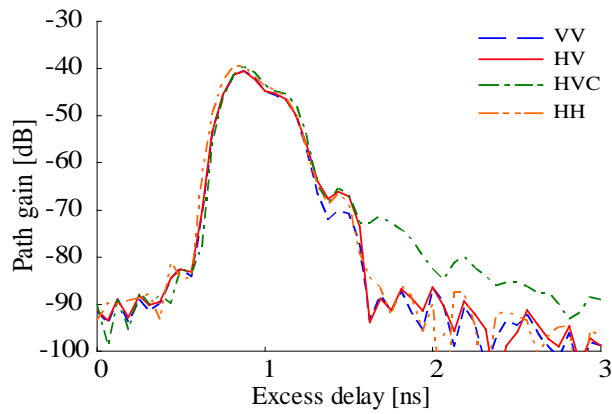
Fig. 2.17.   Time-domain path gains between monopole antennas: (a) $d_v = 0$, (b) 100, and (c) 200 mm.

2.3　Summary

An aqueous solution of sucrose ($C_{12}H_{22}O_{11}$, 1.0 mol/l) provided the best results within a UWB bandwidth of 3.1 to 10.6 GHz. The maximum and rms errors between 2 and 12 GHz were 12% maximal at 2.0 GHz and 8.5% rms for ε'; and 28% maximal at 7.0 GHz an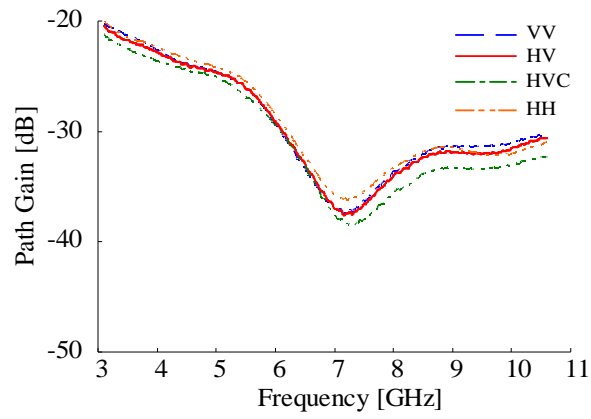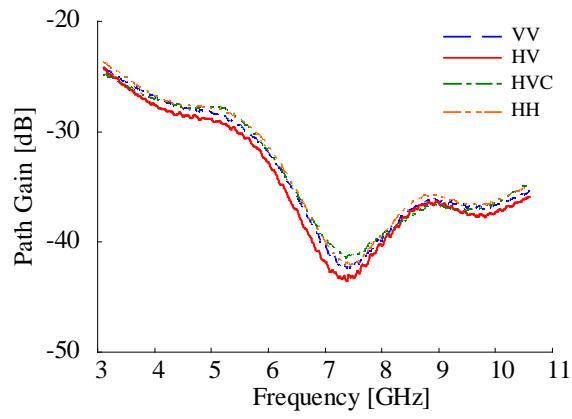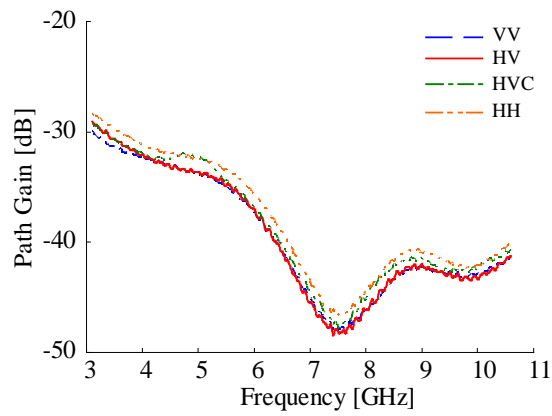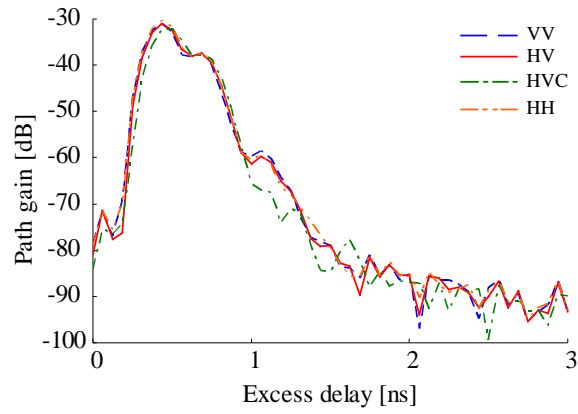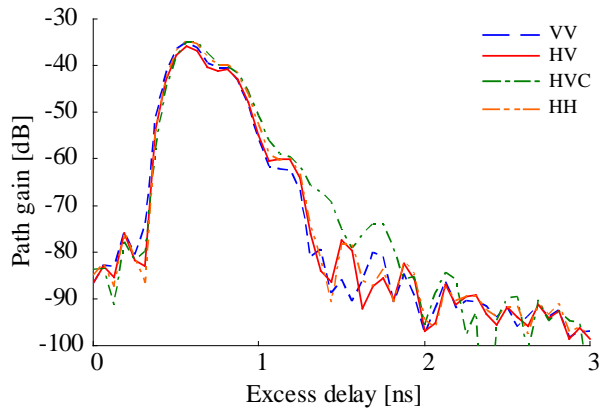d 21.5% rms for ε''. Although the maximum errors were relatively large, the rms errors were found to be tolerably small, considering typical measurement accuracies of around 5%. Reflection and scattering from homogeneous dielectric media in typical shapes (an infinite plane, a sphere, and an infinite cylinder) were calculated to evaluate the effect of these errors on the phantom performances, assuming a plane wave TE or TM incidence. In addition, the distortion of UWB waveforms reflected from a planar infinite medium and an infinite cylinder with errors in $\dot{\varepsilon}$ was numerically analyzed, assuming that the incidence of Gaussian modulated impulse occupied 3.1 to 10.6 GHz. The performance of the liquid UWB phantom material (1.0-mol/l aqueous solution of sucrose) was similar to that of muscle.

The effects of the feeding cable configuration on UWB radio propagation were measured. It was found that careful attention should be paid to the cable configuration when electrically-small large VSWR antennas were used. It was also found that a perpendicular configuration of transmitting and receiving antennas without crossing (HV) yielded the least significant effects.

Chapter 3

Measurements of UWB Propagation Channels between a Base Station and On-/Off-Body Antennas

3.1   Objectives

While on-body UWB radio propagation performances have been studied experimentally [16], [19], [45], [46] and numerically [17] (using ray-tracing and finite-difference time-domain techniques), off-body UWB radio propagation characteristics have not been evaluated. Two UWB propagation channels envisioned for WPAN [40] are discussed in this chapter. First, a desktop environment in which a human arm blocks an LOS path, for instance, a wireless mouse and keyboard, was employed. Next, the radio propagation characteristics between a base station and an antenna mounted on a human torso were investigated.

3.2   Propagation Channels Around an Arm

An arm phantom was developed using a cylindrical container and the liquid material described in the previous section 2.1. The container, made of an acrylic resin, was 3 mm in thickness, 500 mm in length, and 64 mm in diameter, and was filled with the 1.0 mol/l sucrose solution. The relative permittivity of the acrylic resin was 2.5 (at 10.6 GHz) to 2.8 (at 3.1 GHz). A plastic intake was attached to the bottom of the cylinder to fill the liquid.

The phantom was evaluated in a typical propagation environment in comparison with the real human arms of three adult volunteers (age: 22 to 24, length between the elbow to the tip of the fist: 340 to 380 mm, width of fist: 90 to 110 mm). The three volunteers were employed to investigate the differences between individuals and we could not gather any more volunteers. The UWB additional path loss caused by a real human arm blocking the LOS path was found to be up to 10 to 12 dB [6]. In the same propagation environment, the relative UWB path gains and delay

profiles were measured by a VNA on a metal plate simulating a typical office desk (1200×800 mm), as shown in Fig. 3.1. Desktops are the most common environment in which WPAN is employed. Transmitting and receiving antennas were omni-directional low VSWR monopole antennas [44], which were separated by 500 mm in the center of the metal plate for transmission and reception. The real and phantom arms were perpendicular to the LOS at the center of the propagation path. The location x of the fingertip of volunteers or the bottom (without the intake) of the arm phantom was moved from -200 to +200 mm at 20 mm intervals, where the intersection of the LOS and the loci of the arm was the origin, as shown in Fig. 3.2. The frequency range was 3.1 to 10.6 GHz. All the measurements were carried out in a 3-m radio anechoic chamber. The diameter of the free-space first Fresnel zone, which was partially blocked by a human or phantom arm, ranged from 192 mm (at 3.1 GHz) to 104 mm (at 10.6 GHz).

The measurement results for the relative path gain are shown in Fig. 3.3 (a). The relative path gain caused by the human arms and the arm phantom were found to be up to 9 to 11 dB and 9 dB, respectively. The errors in the relative path gain between the human arms and the arm phantom were within 1.0 to 1.2 dB rms. The delay profiles when $x = 200$ mm were also essentially similar, as shown in Fig. 3.3 (b). These results validated the proper electromagnetic response of the arm phantom, and this arm phantom was thus deemed to be usable for experimental evaluation of UWB antennas and propagation.
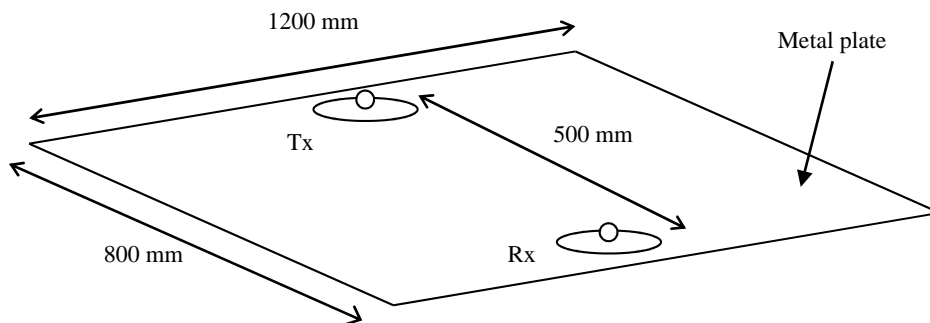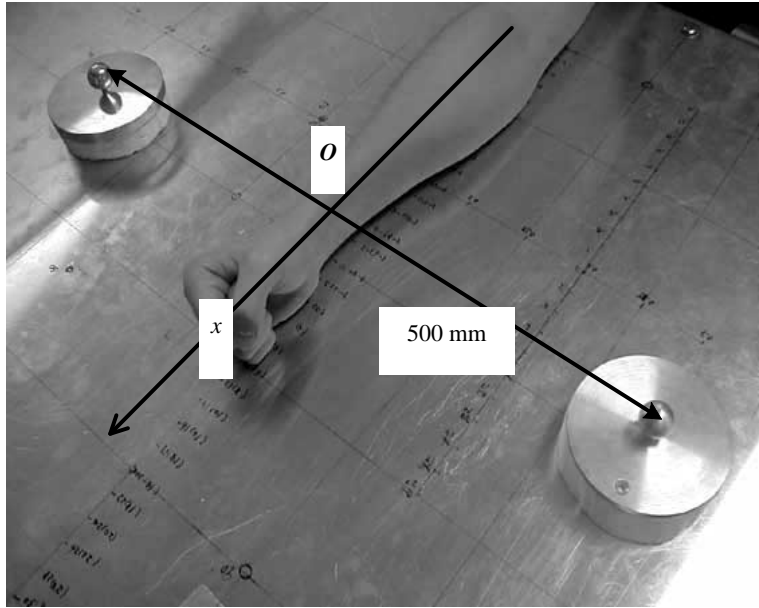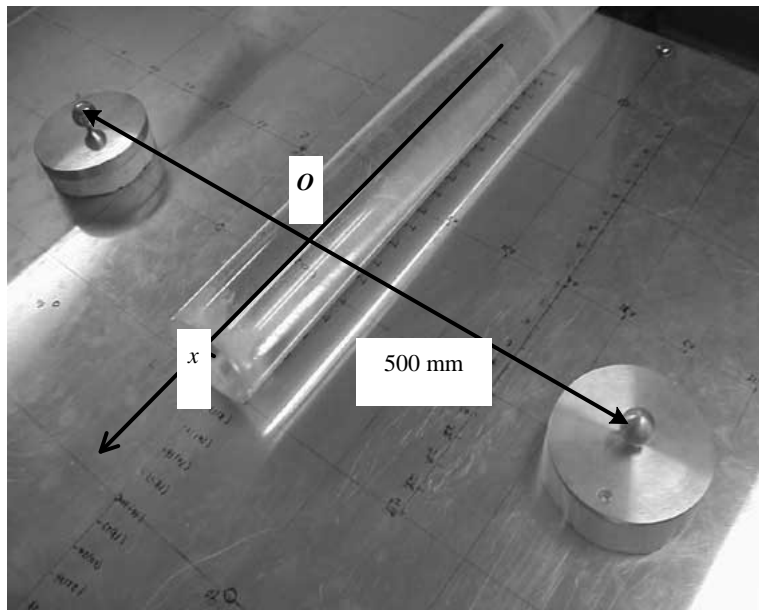

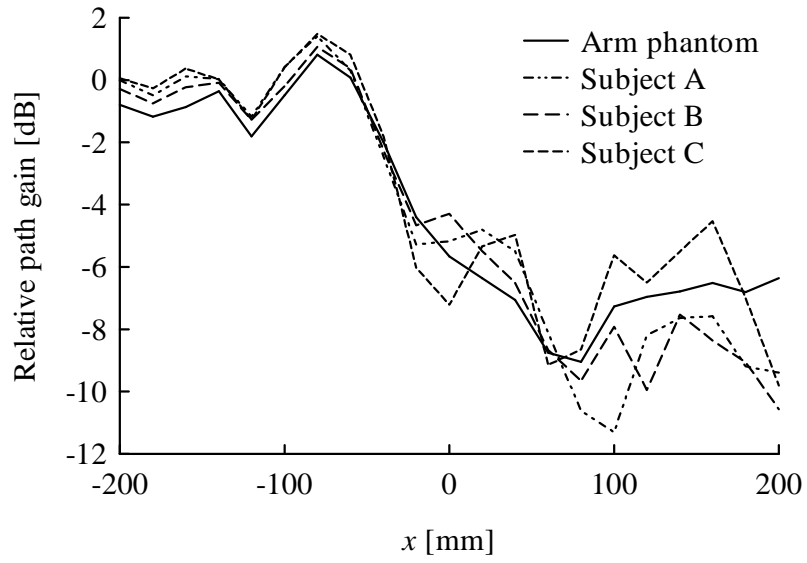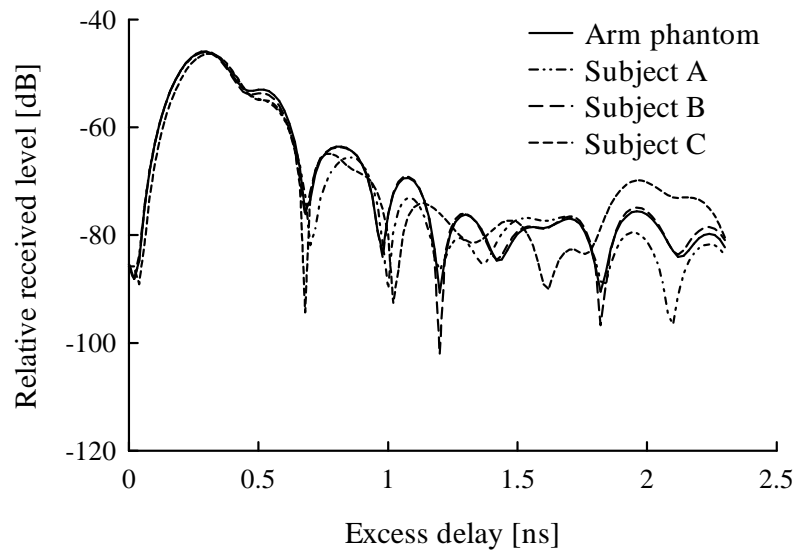Fig. 3.1.   Simplified office desk.

(a)

(b)

Fig. 3.2.   Measurements of additional loss caused by (a) a human arm and (b) an arm phantom on a conductive

plane.

(a)

(b)

Fig. 3.3.   Comparison of the arm phantom and the human arms: (a) relative path gain and (b) delay profiles measured when $x = 200$ mm.

3.3   Propagation Channels Around a Torso

A torso phantom was developed using a nearly-parallelepiped 20-liter (approximately $340 \times 200 \times 350$ mm in outer size) polyethylene water tank and the 1.0 mol/l sucrose solution. The relative permittivity of the polyethylene was 1.5 (at 10.6 GHz) to 1.9 (at 3.1 GHz). This phantom was compared with three adult male volunteers in a situation where WBANs are typically employed. In WBAN scenarios, sensor nodes collect various data and send them to a coordinator. The coordinator is mostly placed around the torso, and the transmitting antenna (an omnidirectional monopole) [44] mounted on the back waist of the volunteer or the broad side of the torso phantom. The electric center of the antenna was separated by 50 mm from the body surface (since the ground plane of the monopole antenna was 100 mm in diameter). The receiving antenna (a double-ridged waveguide horn, 2 to 18 GHz) was placed at a distance of 3 m in a radio anechoic chamber, as shown in Figs. 3.4 and 3.5. The volunteers were 22 to 24 years old, their height 1.70 to 1.79 m, and the breadth of chest 310 to 340 mm. The height of the two antennas was 1.17 m. The propagation losses and delay profiles between the two antennas were measured, while rotating the human body or the torso phantom azimuthally from 0º to 180º, as shown in Fig. 3.5 (b). UWB (3.1 to 10.6 GHz) path gain and delay profiles were also measured by using the VNA. The transmitting antenna mounted on the human body or the torso phantom was fed via an optical fiber system [41] instead of a coaxial cable to avoid reradiation from the metallic cable. This optical fiber system employed a wideband (0.1 to 11 GHz) electrical-to-optical transformer, a single-mode optical fiber cable (which is practically transparent to microwaves), and a compact battery-powered optical-to-electrical transformer.

The measurement results are shown in Fig. 3.6. The maximum plunges in the relative path gain were 25 to 28 dB for the volunteers and 23 dB for the torso phantom. The rms errors between the human volunteers and the torso phantom were from 1.0 to 1.4 dB. The delay profiles at the azimuth angle of $0°$ were essentially the same, as shown in Fig. 3.6 (b). Hence, the validity of the torso phantom was confirmed.

When an antenna is placed in close vicinity to a human body, the antenna input impedance changes from that in free space. The UWB (3.1 to 10.6 GHz) input impedance of the omnidirectional monopole antenna [44] was measured in the 3-m radio anechoic chamber. The antenna was separated by either $d = 50$, 100, 200, 500, or 1000 mm from either a human body (an adult male) at waist height or the torso phantom. Figure 3.7 shows the measured input impedance plotted on magnified Smith charts. In the case of $d = 50$ mm, the curves of the
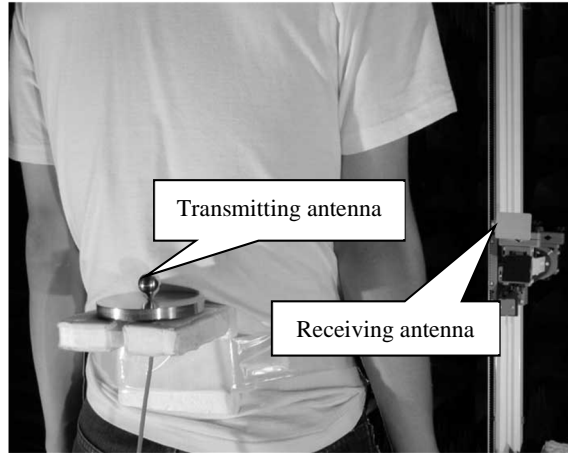
(a)
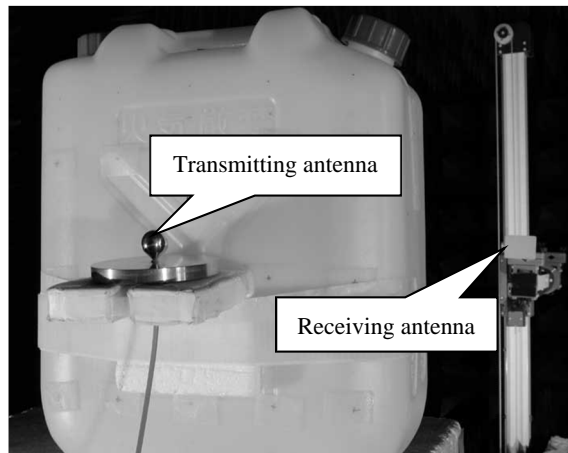
(b)

Fig. 3.4.   Measurement of additional loss caused by (a) a human body and (b) a torso phantom.
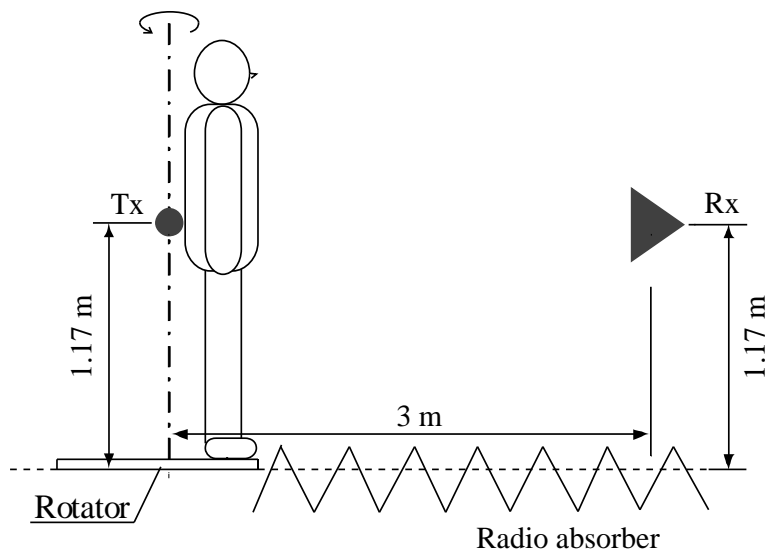
(a)
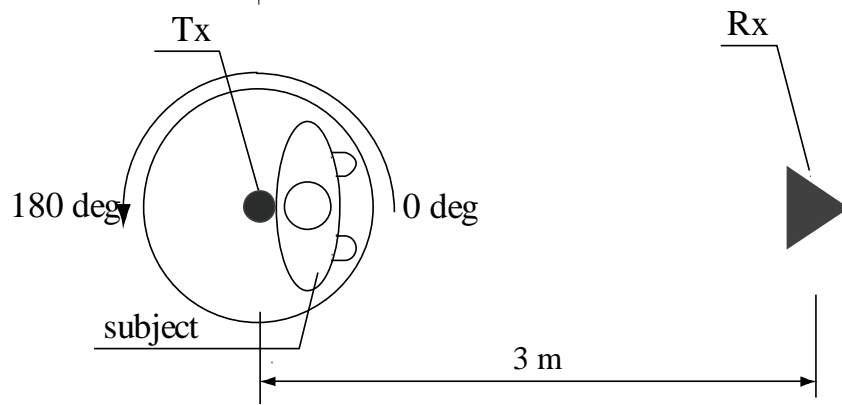
(b)

Fig. 3.5. Experimental set-up for measuring relative path gain and delay profile of human body and torso phantom: (a) elevation and (b) plan views.
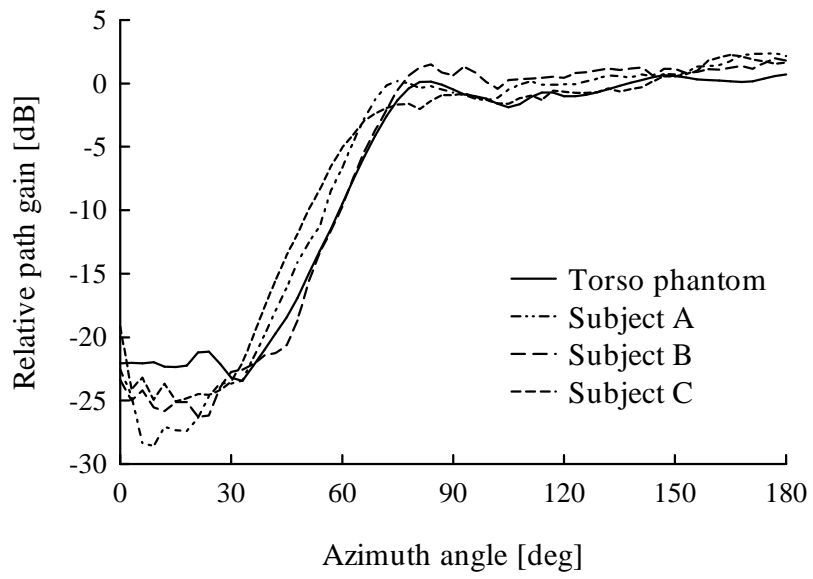
(a)
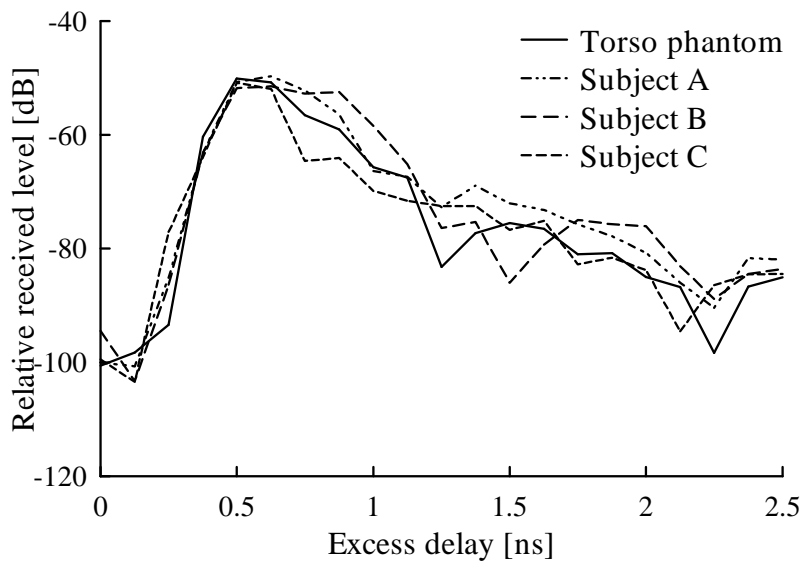
(b)

Fig. 3.6.　Comparison of the torso phantom and the human bodies: (a) relative path gain and (b) delay profiles measured when the azimuth angle = 0°.
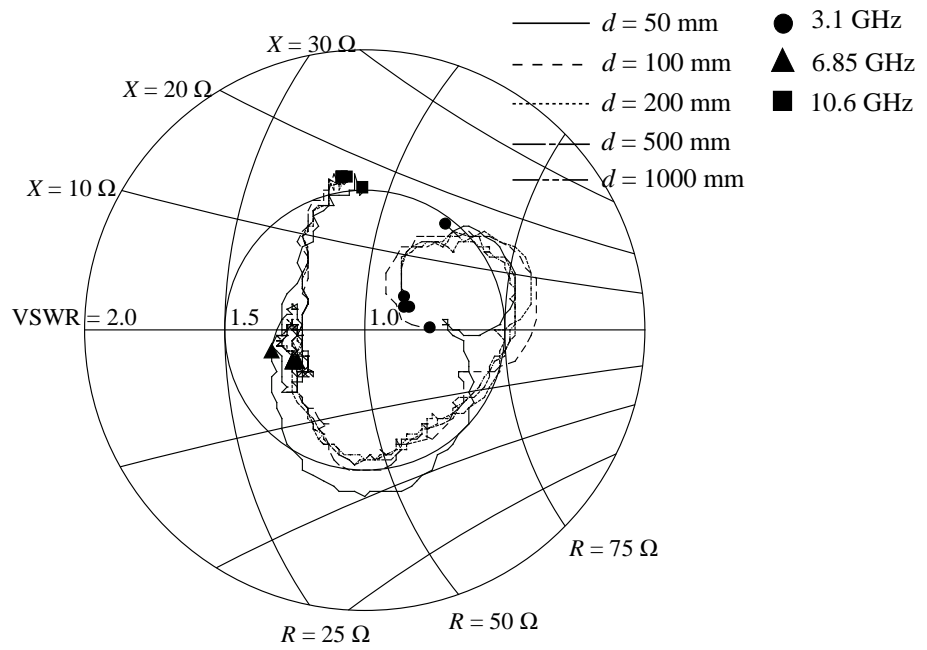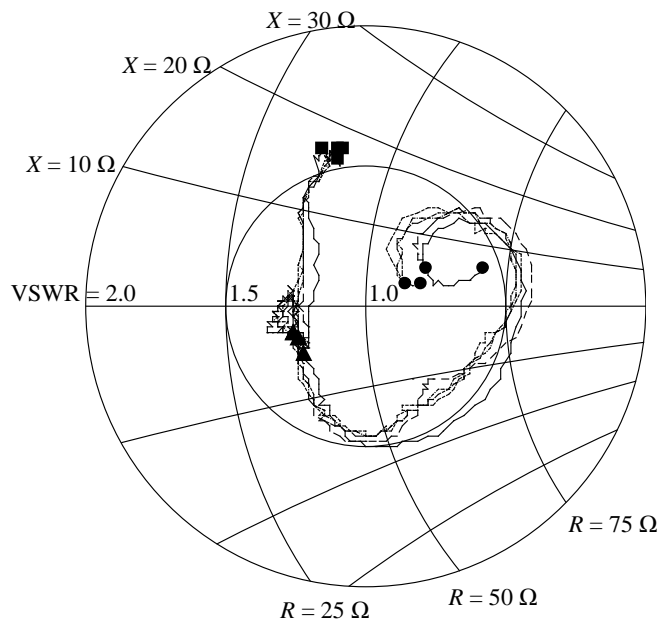
Fig. 3.7.   Measured input impedance of monopole antenna in the vicinity of: (a) a human body and (b) a torso phantom plotted on magnified Smith charts.

human body and the torso phantom deviated slightly from the others, but these two curves were closely similar to each other. Beyond $d = 100$ mm, the curves were almost coincident and thus the effect of the human body (and the torso phantom) was negligible. The torso phantom, therefore, was considered to satisfactorily simulate a human body when the antenna-body distance is either far or near.

3.4   Summary

Radio propagations around the human arm and between a base station and the human torso were measured. In addition to these measurements, the developed UWB arm and torso phantoms were also employed. The maximum plunges in relative path gains when the human and the arm phantom blocked the LOS path were as follows:

- In the case of the volunteers, the relative path gains were found to be up to 9 to 11 dB.
- In the case of the developed arm phantom, the path gains went up to 9 dB.

The maximum plunges in relative path gains when the human torso and the torso phantom blocked the path were as follows:

- In the case of the volunteers, the relative path gains were 25 to 28 dB.
- In the case of the developed torso phantom, the path gain was 23 dB.

Next, the effects of shape imperfection will be discussed. Although the arm and torso phantoms were fabricated as simple shapes (a cylinder and a near parallelepiped), the evaluation results indicate that these phantoms can satisfactorily simulate the respective parts of the human body. The curves of the relative path gains, depicted in Figs. 3.3 (a) and 3.6 (a), were similar to those for knife-edge diffraction. In Fig. 3.3 (a), the relative path gains were around -6 dB when $x = 0$ mm, which corresponded to a diffraction loss of 6 dB when a knife edge touched the LOS. Also, Fig. 3.6 (a) shows that the path gains were around -6 dB when the azimuth angle was approximately 70°, at which point the LOS between the transmitting and receiving antennas touched a vertical edge of the torso phantom. This implies that the dominant forward scattering mechanism in these experimental set-ups was diffraction since the direct wave was blocked by the human body. The scattering characteristics, therefore, were also relatively tolerant of the phantom shapes.

Chapter 4

Measurements and Modeling of UWB Propagation Losses Around the Human Body Dependent on Room Volume

4.1   Objectives

A number of measurements relating to WBAN have also been carried out to characterize on-body UWB propagation in either a radio anechoic chamber or a specific room type [16]-[27]. Conventional UWB propagation loss models in these studies did not consider the impact of the surrounding environments. It is necessary to evaluate the variation in propagation characteristics in various rooms since the major users of WBAN applications move through different-sized rooms. Multipath components (mainly reflected from the floor, walls, and ceiling) are highly dependent on the volume and the construction of rooms.

In this chapter, we examine the measurements and modeling of UWB propagation losses for WBAN, emphasizing the impact of the surrounding environments [47]. The parameters in the conventional UWB propagation loss model were derived from measured results. It was found that the models depend on the room volume and the propagation channel, such as LOS or NLOS. A new model taking account of the impact of room volume was proposed and its parameters were estimated. The probabilistic distributions of propagation losses were also examined, and lognormal distribution was found to yield the best fit.

4.2   Measurement Set-up

The measurement campaigns were conducted in the parallelepiped rooms, as listed in Table 4.1 and illustrated in Fig. 4.1. The dimensions of Room A (a radio anechoic chamber) were measured between the apexes of the radio absorbers paneled on all surfaces. As a radio propagation environment, the radio anechoic chamber can be considered a room extending to an

Table 4.1   Outline of five rooms used for experiments.

	Width [m]	Depth [m]	Height [m]	Volume [m^3]
Room A (radio anechoic chamber)	6.1	3.6	1.9	42 ($\approx \infty$)
Room B	21.6	8.8	2.4	456
Room C	6.6	4.3	2.5	71
Room D	2.7	2.6	2.3	16
Room E	2.0	1.0	2.5	5

infinite volume. Rooms B to E were made of reinforced concrete, and their floors, walls, and ceilings were mostly covered with linoleum, wallpaper, and plasterboard, all of which had lossy dielectrics. Although the five rooms had different volumes, the heights were almost the same, since the heights of rooms from floor to floor do not deviate much within most buildings. The measurements were conducted using three volunteers (adult males, ranging from 1.72 to 1.77 m tall and from 56 to 60 kg). As mentioned in Chapter 3, three volunteers were hired in order to research individual differences and we were unable to gather any more volunteers. Each subject stood upright with the feet shoulder-width apart in either a quiet zone (where reflected waves are minimized and amplitude of the electric field fluctuates less) of the radio anechoic chamber or in the center of Rooms B to E. The standing posture was selected to evaluate the impact of room volume, since it is one of the most typical postures. The UWB (from 3.1 to 10.6 GHz) frequency-domain propagation losses were measured by the VNA. The specifications of the measurements are shown in Table 4.2. Commercially-available meanderline antennas [43] were used for transmission and reception. The VSWR of the antennas was less than 2.5 between 3.1 and 10.6 GHz and the omnidirectionality in the horizontal plane was within 3 dB in a free space. The transmitting antenna was affixed to the center back waist of the volunteers at a height of 1.0 m from the floor, as shown in Fig. 4.2 (also indicated by " * " in Fig. 4.3). The receiving antenna was placed at 100-mm intervals on the torso. Both antennas were vertically-polarized and separated by 10-mm from the volunteers' bodies. When the receiving antenna was placed on the back of volunteers' bodies, the path was roughly LOS; and when on the front, it was NLOS. In total 69 receiving points around the torso were employed. The transmitting and receiving antennas were fed by 2- and 3-m long coaxial cables and these cables were perpendicular in configuration without crossing to reduce undesired cable coupling [42], as described in section 2.2.
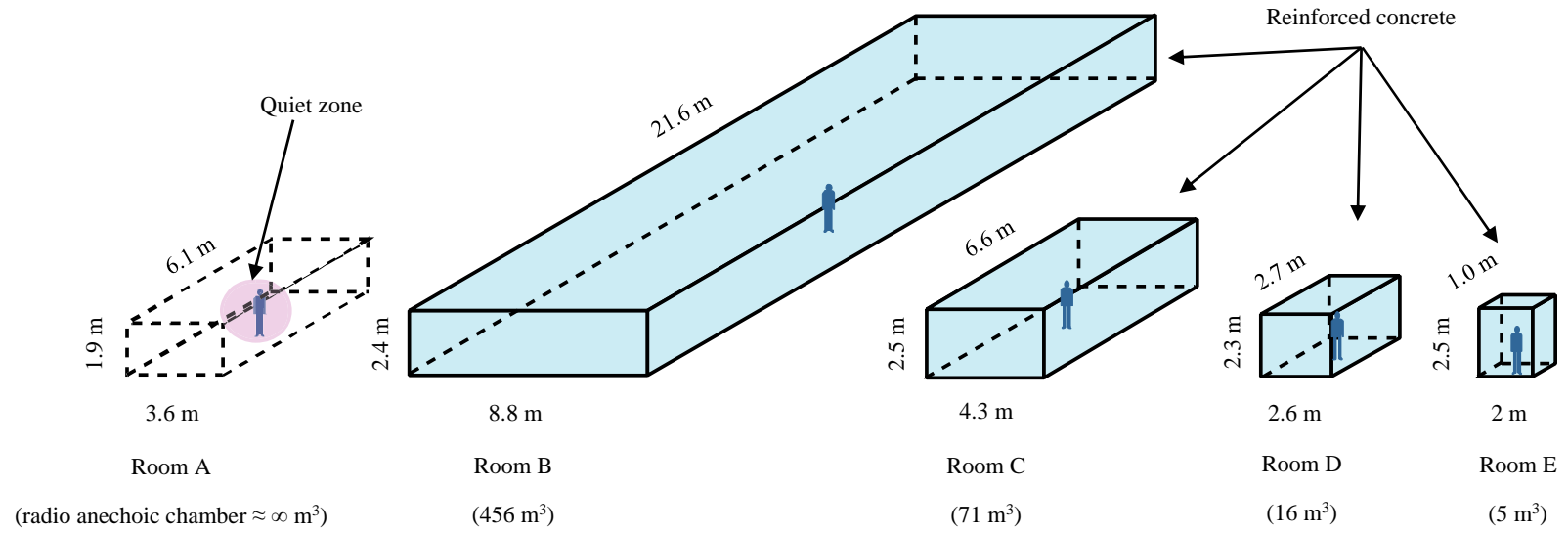
Fig. 4.1.   Illustration of five rooms used for experiments.

Table 4.2　Specifications of the experiment.

Bandwidth	3.1 – 10.6 GHz
Frequency sweeping points by VNA	751 points, 10-MHz interval
IF bandwidth of VNA	100 Hz
Calibration	Internal function of the VNA
Antennas	Meanderline antennas [43]
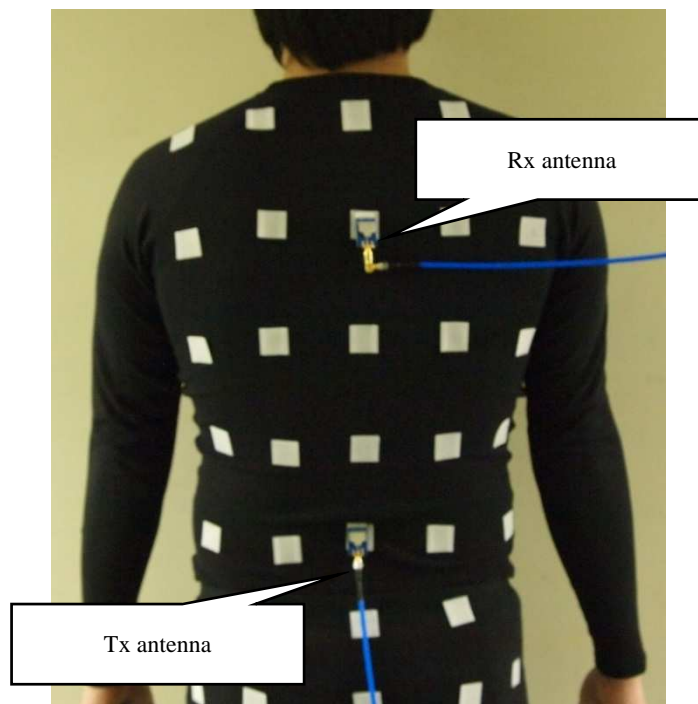
Fig. 4.2.　Placement of transmitting and receiving antennas on the body. The rectangular patches on the clothes are the fabric hook-and-loop fasteners used to fix the antennas in place.

4.3   UWB Propagation Losses

The UWB propagation losses were calculated by integrating the power of the losses between the feeding points of the antennas over the occupied bandwidth:

$$PL_{dB} = 10 \log_{10} \left(\frac{1}{f_H - f_L} \int_{f_L}^{f_H} 10^{\frac{PL_{dB}(f)}{10}} df \right) \quad (4.1)$$

where $PL_{dB}(f)$ is the propagation loss in dB measured at a frequency f, and f_L and f_H are the lowest and the highest frequencies [6]. The calibration was conducted between the feeding points with a coaxial through adaptor. These propagation losses included the antenna gains (typically -10 to 3 dBi), which were affected by the human body and varied depending on the radiation direction and the frequency [48]. A set of examples of the spatial distributions of UWB propagation losses, measured with a volunteer (1.77 m tall and 57 kg) in the five different environments, are shown in Fig. 4.3. The frequency-domain transfer function was obtained by taking the IFT of a delay profile. The number of IFT points was 1,024, consisting of 751 measurements within the 7.5 GHz bandwidth and 273 zeros for zero padding. A rectangular window was used for data windowing. The time resolution was 0.098 ns. Figure 4.4 shows examples of the frequency- and time-domain propagation losses when the receiving antenna was placed on the center chest and the back side of one volunteer (the receiving antenna was placed at a height of 1.3 m from the floor). In Fig. 4.4, the ordinates are absolute values of UWB propagation losses in decibels. The propagation losses decreased with the decreasing room volume, as shown in Figs. 4.3 and 4.4. This was attributed to the large number of multipath components from the nearby floor, walls, and ceiling in Rooms B to E, as shown in Fig. 4.4 (b). The dominant propagation path in Room A (the radio anechoic chamber) was either a direct or a diffracted wave, and thus the total reception power was lower than in the other rooms. With decreasing room volume, mean free path lengths decreased, the power component contained in the multipath components increased, and consequently the total received power increased. Similar phenomena occurred at the other measured points (See Appendix B).

Generally, the wider bandwidth provided higher reception power, because of cancellation of the nulls in the frequency responses [7], [48]. Reception power versus occupied bandwidth at the deepest dead spot was derived from the measured data in the five environments.

UWB reduces fading depth and is therefore advantageous over narrowband from the viewpoint of the link budget (See Appendix C).
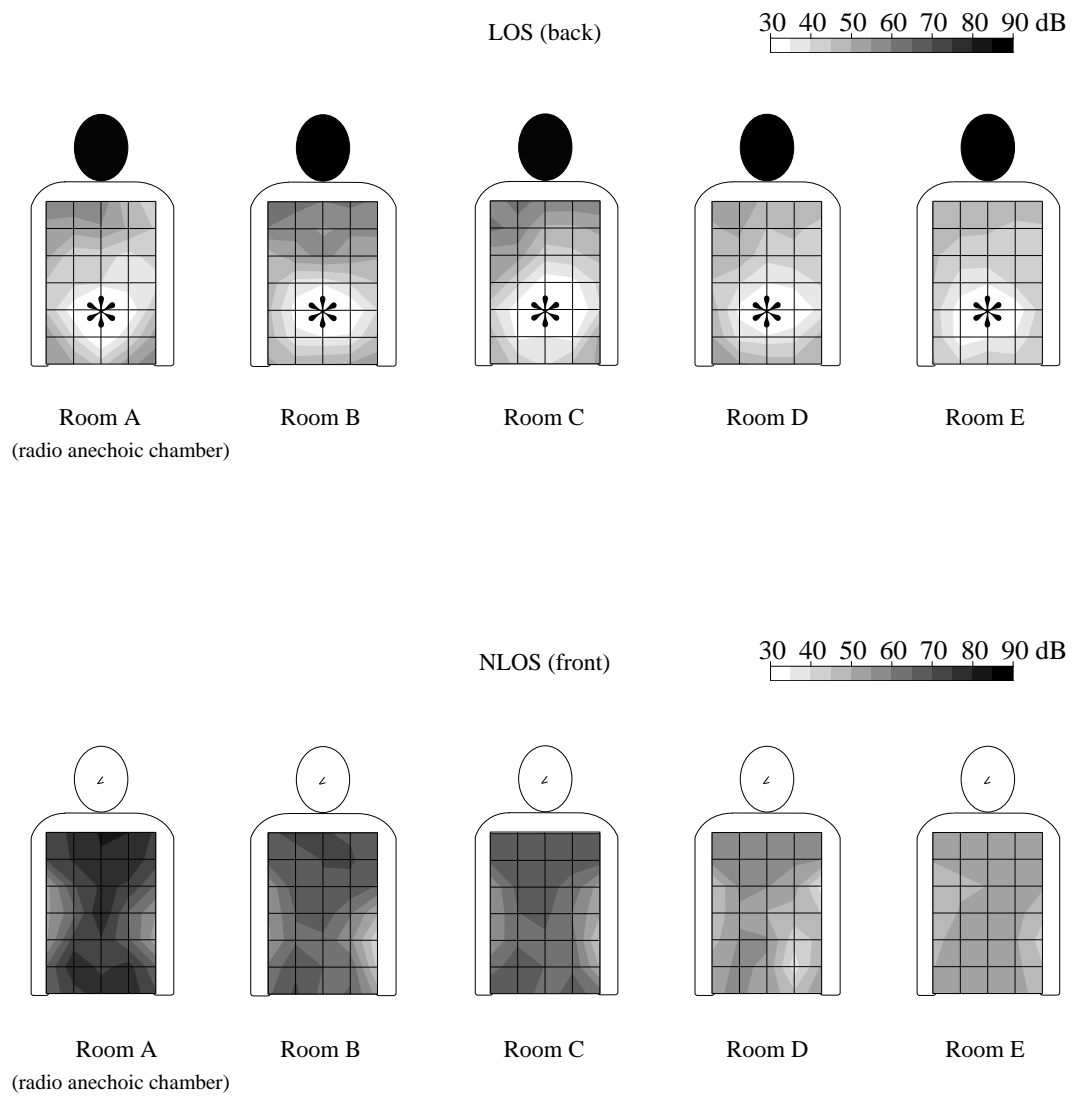
Fig. 4.3. Spatial distributions of UWB propagation losses in the five environments. The transmitting antenna was placed at a point denoted by *.
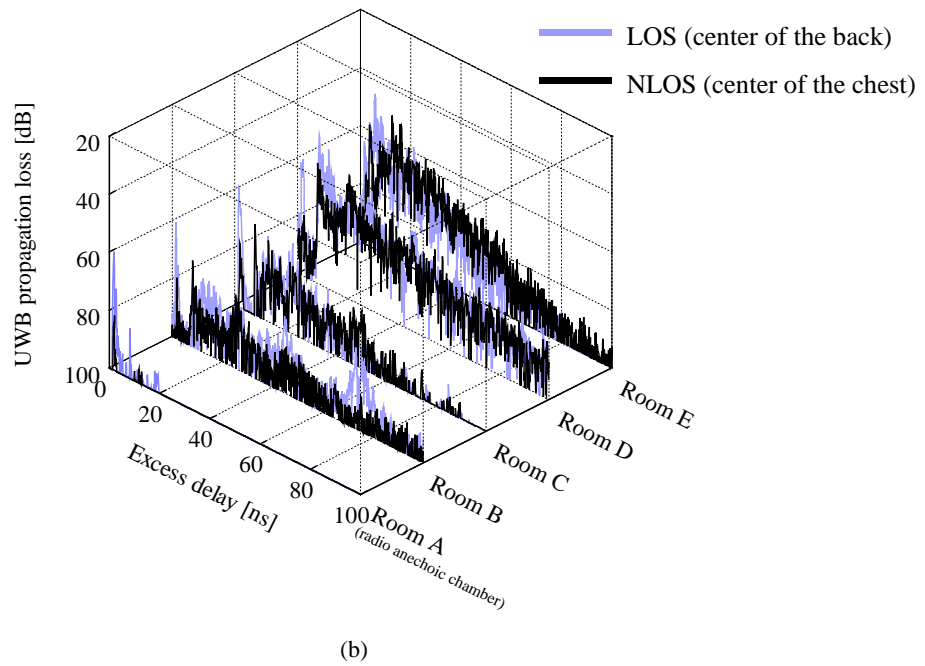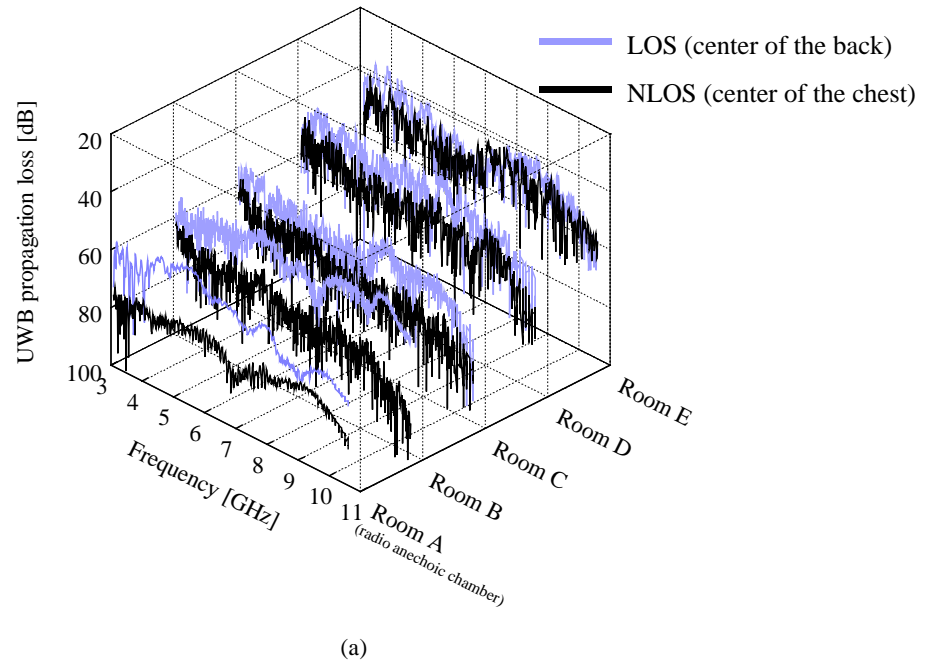
(a)

(b)

Fig. 4.4. Propagation losses at the center of the back (LOS) and the center of the chest (NLOS) in the (a) frequency and (b) time domains. Envelopes of the LOS and the NLOS curves were at approximately similar levels.
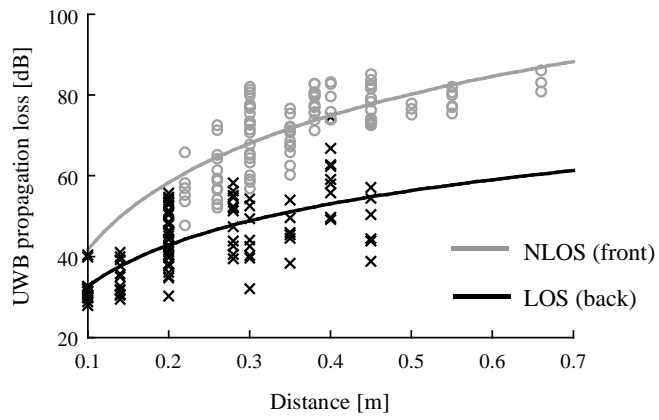
4.4   Propagation Loss Models

Following Fort et al. [21], the propagation losses of on-body channels were approximated by

$$PL_{dB} = PL_{0dB} + 10n \log_{10}\left(\frac{d}{d_0}\right),$$ (4.2)

where PL_{0dB} is the propagation loss at the reference distance d_0 (= 0.1 m), d is the propagation distance (distance along the perimeter of the body between the transmitting and the receiving antennas), and n is the propagation loss exponent. This equation is widely used throughout radio propagation studies. The theoretical n value is 2 in a free space and experimental n is between 3 and 5 in cellular mobile communication environments [49]. Applying the least square method, PL_{0dB} and n were calculated from the measured data. Scattered plots of the UWB propagation loss measured for the three volunteers versus the distance and the obtained loss models are shown in Fig. 4.5. The maximum variation of the propagation losses measured in the radio anechoic chamber was 25 dB (when d = 0.2 m at LOS), while that in Room E (the smallest in size of the five rooms) was 9 dB (when d = 0.1, 0.14, and 0.2 m at LOS) where the dominant propagation components were multipath reflected from the surrounding floor, ceiling, and walls. These 25- and 9-dB variations were found to be nearly insensitive to the three subjects since each subject had almost the same variations. The larger number of multipath components resulted in a smaller spatial variation for ultra wide bandwidth, as shown in Fig. 4.3. PL_{0dB} and n were derived from the data measured for the three subjects. These parameters are summarized along with the associated 95% fidelity intervals in Table 4.3, and the behaviors of the parameters were as follows:

- In the case of LOS, because the dominant propagation path was a direct wave, the differences in PL_{0dB} between the five environments were negligible.
- In the case of NLOS, PL_{0dB} also differed negligibly.
- In the case of LOS, n decreased (from 3.4 to 2.2) with decreasing room volume, since in a smaller room the total receiving power contained more contributions from the large number of multipath components, which were independent of d.
- In the case of NLOS, n also decreased (from 5.5 to 0.6) with decreasing room volume.

(a)
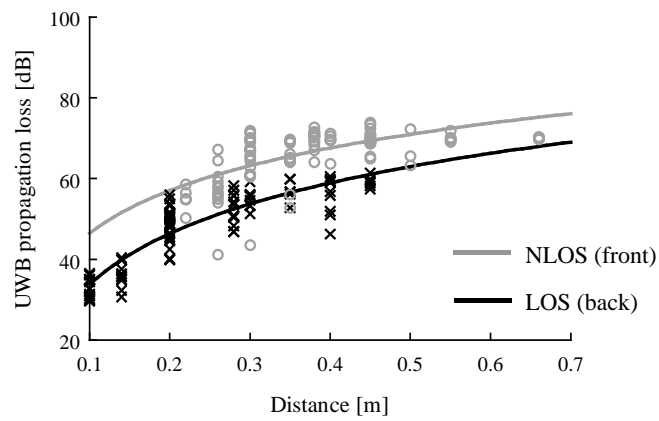
(b)
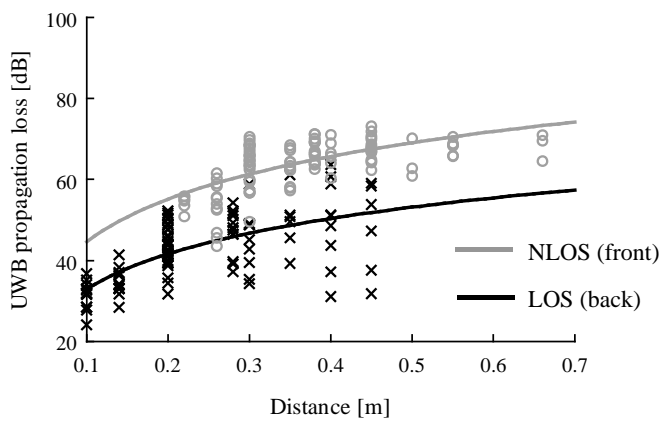
(c)

Fig. 4.5. The propagation loss models along with the measured data in the five environments: (a) Room A (radio anechoic chamber) and (b) Room B to (e) Room E.
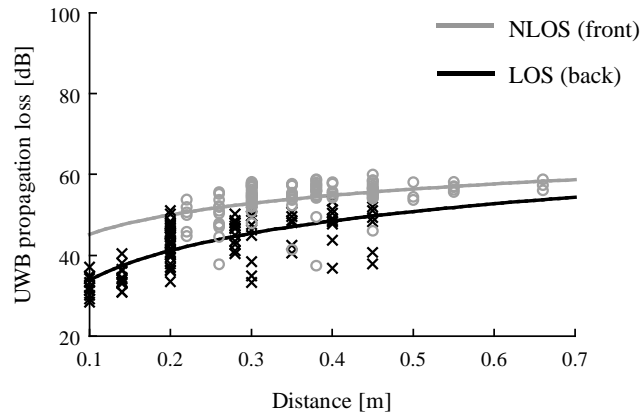
(d)
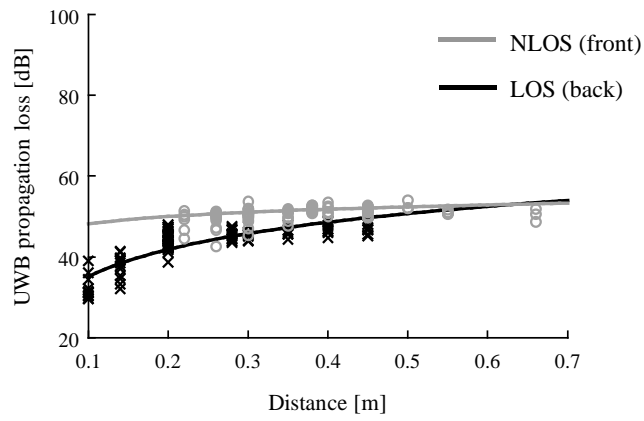
(e)

Fig. 4.5.   Continued.

- In the radio anechoic chamber, $n = 3.4$ for LOS was consistent with the previously-published $n = 3.1$ [22]. However, as shown in Fig. 4.6 (b), in the case of NLOS, $n = 4.8$, 5.9, and 5.9 for the three subjects; as shown in Fig. 4.6 (b); and their average $= 5.5 \pm 1.1$ (95% fidelity interval). The $n = 5.5$ result was significantly smaller than the previously-published $n = 7.2$ [21]. This is most likely due to the fact that the volunteers in the present study were slenderer than those in [21] (our volunteers measured 80 cm around the chest versus more than 100 cm in the previous study), the space under the arms was larger, and thus the power of the diffracted waves was greater.

Table 4.3   Estimated parameters (and ±95% fidelity interval) of the conventional propagation loss model (Eq. (4.2)) in the five environments.

	Parameters	LOS (back)	NLOS (front)
Room A	PL_{0dB} [dB]	32.7 (±2.8)	41.8 (±6.1)
(radio anechoic chamber)	n	3.4 (±0.7)	5.5 (±1.1)
Room B	PL_{0dB} [dB]	33.9 (±1.7)	46.5 (±4.8)
	n	4.2 (±0.4)	3.5 (±0.9)
Room C	PL_{0dB} [dB]	32.9 (±2.6)	44.6 (±4.6)
	n	2.9 (±0.7)	3.5 (±0.8)
Room D	PL_{0dB} [dB]	33.9 (±1.9)	45.2 (±3.6)
	n	2.4 (±0.5)	1.6 (±0.6)
Room E	PL_{0dB} [dB]	35.1 (±1.1)	48.2 (±2.4)
	n	2.2 (±0.3)	0.6 (±0.4)

Scattered plots for PL_{0dB} and n are shown in Fig. 4.6 against $1/\sqrt[3]{V}$, where V is the room volume. These parameters were almost linearly proportional to $1/\sqrt[3]{V}$. Since the dependency of PL_{0dB} on $1/\sqrt[3]{V}$ was observed to be slight, PL_{0dB} was assumed to be constant. The least square method was used to approximate the exponent of n, and then modeled by

$$n(V) = n_\infty + \frac{n'}{\sqrt[3]{V}} , \qquad (4.3)$$

$\sqrt[3]{V}$ represents the mean free path length of the rays traveling within a room having a finite (or infinite) volume V. Note that $n = n_\infty$ when V approaches infinity (corresponding to the free space and radio anechoic chambers). The PL_{0dB}, n_∞, and n' estimated from the data for the three subjects are summarized in Table 4.4, accompanied by the 95% fidelity intervals. Note that the parameters are valid when one of the devices is fixed at the center back waist of the standing human body. Substituting these parameters into Eq. (4.2), a volume-dependent propagation loss model was formulated by

$$PL_{dB} = PL_{0dB} + 10\left(n_\infty + \frac{n'}{\sqrt[3]{V}}\right)\log_{10}\left(\frac{d}{d_0}\right). \qquad (4.4)$$
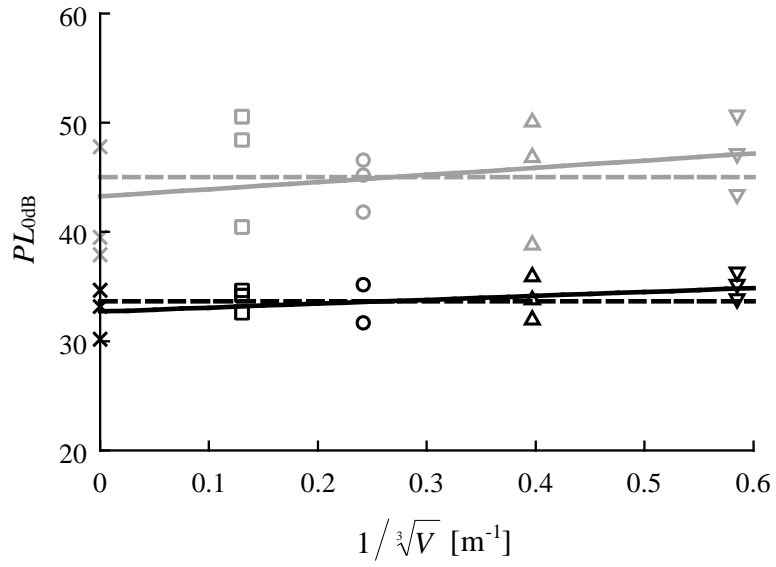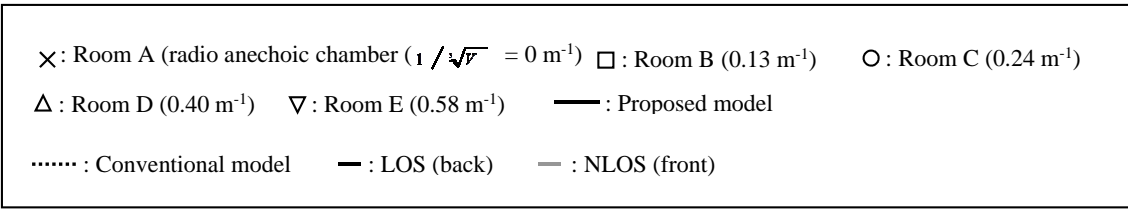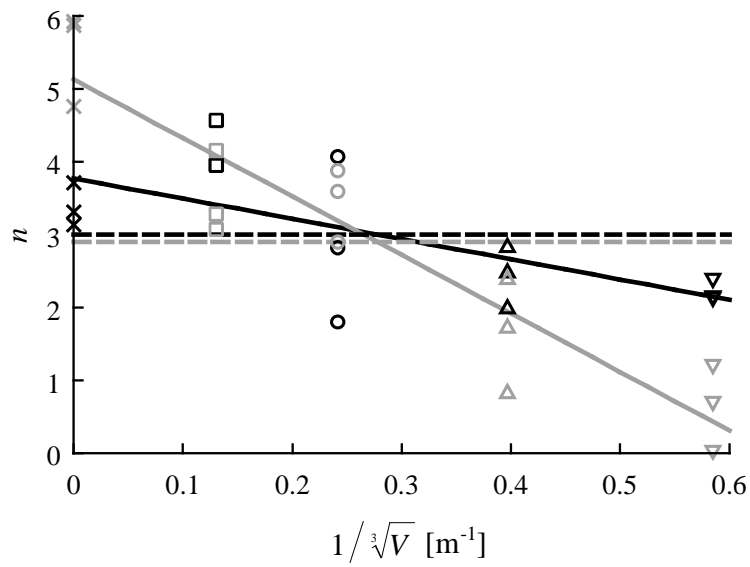
Fig. 4.6. Propagation loss parameters against $1/\sqrt[3]{V}$: (a) PL_{0dB} and (b) n.

Table 4.4 Estimated parameters (and ±95% fidelity interval) of the proposed propagation loss model (Eq. (4.4)).

	Parameters	LOS (back)	NLOS (front)
PL_{0dB} [dB]	PL_{0dB} [dB]	33.7 (±3.6)	45.0 (±9.1)
n	n_∞	3.8 (±0.6)	5.1 (±0.6)
	n' [m]	-2.8 (±1.8)	-8.0 (±1.9)

Table 4.5 The rms errors for PL_{dB} against the proposed and the conventional models.

	LOS (back)		NLOS (front)	
	Proposed	Conventional	Proposed	Conventional
rms error for PL_{dB}	5.57	5.75	4.92	9.25

Next, accuracy in the proposed model was compared with that of a conventional model. PL_{0dB} and n in the conventional model were derived from all the data measured for the three subjects in the five rooms by using Eq. (4.2), as presented by the broken lines in Fig. 4.6. The rms errors for PL_{dB} were calculated for all the data when using the proposed and conventional models, as listed in Table 4.5; and scattered plots of the UWB propagation loss measured for the three volunteers versus the distance and the $1/\sqrt[3]{V}$, along with the proposed and conventional models, are shown in Fig. 4.7. Whereas the rms errors for LOS in the proposed model were slightly smaller than for the conventional model, the rms error for NLOS in the proposed model was considerably smaller than that in the conventional model. Since the dependence of n on the room volume for NLOS was larger than for LOS, as shown in Fig. 4.6 (b), it can be concluded that the proposed model outperforms the conventional one in NLOS environments.

The relation between the occupied bandwidth and the parameters, PL_{0dB}, n_∞, and n' was evaluated, as shown in Fig. 4.8, by fixing the center frequency at 6.85 GHz and changing the bandwidth from 0.5, to 1, 1.5, 3, and 7.5 GHz. The effects of bandwidth on the parameters were found to be negligible.

✕ : Room A (radio anechoic chamber ($1 / \sqrt[3]{V}$ = 0 m^{-1}) □ : Room B (0.13 m^{-1})   ○ : Room C (0.24 m^{-1})

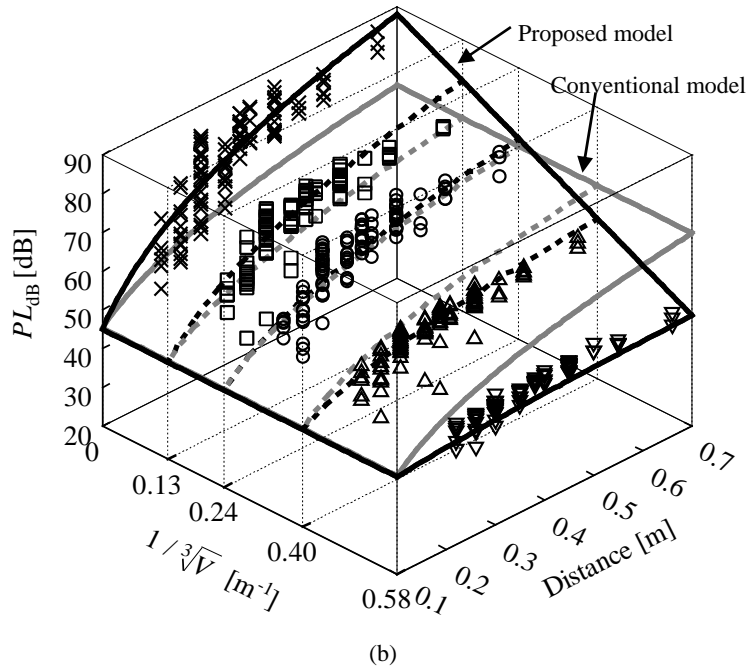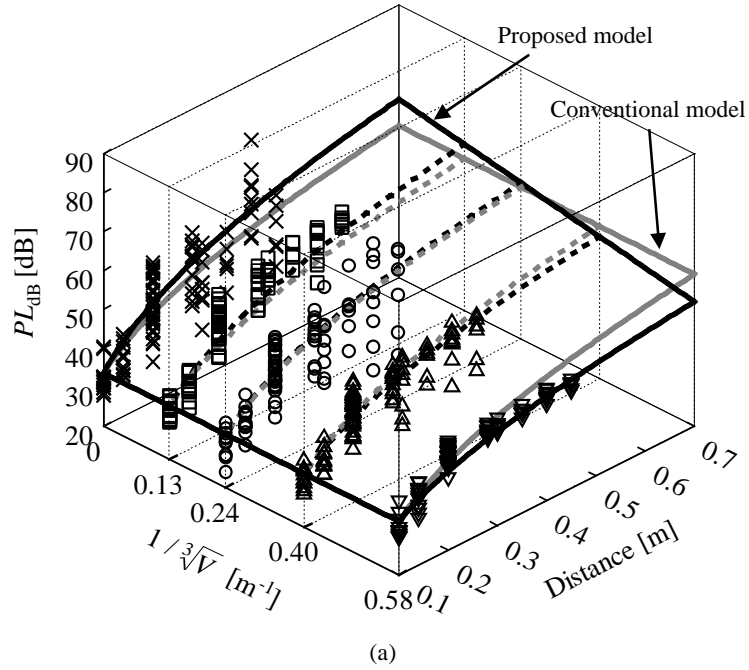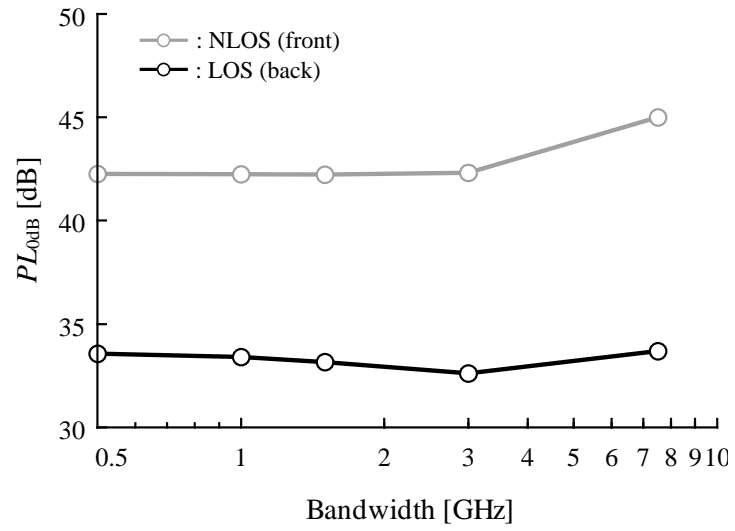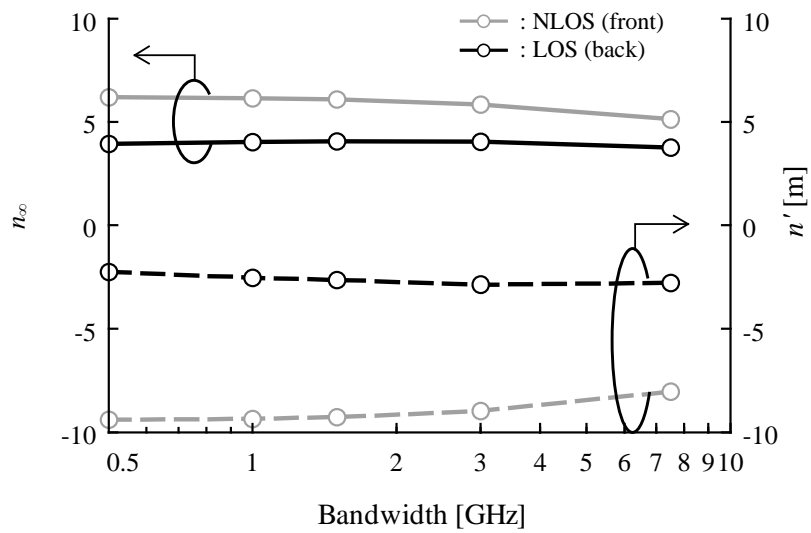△ : Room D (0.40 m^{-1})   ▽ : Room E (0.58 m^{-1})

(a)

(b)

Fig. 4.7.   The proposed and conventional models along with the measured data in the five environments: (a) LOS and (b) NLOS.

(a)

(b)

Fig. 4.8. The relation between the occupied bandwidth and the parameters: (a) PL_{0dB}, and (b) n_∞ and n'.

4.5   Statistical Properties of the UWB Propagation Loss

In addition to the propagation loss model, a statistical model of the amplitude distribution over the surface of the body is considered here. Lognormal distribution has been reported [21] to be an excellent fit to the amplitude data in comparison with the Nakagami-m and Rayleigh distributions for all receiver locations. In this section, the lognormal, Nakagami, and Rayleigh distributions are compared in terms of their ability to estimate a statistical model. As in previous research [21], the second-order corrected Akaike Information Criterion (AIC$_c$) was used to rank the models:

$$\text{AIC}_c = -2\log_e\left(L(\hat{\theta})\right) + 2K + \frac{2K(K+1)}{N-K-1} \qquad (4.5)$$

where $\log_e\left(L(\hat{\theta})\right)$ is the maximized log-likelihood value over unknown parameters (θ), K is the number of parameters in the approximating model, and N is the sample size. A subscript "c" of "AIC" indicates "correct". The lognormal and Nakagami distributions are two parameters ($K = 2$); the Rayleigh is one ($K = 1$). The values of N are 102 and 105, for LOS and NLOS, respectively. This equation is straightforward to compute since the log-likelihood is readily available from the maximum likelihood estimates. Intuitively, the first term indicates that better models have a lower AIC$_c$ because the log-likelihood reflects the overall fit of the model to the data. The second part of the equation penalizes additional parameters ensuring we select models that best fit the data with the least number of parameters. The AIC$_c$ also has a strong theoretical motivation since it provides an estimate of the Kullback–Leibler information loss [50]. In this way, the model with the lowest AIC$_c$ approximates the "true" distribution with minimum loss of information.

In practice, the value of the AIC$_c$ by itself has no meaning. However, the relative values of AIC$_c$ among the models can be used to rank the models from best to worst and to provide strong evidence that one model is better than another. To facilitate this, the related metric is given by [51]:

$$\Delta_i = \text{AIC}_i - \text{Min}(\text{AIC}_i) \qquad (4.6)$$

where AIC$_i$ is the i-th AIC value. Clearly, the best model among the set of models has a delta AIC of 0. As a rule-of-thumb, $\Delta_i < 2$ suggests substantial evidence for the model, values between 3–7 indicate that the model has considerably less support, while values greater than ten indicate that the model is very unlikely [51]. Comparisons of the models fitting amplitude distribution are

shown in Fig. 4.9 in terms of Δ. The lognormal distribution provided the best fit to the cumulative density function (CDF) of amplitudes regardless of the room volume, either NLOS or LOS. The lognormal fittings to the amplitude distributions are shown in Fig. 4.10. The lognormal distribution was defined by

$$f(x|\mu,\sigma) = \frac{1}{x\sigma\sqrt{2\pi}} e^{\frac{-(\ln x - \mu)^2}{2\sigma^2}} \;,$$ (4.7)

where μ and σ are the mean and the standard deviation of amplitude, respectively. The parameters of μ and σ, fitting the measured data, are summarized in Table 4.6. The μ increased with decreasing room volume since the average UWB propagation losses decreased with decreasing room volume, as shown in Fig. 4.3. The σ decreased with decreasing room volume. This is because the valuation of the UWB propagation losses also decreased with decreasing room volume, as shown in Fig. 4.3.

The μ and σ were also almost linearly proportional to $1/\sqrt[3]{V}$, as shown in Fig. 4.11. The least square method was used to approximate the exponent of μ and σ, and the parameters were modeled by

$$\mu(V) = \mu_\infty + \frac{\mu'}{\sqrt[3]{V}}$$ (4.8)

and

$$\sigma(V) = \sigma_\infty + \frac{\sigma'}{\sqrt[3]{V}} \;.$$ (4.9)

Note that $\mu = \mu_\infty$ and $\sigma = \sigma_\infty$ when V approaches infinity. The μ_∞, μ', σ_∞, and σ' estimated from the data for the three subjects are summarized in Table 4.7.
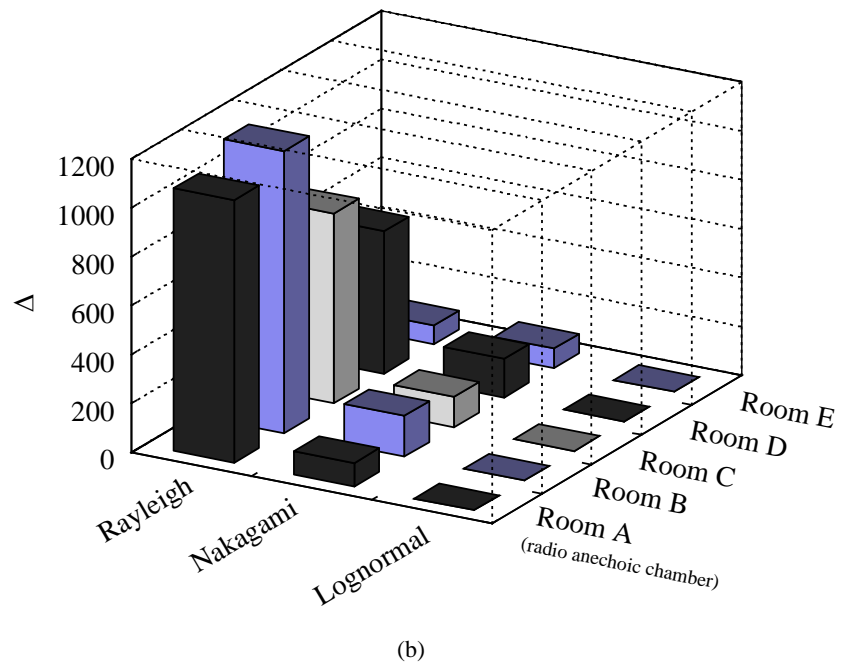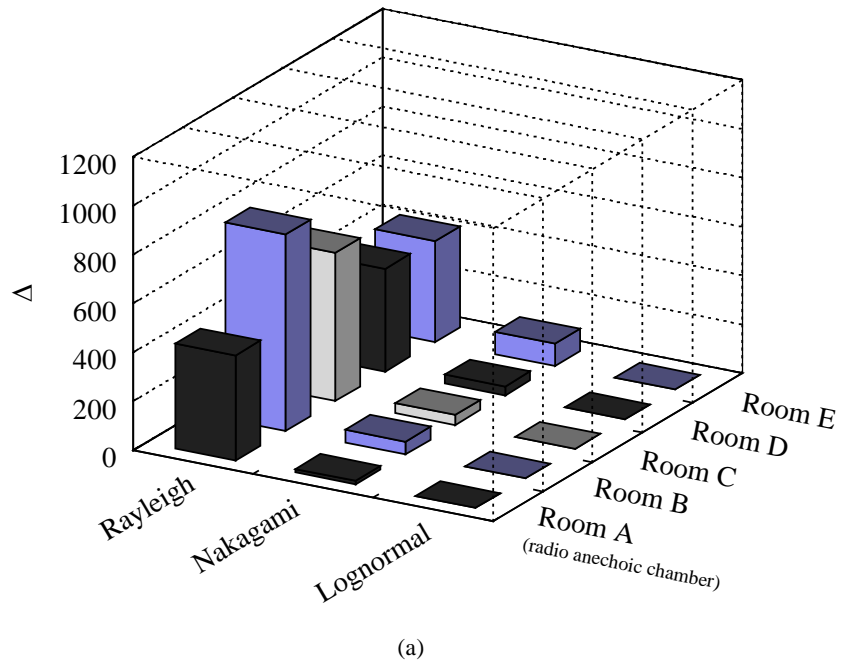
Fig. 4.9.   Comparisons of the models fitting amplitude distribution: (a) LOS and (b) NLOS.
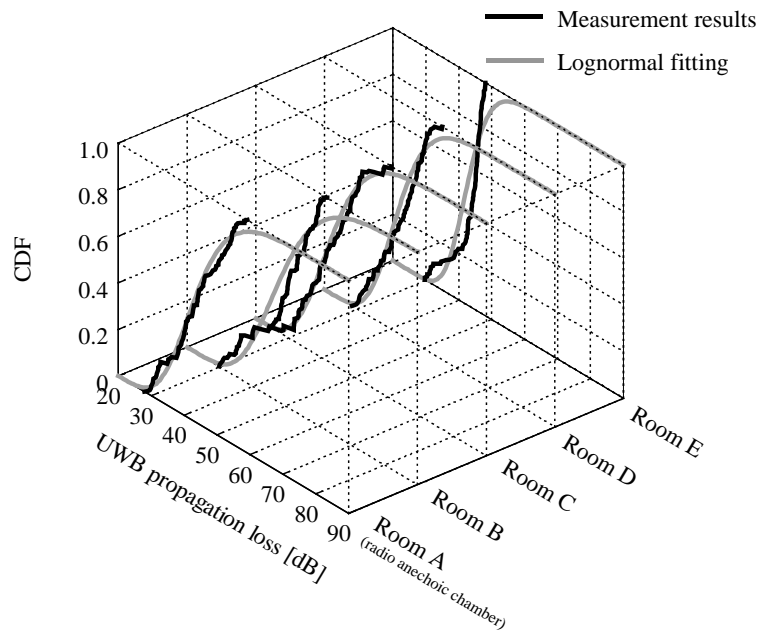
(a)
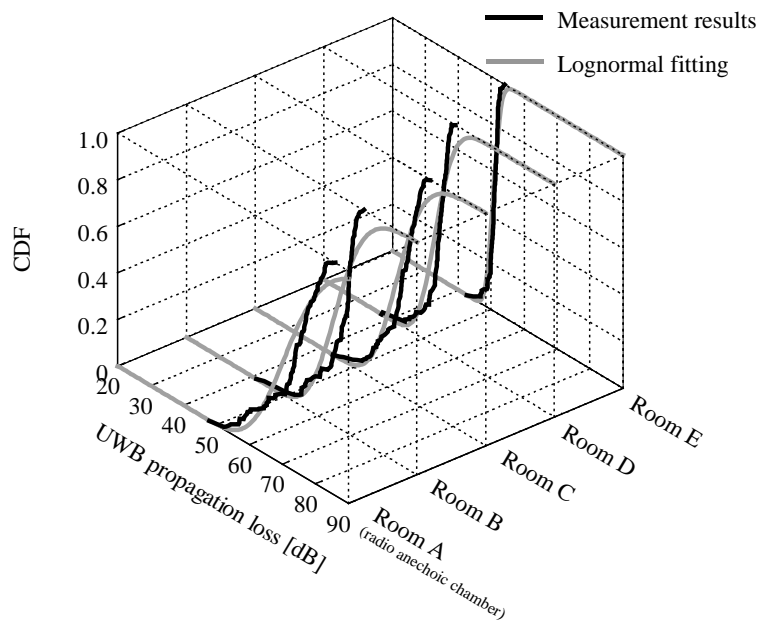
(b)

Fig. 4.10. The lognormal fittings to the amplitude distributions: (a) LOS and (b) NLOS.

Table 4.6   The parameters of μ and σ in Eq. (4.7) fitted to the measured data in the five environments.

	LOS (back)		NLOS (front)	
	μ	σ	μ	σ
Room A (radio anechoic chamber)	-9.7	1.9	-16.6	2.0
Room B	-11.2	2.1	-15.2	1.4
Room C	-9.9	1.9	-14.6	1.4
Room D	-9.8	1.6	-12.5	1.0
Room E	-9.8	1.2	-11.7	0.4

$\times$: Room A (radio anechoic chamber ($1/\sqrt[3]{V}$ = 0 m⁻¹) $\square$: Room B (0.13 m⁻¹) $\bigcirc$: Room C (0.24 m⁻¹)

$\triangle$: Room D (0.40 m⁻¹) ∇ : Room E (0.58 m⁻¹)   ▬ : LOS (back)   ▬ : NLOS (front)
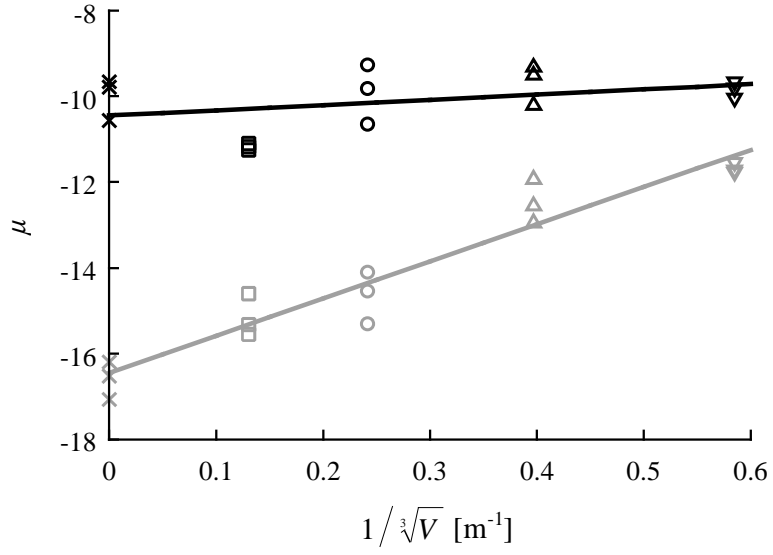
(a)
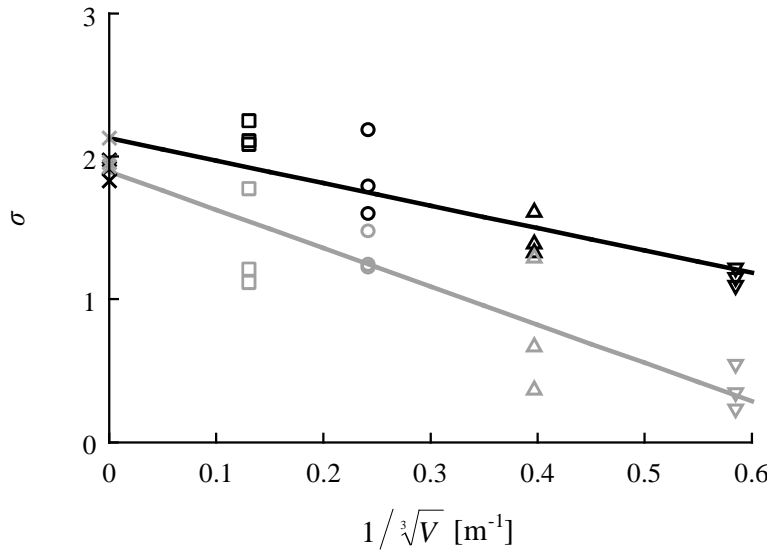
(b)

Fig. 4.11. Lognormal distribution parameters against $1/\sqrt[3]{V}$: (a) μ and (b) σ.

Table 4.7　Estimated parameters (and ±95% fidelity interval) of the lognormal distribution embodying the impact of room volume.

	Parameters	LOS (back)	NLOS (front)
μ	μ_∞	-10.5 (±0.5)	-16.5 (±0.5)
	μ' [m]	1.2 (±1.4)	8.7 (±1.4)
σ	σ_∞	2.1 (±0.2)	1.9 (±0.3)
	σ' [m]	-1.6 (±0.6)	-2.7 (±0.7)

4.6　Summary

This chapter presents the findings from a study of the on-body UWB radio propagation measurements and modeling in five environments, and their volume-dependent modeling. The propagation mechanisms differed among LOS, NLOS, and the surrounding environments as follows:

In a radio anechoic chamber (approximately equivalent to free space), the propagation mechanisms were as follows:

- In the case of LOS, the dominant propagation path was the direct wave.
- In the case of NLOS, the dominant paths were diffracted waves.

In Rooms B to E (multipath environments), however, the propagation mechanisms were as follows:

- In the case of LOS, the dominant path was the direct wave.
- In the case of NLOS, the dominant paths were reflected waves.

These mechanisms resulted in the following phenomena.

In the free space:

- LOS resulted in higher reception.
- NLOS resulted in lower reception than in LOS.

In multipath environments:

- Both LOS and NLOS resulted in higher reception power than in free space.

A conventional UWB propagation loss model (Eq. (4.2)) was modified to include the impact of the room volume and the parameters were derived from the measured data.

- In the case of LOS, PL_{0dB} differed negligibly between the room volumes because the dominant propagation path was the direct wave.
- In the case of NLOS, PL_{0dB} also differed negligibly.
- In the case of LOS, n decreased with decreasing room volume, since in a smaller room the total received power contained more contributions from the large number of multipath components, which were independent of d.
- In the case of NLOS, n also decreased with decreasing room volume.

A new model (Eq. (4.4)) including the impact of room volume was proposed. The parameters in the new model were derived from the measured data for individual body sections. Accuracy in the proposed and conventional models was compared. The rms error for the proposed model was considerably smaller than that for the conventional one. The relation between the occupied bandwidth and the parameters was evaluated. The effects of bandwidth on the parameters were found to be negligible.

Probabilistic distributions of propagation losses, considering the impact of room volume, were also examined. The lognormal distributions were found to provide the best fit to the propagation losses regardless of room-size, although Fort et al. [21] reported that lognormal distributions were a good fit to the path losses measured in an indoor environment. The parameters of lognormal distributions were derived from the measured data. The μ and σ increased and decreased with decreasing room volume, respectively. This is because the UWB propagation losses decreased with decreasing room volume.

Chapter 5

Statistical Modeling of UWB Wireless Channels Around the Human Body Considering Room Volume

5.1   Objectives

In Chapter 4, we measured UWB (3.1 - 10.6 GHz) radio propagation characteristics around the human body in a radio anechoic chamber and four different rooms, and proposed a new UWB propagation loss model depending on the room volume. In this Chapter, a time-domain statistical channel model, based on the same measurement campaign as in Chapter 4, will be presented [52].

As for statistical modeling of the channel impulse response, Fort et al. [19] separated the WBAN propagation channels into two parts: (1) diffraction around the body and (2) reflections off of nearby scatterers then back at the body, and modeled the second part using a modified SV model [53]. The applicable area of the modified SV model in [53], however, was limited to WPAN not including human bodies. Roblin [54] scrutinized the separability of channels for various scenarios in three different rooms, and concluded that UWB channels can be separated in the case of a relatively larger room, but Roblin [54] has not developed a channel model. Previous studies, then, have not reported a statistical channel model around the human body while also considering room volume. Multipath components (mainly reflected from floor, ceiling, and walls) are highly dependent on the environment, so it is necessary to establish a channel model dependent on room volume for WBAN applications. We also divided the channel responses into two parts which were then modeled by power decay law and a modified SV model that took account of room volume.

69

5.2   Measurement Set-up

The measurement set-up used to extract the static modeling is summarized here. The measurement campaigns were conducted in five parallelepiped rooms, as shown in Table 4.1 and Fig. 4.1. Room A (a radio anechoic chamber) can be considered a room extending to an infinite volume (i.e. a free space) in terms of its radio propagation environment. Rooms B to E were made of reinforced concrete. Their floors, walls, and ceilings were mostly covered with linoleum, wallpaper, and plasterboard, all of which had lossy dielectrics. The measurements were carried out using a human subject (adult male, 1.72 m tall and 56 kg). The subject stood upright with the feet shoulder-width apart in either a quiet zone of the radio anechoic chamber or in the center of Rooms B to E. The UWB (3.1 - 10.6 GHz) on-body propagation losses were measured by the VNA. The same small low-profile meanderline antennas [43] were used for all measurements. The transmitting antenna was affixed to the center back waist of the subject and placed at a height of 1.0 m from the floor, as shown in Fig. 4.2. The receiving antenna was placed at approximately 100-mm intervals on the torso. When the receiving antenna was placed on the back of the subject's body, the path was roughly LOS, and when on the front, it was NLOS. The frequency-domain was obtained by taking the IFT of a delay profile. Section 4.2 provides a more detailed description.

5.3   Modeling

5.3.1 Division of Propagation Channels

A delay profile can be treated by dividing it into two domains, in the same way as in [19], [54]: the first (approximate arrival time $0 < t \leq 4$ ns) and second ($t > 4$ ns) domains, as schematically shown in Fig. 5.1. The first domain represents the contribution of the human body alone, consisting of either direct (for LOS) or diffracted (for NLOS) waves measured in free space or radio anechoic chambers. And the second domain represents the contribution of the surrounding environments, consisting of the remaining multipath components, which depend on room volume. The justification for dividing the profiles at $t = 4$ ns is as follows. Figure 5.2 depicts APDPs (averaged over 3 ns) for LOS and NLOS measured in Rooms A to E. The curves are almost equal for the period between 0 and approximately 4 ns: the effect of the surrounding environment was insignificant up to 4 ns. Beyond 4 ns, the propagation loss decreased (the curves move upward) with decreasing room volume. Furthermore, the amplitude distribution was examined to confirm the validity of $t = 4$ ns for dividing the delay profiles. The amplitudes within the measured delay profiles were found to follow lognormal distribution up to an excess delay of 10 ns. The averages in the lognormal distribution up to 3, 4, 5, and 7 ns were estimated for LOS and NLOS, as shown in Fig. 5.3, where the 95% confidence intervals derived from the Room A data are plotted by dashed lines. While all the averages up to 4 ns for Rooms B to E fell within the 95% intervals, some (Rooms C, D, and E for LOS and Rooms D and E for NLOS) were outside these intervals, as shown in Fig. 5.3. This fact also ratified the validity of $t = 4$ ns for dividing the profiles.
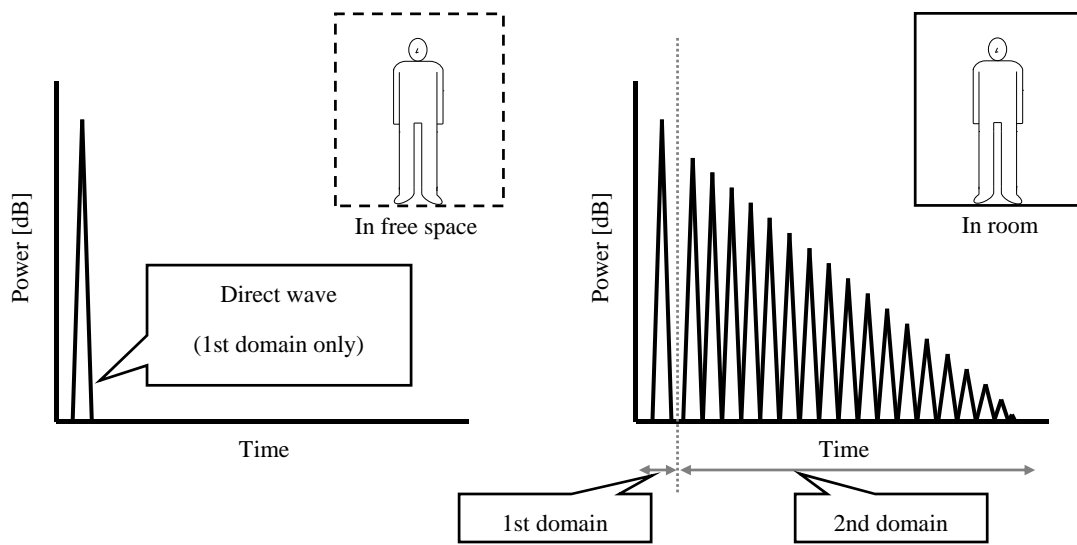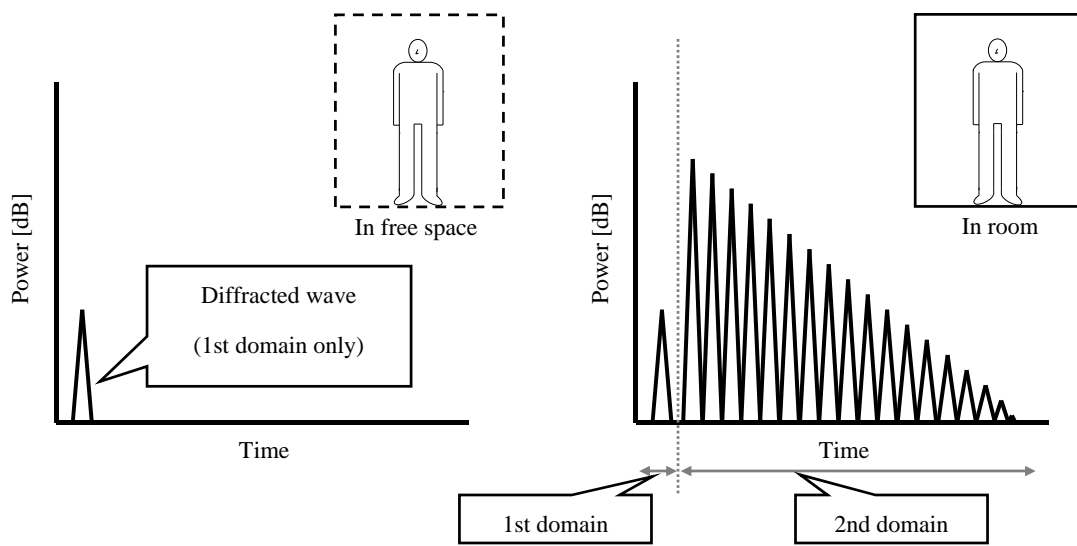
Fig. 5.1.   Conceptual diagram of division of the delay profiles: (a) LOS and (b) NLOS. The first domain represents the delay profiles measured in free space or radio anechoic chambers and contain direct or diffracted waves along the body. The second domain consists of the remaining multipath components.
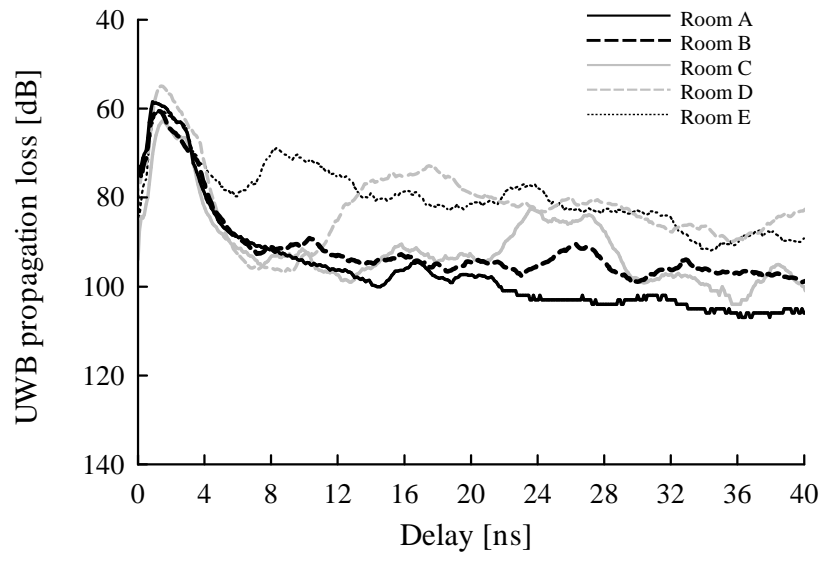
(a)
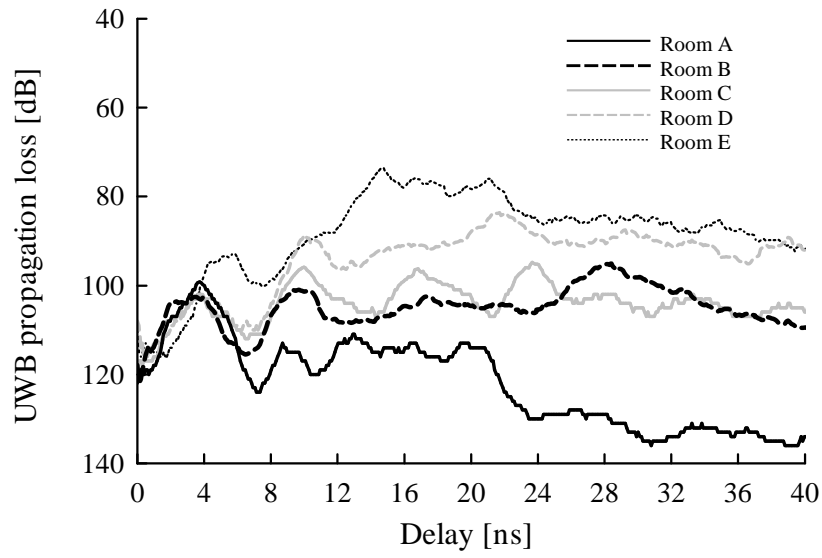
(b)

Fig. 5.2.   Measured APDPs (averaged over 3 ns): (a) LOS and (b) NLOS.
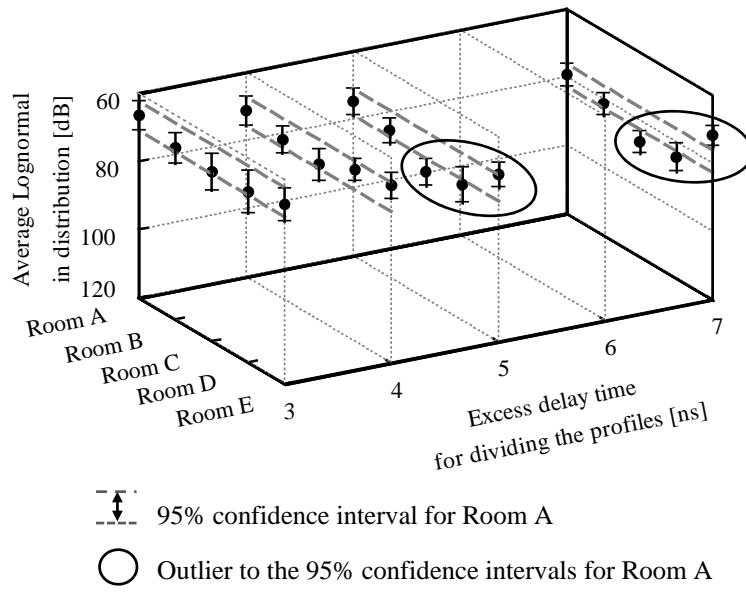
(a)
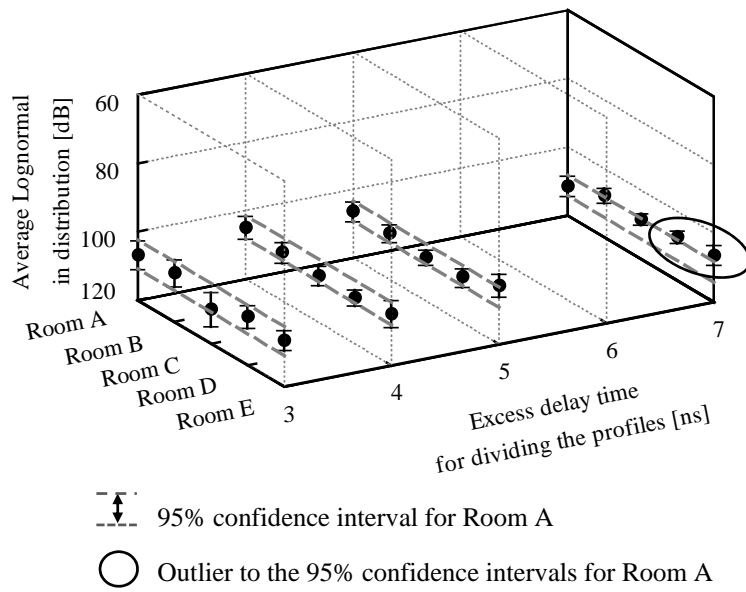
(b)

Fig. 5.3. Averages in lognormal distribution fitted to the propagation loss for Rooms A to E: (a) LOS and (b) NLOS. The dashed lines are the 95% confidence intervals for Room A (a radio anechoic chamber). The averages circled by ovals are outliers to the 95% intervals for Room A.

5.3.2 Statistical Analysis of the First Domain

The channel response in the first domain ($0 < t \leq 4$ ns) can be represented by

$$h_1(t) = h_{10} \cdot \left(\frac{d}{d_0}\right)^n \cdot \delta(t - t_0), \qquad (5.1)$$

where h_{10} is the propagation gain at the reference distance d_0 (= 0.1 m), d is the propagation distance along the perimeter of the body, n is the propagation loss exponent, t_0 is the arrival time of the first wave, and $\delta(\cdot)$ is the Dirac delta function. The arrival time t_0 is proportional to d. Equation (5.1) represents a special case (when the room volume $V = \infty$) of the proposed UWB propagation loss model depending on room volume [47], as described in section 4.3. The values of h_{10} and n in Eq. (5.1) were found to be 4.3×10^{-4} and 3.8 for LOS and 3.2×10^{-5} and 5.1 for NLOS, respectively, from the data for PL_{dB} shown in Fig. 5.4. The statistics for $h_1(t)$ followed lognormal distribution with a standard deviation of 4.4 dB ($\pm$ 0.5 dB) and 3.4 dB ($\pm$ 0.5 dB), for LOS and NLOS, respectively, where the values in parentheses indicate 95% confidence intervals.
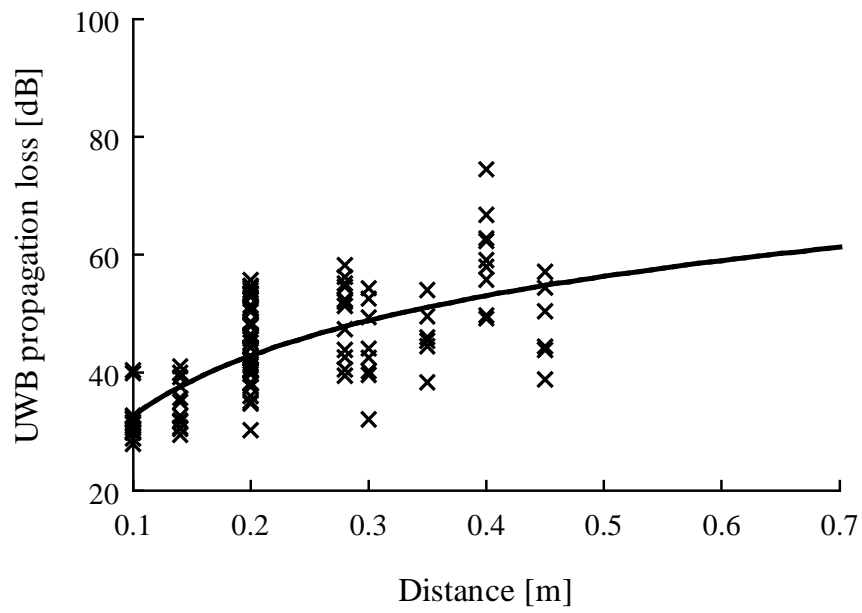
(a)
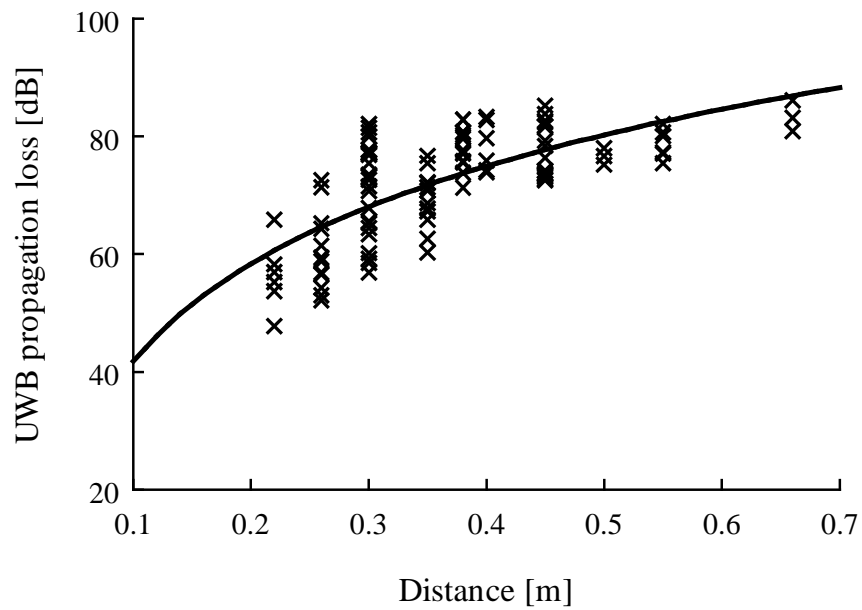
(b)

Fig. 5.4.   Ultra-wideband propagaion losses between on-body antennas measured in a radio anechoic chamber: (a) LOS and (b) NLOS.

5.3.3 Statistical Analysis of the Second Domain

The second domain ($t > 4$ ns) can be represented by a modified SV model [55] based on a cluster concept of rays:

$$h_2(t) = \sum_{l=0}^{\infty} \sum_{k=0}^{\infty} \beta_{k,l} \delta(t - T_l - \tau_{k,l}),$$ (5.2)

where $\{\beta_{k,l}\}$ are the multipath gain coefficients, $\{T_l\}$ is the delay of the l-th cluster, and $\{\tau_{k,l}\}$ is the delay of the k-th multipath component relative to the l-th cluster arrival time (T_l). Figure 5.5 demonstrates the concept of clusters and rays. Each cluster is formed by the reflection of UWB waves from different objects, for example one cluster may represent the reflected signals from a wall and another cluster the signals reflected from a desk located a couple of meters away. The modified SV model is the standard for modeling UWB channels established by the IEEE 802.15 task group. Delay profiles measured in Rooms B, C, D, and E indicated that rays arrived in clusters, as shown in Fig. 5.6, where the abscissas of the graphs are drawn in antilogarithm to improve readability. The first wave of the second cluster yielded higher reception power than the first wave of the first cluster, as shown in Fig. 5.6 (b), (d), and (e). This is because multipath waves that traveled the same propagation length combined at the receiving antenna; or the reflected object differed between the first and second clusters. Although the difference did not exceed 1 dB between the first waves of the first and the second clusters, we modeled using the first cluster. While Fort et al. stated that the cluster interval times fitted the Weibull distribution [19], in all our cases, the arrival time intervals of the clusters were found on using the Kolmogorov-Smirnov test with a 95% confidence interval to follow an exponential distribution. This means that cluster arrivals are modeled as a Poisson arrival process with a fixed rate of Λ [1/ns]. Within each cluster, subsequent rays also arrived according to a Poisson process with another fixed rate of λ [1/ns]. The distribution of the cluster and ray arrival times are given by

$$p(T_l \,|\, T_{l-1}) = \Lambda \exp[-\Lambda(T_l - T_{l-1})], \qquad l > 0$$ (5.3)

and

$$p(\tau_{k,l} \,|\, \tau_{(k-1),l}) = \lambda \exp[-\lambda(\tau_{k,l} - \tau_{(k-1),l})], \quad k > 0,$$ (5.4)

where Λ and λ are cluster arrival rate and ray arrival rate within each cluster, respectively. The IEEE 802.15.4a channel model [53] used a lognormal distribution rather than the Rayleigh

distribution adopted in the original SV model [55] for the multipath gain coefficients $\beta_{k, l}$. We also adopted a lognormal distribution for $\beta_{k, l}$ because this gave a better fit to the measured data. The average power of both the clusters and the rays within the clusters are assumed to decay exponentially, such that the average power of the multipath component at a given delay $T_l + \tau_{k,l}$ is given by

$$\left\langle \beta^2_{k,l} \right\rangle = \left\langle \beta^2_{0,0} \right\rangle \exp\left(-\frac{T_l}{\Gamma}\right) \exp\left(-\frac{\tau_{k,l}}{\gamma}\right),$$ (5.5)

where $\langle \beta^2_{0, 0} \rangle$ is the expected value of the power of the first arriving multipath component, Γ is the delay exponent of the clusters, and γ is the decay exponent of the rays within a cluster. The power of the first arriving multipath detected in measured delay profiles is lower with decreasing room volume, as shown in Fig. 5.7. The power of the first multipath component, $\langle \beta^2_{0, 0} \rangle$, can be represented by

$$\left\langle \beta^2_{0,0} \right\rangle = \beta_0 \cdot \left(\sqrt[3]{V} \right)^v.$$ (5.6)

The values of β_0 and v were calculated by using the measured delay profiles, as listed in Table 5.1.

The values of Λ, λ, Γ, and γ were derived from the delay profile data measured in Rooms B, C, D, and E. Figures 5.8 and 5.9 present those values against $V^{1/3}$ along with regression lines. Note that $V^{1/3}$ represents the mean free path length of the rays traveling within a room having a finite (or infinite) volume V. The cluster arrival time rate Λ [1/ns] is approximately 0.08, while the ray arrival time rate λ [1/ns] is 0.4 for both LOS and NLOS. While the arrival rates Λ and λ exhibited no apparent dependence on $V^{1/3}$ or LOS/NLOS scenarios as shown in Fig. 5.8, the power decay factors Γ and γ increased slightly with $V^{1/3}$, as shown in Fig. 5.9. The propagation distances (and therefore propagation losses) of rays increase with the room volume, and therefore the decay factors increase. The slope of the NLOS scenario was steeper than that for the LOS scenario. The dependence of the cluster power-decay factor and the ray power-decay factor on $V^{1/3}$, depicted in Fig. 5.9, is formulated by

$$\Gamma = \Gamma_0 + \Gamma'' \cdot \sqrt[3]{V}$$ (5.7)

and

$$\gamma = \gamma_0 + \gamma' \cdot \sqrt[3]{V} \;,$$ (5.8)

where Γ_0 and γ_0 are values of Γ and γ when imaginarily $V = 0$, Γ' and γ' are the slope of the cluster and the ray within the cluster against $V^{1/3}$, respectively. The values of Γ_0, γ_0, Γ' and γ' are listed in Table 5.2. Although the effect of shadowing has not been considered in this chapter, it can be included in Eq. (5.2) after using the same method as adopted in [53].
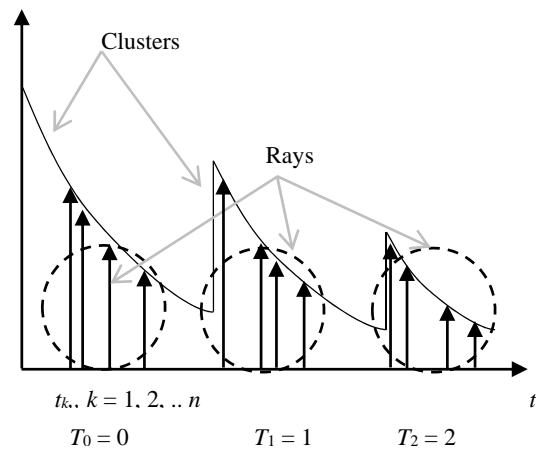
Fig. 5.5. Illustration of Clusters and Rays (notice that clusters and rays decay exponentially) [53], [55].
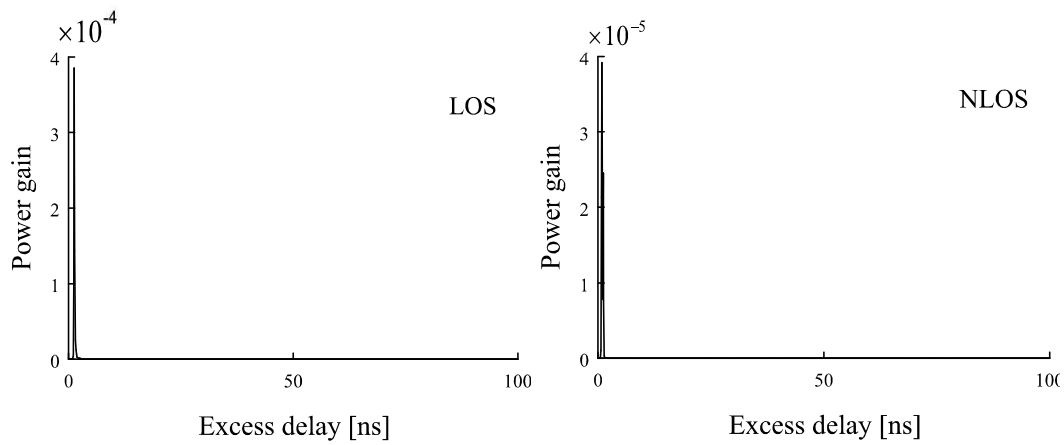
(a)

Fig. 5.6. Examples of the delay profiles measured in Rooms A to E. Profiles for LOS were measured at the center of the back and those for NLOS at the center of the chest. The dashed lines represent the exponential power decay of the rays and clusters. The black and grey arrows indicate the first and second domains.
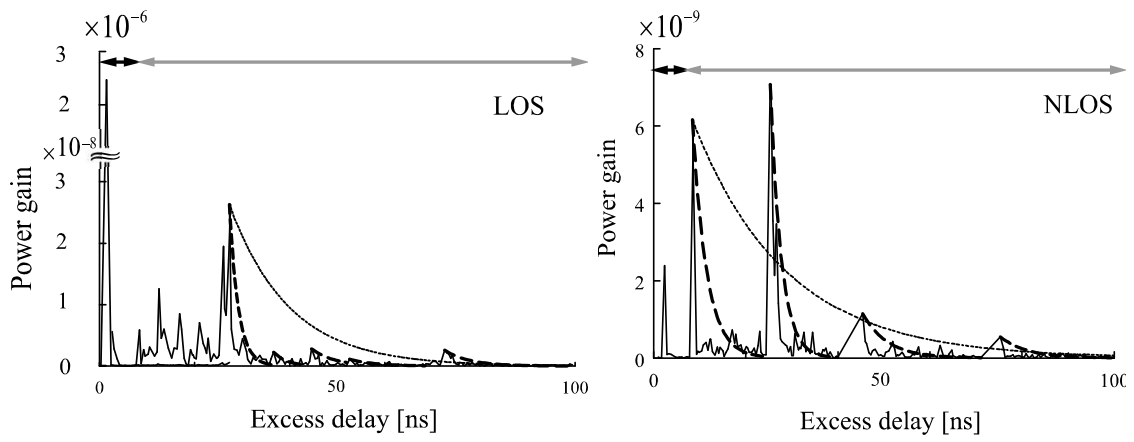
(b)
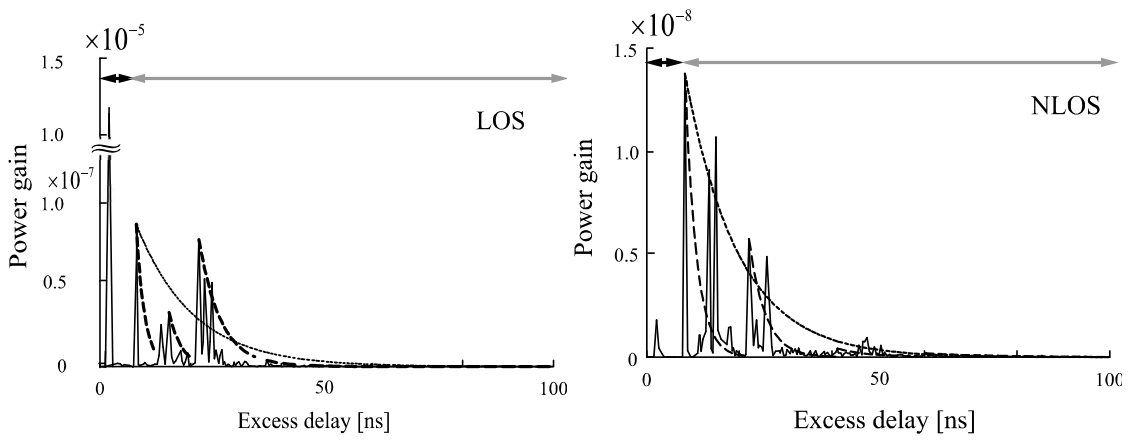
(c)

Fig. 5.6.   Continued.
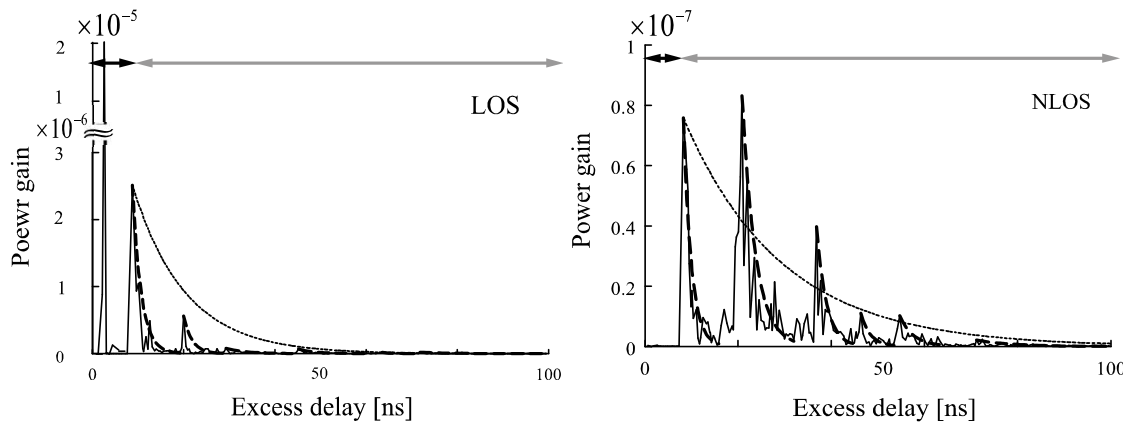
(d)
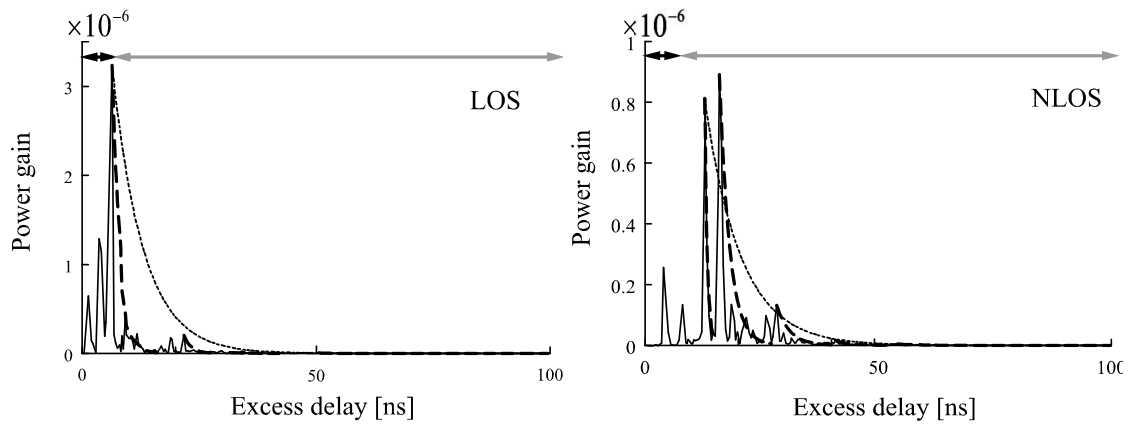
(e)

Fig. 5.6.   Continued.
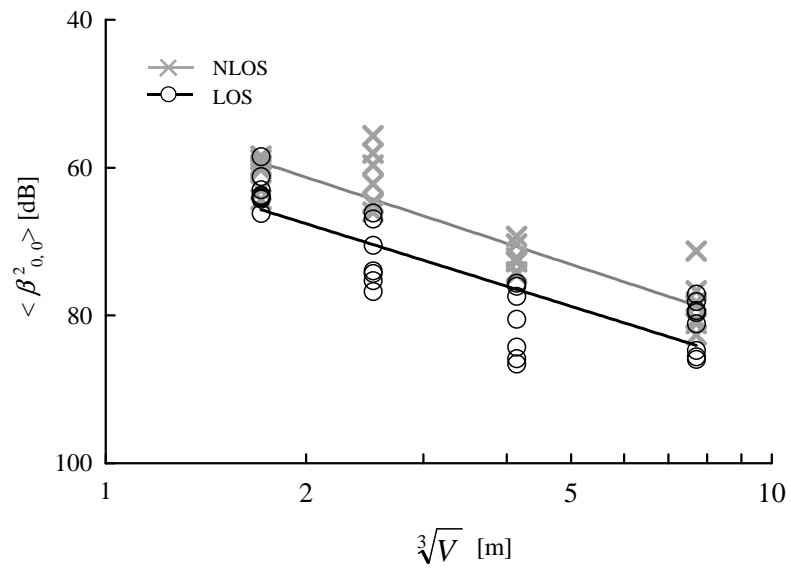
Fig. 5.7.　UWB propagation loss of the first ray within the first cluster against $V^{1/3}$.

Table 5.1　Parameters of the first arriving multipath component.

	NLOS	LOS
v	-2.8	-3.0
β_0	59.1	52.4
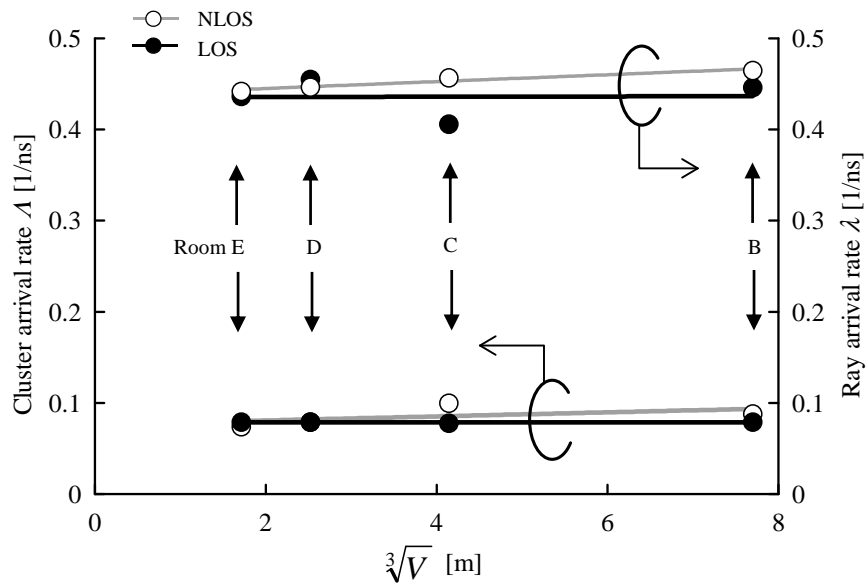
Fig. 5.8.   Arrival rates of clusters and rays within clusters.
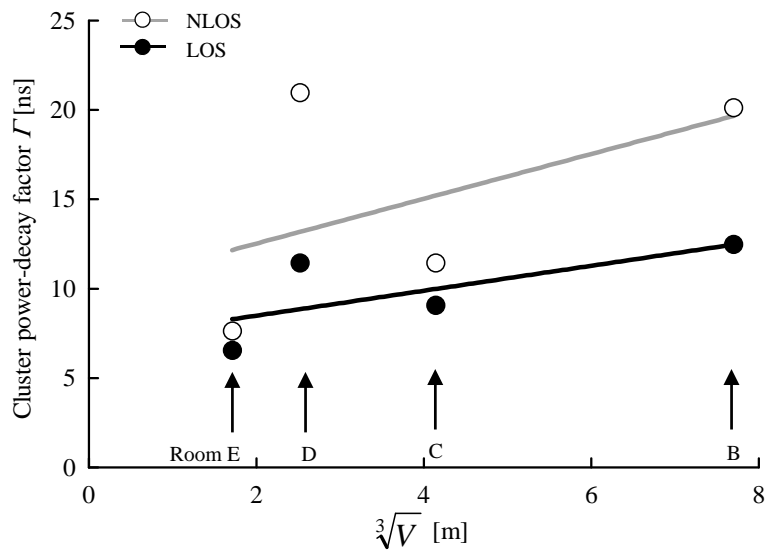
(a)

Fig. 5.9.   Power decay factors against $V^{1/3}$ for (a) the clusters and (b) the rays. The solid lines are the linear fitting.
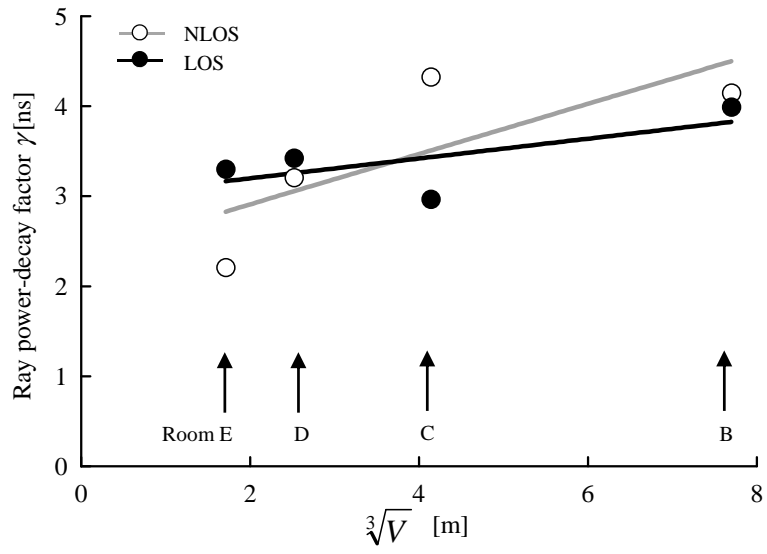
(b)

Fig. 5.9.   Continued.

Table 5.2   The parameters for the cluster and the rays within the cluster.

		NLOS	LOS
Cluster	Γ [ns/m]	1.25	0.70
	Γ_0 [ns]	10.0	7.1
Ray	γ' [ns/m]	0.28	0.11
	γ_0 [ns]	2.4	3.0

5.4 Realization of On-Body UWB Channels Based on the Composite Model

A composite statistical UWB channel model between on-body antennas is formulated by summing the models described in Section 5.3. We used the realization programs described in [53]. A realization is calculated upon providing input data – whether the path is either LOS or NLOS d – (the distance between the antennas along the perimeter of the body), and the room volume, as shown in Fig. 5.10. Once a number of realizations of the channel responses have been calculated randomly (= 100 times), this is then used to estimate the transmission performances and/or system capacity of communication systems, the detection and false alarm rates of radar systems, and so forth, by simulation.

Examples of the channel response realizations for LOS and NLOS, assuming d = 200 mm for LOS and 450 mm for NLOS and V = 5 m^3, are presented in Fig. 5.11, where 20 realizations are overwritten. The APDPs for LOS and NLOS were derived from these realizations and compared with the measured data. The moving average was conducted over a 3-ns period to calculate the APDPs. The APDPs derived from the calculated realizations and from the measured delay profiles agree reasonably well, as shown in Fig. 5.12. The validity of the proposed composite model was therefore confirmed.
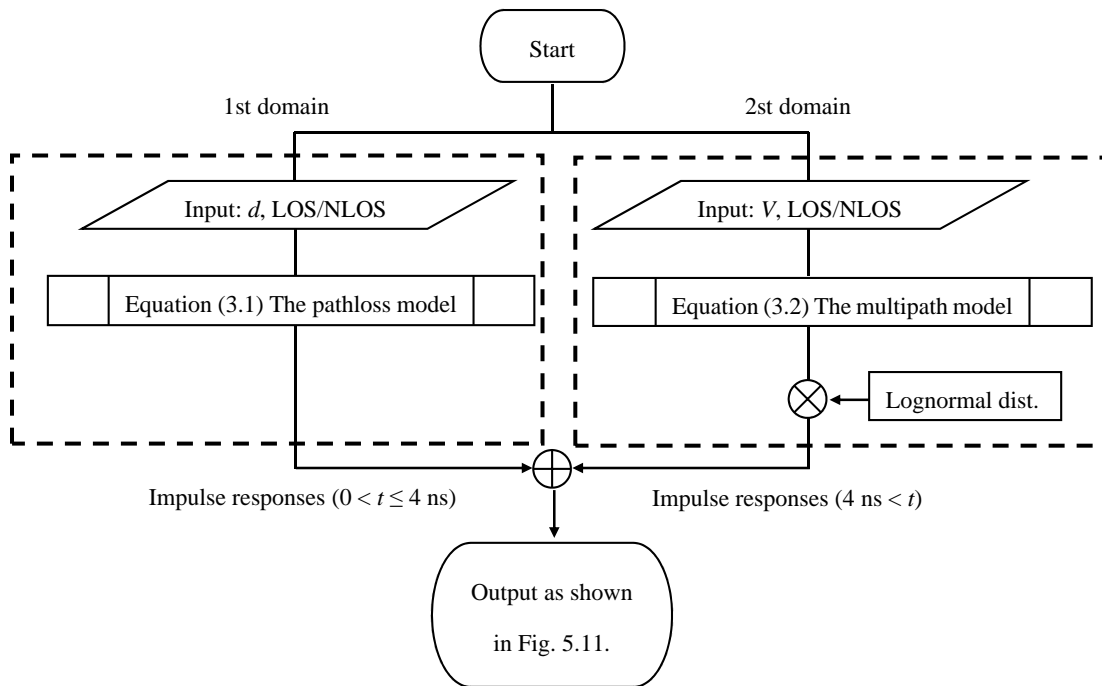
Fig. 5.10.   Flow chart showing the model realization process.
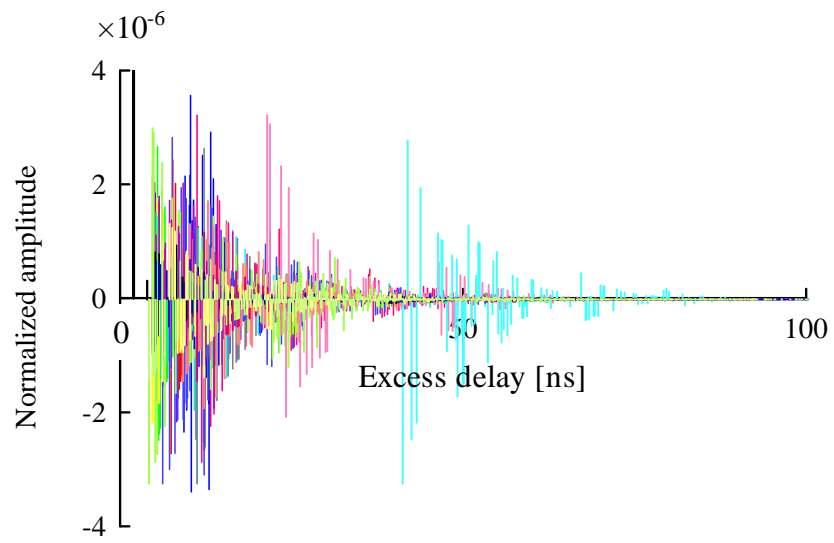
(a)
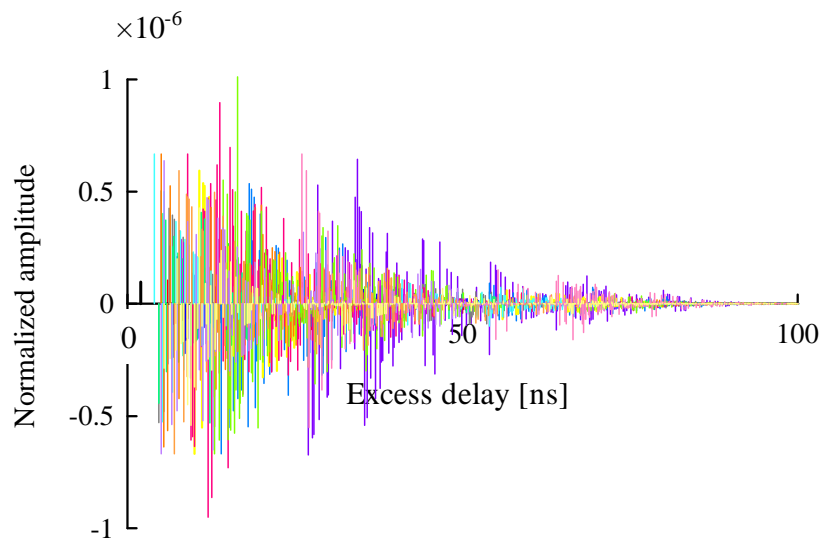
(b)

Fig. 5.11.   Examples of 20 channel response realizations for Room E ($V = 5$ m^3): (a) LOS and (b) NLOS. Note that normalized amplitude 1 = 0 dB.
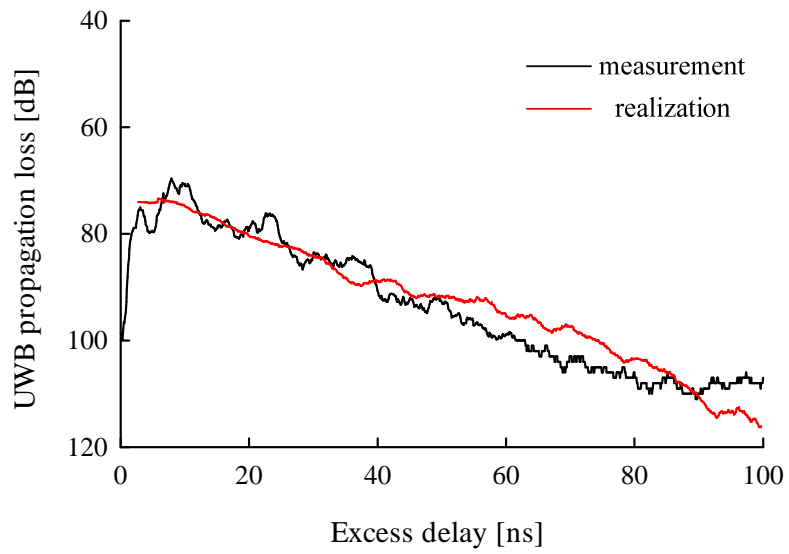
(a)
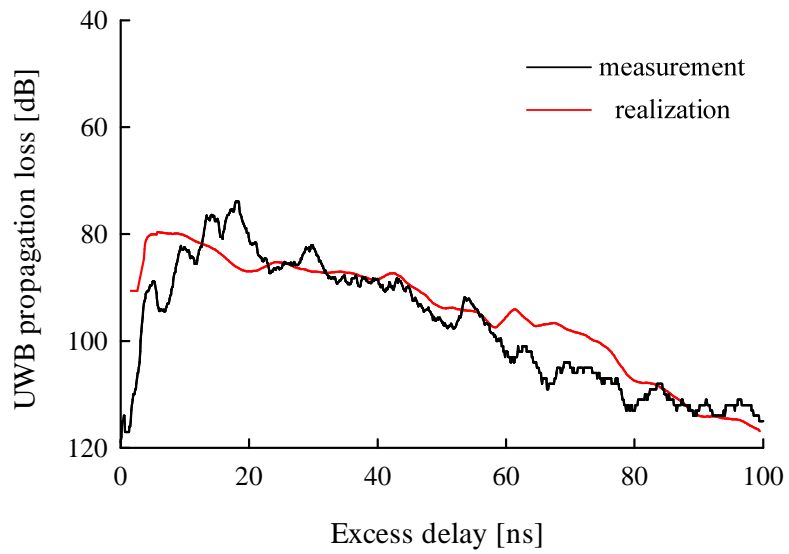
(b)

Fig. 5.12.   Comparison of the APDPs between 20 realizations and measured delay profiles for Room E ($V = 5$ m³):

(a) LOS and (b) NLOS.

5.5   Summary

In this chapter, a series of propagation measurement campaigns were carried out between on-body antennas in five different rooms. A measured delay profile can be divided into two domains. In the first domain ($0 < t \leq 4$ ns), there is either a direct (for LOS) or diffracted (for NLOS) wave which depends on propagation distance along the perimeter of the body but is essentially unrelated to room volume. This domain was modeled with a power decay law against the distance, and its amplitude followed a lognormal distribution. In the second domain ($t > 4$ ns), multipath components are dominant and dependent on room volume. Observations of the second domain indicate that rays generally arrive in clusters. The arrivals of clusters and rays within each cluster were found to be modeled by Poisson processes. As a result, the second domain was modeled by a modified SV model by using a lognormal distribution rather than a Rayleigh distribution for multipath gain coefficients. Finally, a composite model to calculate the UWB on-body channel realizations was obtained by combining the two domains, and validated by using the measured delay profiles.

Chapter 6
Conclusions

This dissertation presents UWB radio propagation measurements and modeling around the human body envisioned for WBAN. The targets of this study are mainly the off-body measurements, the radio propagation measurements around the human body in the five environments, and a modeling of UWB propagation losses and delay profiles that takes account of the impact of room volume.

Chapter 2 described how a liquid UWB phantom material simulating human muscle was developed for experimental studies on antenna and propagation. An aqueous solution of sucrose ($C_{12}H_{22}O_{11}$, 1.0 mol/l) provided the best result within a UWB bandwidth of 3.1 to 10.6 GHz. The effects of errors in realizing $\dot{\varepsilon}$ of muscle were analytically evaluated by assuming the typical shapes of reflecting and scattering objects. The errors for reflected or scattered waveforms were small. Next, the effects of the feeding cable configuration on UWB radio propagation were measured. It was found that careful attention should be paid to the cable configuration when electrically-small large VSWR antennas are used. It was also found that a perpendicular configuration of transmitting and receiving antennas without crossing yielded the least coupling.

Chapter 3 examined the UWB propagation gains between a base station and on-/off-body antennas. The maximum plunges in the relative path gains when the human arm and torso blocked the propagation paths were found at up to 9 to 11 dB and 25 to 28 dB, respectively. In addition, UWB arm and torso phantoms developed using a liquid recipe (1.0 mol/l aqueous solution of sucrose) were also employed. The performances of the arm and torso phantoms were almost the same as those of the human body.

The UWB propagation losses around the human body and propagation loss models dependent on room volume were described in Chapter 4. The measurement campaigns were conducted in the parallelepiped rooms; Room A (a radio anechoic chamber) and Rooms B to E (made of reinforced concrete). The propagation losses decreased with the decreasing room volume. This was attributed to the large number of multipath components from the nearby floor, walls, and ceiling in Rooms B to E. The dominant propagation path in Room A was either a direct or a diffracted wave, and therefore the total reception power was lower than in the other rooms. With decreasing room volume, mean free path lengths decreased, the power component contained in the multipath components increased, and consequently the total received power increased. The

parameters in the conventional UWB propagation loss model were derived from measured results and it was found that the models depend on the room volume and whether the waves were LOS or NLOS. A new model taking into account the impact of the room volume was proposed and its parameters were estimated. The probabilistic distributions of propagation losses were also examined, and lognormal distribution was found to yield the best fit.

Finally, in Chapter 5, statistical modeling of UWB channels around the human body dependent on room volume was described. A measured delay profile can be divided into two domains. In the first domain ($0 < t \leq 4$ ns), there is either a direct (for LOS) or diffracted (for NLOS) wave which depends on the propagation distance along the perimeter of the body but is essentially unrelated to room volume. This domain was modeled with a power decay law against the distance, and its amplitude followed a lognormal distribution. In the second domain ($t > 4$ ns), multipath components are dominant and dependent on room volume. Observations of the second domain indicate that rays generally arrive in clusters. The arrivals of clusters and rays within each cluster were found to be modeled by Poisson processes. As a result, the second domain was modeled using a modified SV model and lognormal distribution rather than Rayleigh distribution for multipath gain coefficients. The composite model used to calculate the UWB on-body channel realizations was obtained by combining the two domains, and validated with the use of the measured delay profiles.

● **Future Research Topics**

This dissertation focuses on the statistical characteristics associated with a standing posture. Previous studies, however, provide channel models with an emphasis on various body postures or body movement [56], [57]. Quantitative performance evaluation of various body postures in different surrounding environments will be our future subject of study.

While full-band UWB is legally approved in the US and Singapore, most countries restrict the use of separate low- and high-band UWB, as described in Section 1.1. Characterization and modeling for the two bands should be split and scrutinized from the viewpoint of the volume-dependent UWB propagation loss model, the statistical model of the UWB propagation losses, and the statistical modeling of the channel responses.

In recent years, UWB radio propagation around human legs has been reported [27], [58], [59], although mostly previous studies have focused on the human torso. The target applications for human legs include rehabilitation, gait analysis, and sports science. We have measured around the lower body section including the legs in the five environments. The parameters of the

conventional propagation loss model were calculated from the measured data, and the value of n was negative [60]. But we have not yet fully understood this phenomenon. So it will be necessary to conduct further research since the characteristics of radio propagation around the human legs will have implications for the development of new applications using UWB technology.

In this thesis, the measurement campaigns were derived from the three volunteers. Their physiques were almost the same. The effects of UWB propagation losses between different subjects of various statures and shapes were measured in an indoor environment; the maximum variation in UWB propagation losses was 14.2 dB [61]. It is necessary to evaluate the effects of different physiques in various surrounding environments.

References

[1]   M. Z. Win and R. A. Scholtz, "Characterization of ultra-wide bandwidth wireless indoor channels: a communication-theoretic view," *IEEE J. Select. Areas Commun.*, vol. 20, no. 9, pp. 1613-1627, Dec. 2002.

[2]   D. Porcino and W. Hirt, "Ultra-wideband radio technology: potential and challenges ahead," *IEEE Commun*, *Magazine*, vol. 41, no. 7, pp. 66-74, Jul. 2003.

[3]   S. Roy, J. R. Foerster, V. S. Somayazulu, and D. G. Leeper, "Ultrawideband radio design: the promise of high-speed, short-range wireless connectivity," in *Proc. IEEE*, vol. 92, no. 2, pp. 295-311, Feb. 2004.

[4]   Federal Communications Commission, "Revision of part 15 of the commission's rules regarding ultra-wideband tansmission systems," *First Report and Order*, FCC 02-48, Apr. 2002.

[5]   http://www.soumu.go.jp/s-news/2006/060327_3.html (In Japanese).

[6]   Y. Suzuki and T. Kobayashi, "Ultra wideband signal propagation in desktop environments," *IEICE Trans. Fundamentals*, vol. E88-A, no. 9, pp. 2272-2278, Sept. 2005.

[7]   T. Kobayashi, "Measurements and characterization of ultra wideband propagation channels in a passenger-car compartment," *IEICE Trans. Fundamentals*, vol. E89-A, no. 11, pp. 3089-3094, Nov. 2006.

[8]   United Nations, *World Population Prospects: The 2012 Revision*, United Nations, New York, NY, USA, 2013.

[9]   E. Jovanov, A. O'Donnell-Lords, D. Raskovic, P. Cox, R. Adhami, and F. Andrasik, "Stress monitoring using a distributed wireless intelligent sensor system," *IEEE Eng. Medicine Biol. Mag.*, vol. 22, no. 3, pp. 49–55, May/Jun. 2003.

[10] Y. Hao and R. Foster, "Topical review: Wireless body sensor networks for health-monitoring applications," *Physiol. Meas.*, vol. 29, no. 11, pp. R27–R56, Nov. 2008.

[11] M. Ghavami, L. B. Michael, and R. Kohno, *Ultra Wideband Signal and Systems in Communication Engineering, 2nd ed*. New York, NY: Wiley, 2007.

[12] A. F. Molisch, D. Cassioli, C.-C. Chong, S. Emami, A. Fort, B. Kannan, J. Karedal, J. Kunisch, H. G. Schantz, K. Siwiak, and M. Z. Win, "A comprehensive standardized model for ultrawideband propagation channels," *IEEE Trans. Antennas Propag.*, vol. 54, no. 11, pp. 3151-3166. Nov. 2006.

[13] T. Kobayashi and T. Nojima, "Liquid material simulating electromagnetic properties of

biological tissues at UHF bands," in *XXVIth General Assembly of the International Union of Radio Science*, Toronto, Ontario, Canada, Aug. 13-21, 1999.

[14]   G. Hartsgrove, A. Kraszewski, and A. Surowiec, "Simulated biological materials for electromagnetic radiation absorption studies," *Bioelectromagnetics*, vol. 8, no. 1, pp. 29-36, Jan. 1987.

[15]   C. K. Chou, G. W. Chen, A. W. Guy, and K. H. Luk, "Formulas for preparing phantom muscle tissue at various radiofrequencies," *Bioelectromagnetics*, vol. 5, no. 4, pp. 435-441, July 1984.

[16]   A. Alomainy, Y. Hao, X. Hu, C. G. Parini, and P. S. Hall, "UWB on-body radio propagation and system modeling for wireless body-centric networks," *IEE Proc. Commun.*, vol. 153, no. 1, pp. 107-114, Feb. 2006.

[17]   Y. Zhao, A. Alomainy, Y. Hao, and C. Parini, "UWB on-body radio channel modelling using ray theory and subband FDTD method," *IEEE Trans. Microwave Theory Tech.*, vol. 54, no. 4, pp. 1827-1835, 2006.

[18]   A. A. Goulianos, T. W. C. Brown, and S. Stavrou, "A novel path-loss model for UWB off-body propagation," in *Proc. IEEE 67th Veh. Tech. Conf. (VTC2008-Spring)*, Marina Bay, Singapore, pp. 450-454, May 11-14, 2008.

[19]   A. Fort, J. Ryckaert, C. Desset, P. D. Doncker, P. Wambacq, and L. V. Biesen, "Ultra-wideband channel model for communication around the human body," *IEEE J. Select. Areas Commun.*, vol. 24, no. 4, pp. 927-933, April 2006.

[20]   A. Fort, C. Desset, P. Wambacq, and L. V. Biesen, "Body area UWB RAKE receiver communication," in *IEEE Internat. Conf. Commun. (ICC 2006)*, Istanbul, Turkey, vol. 10, pp. 4682-4687, June 11-15, 2006.

[21]   A. Fort, C. Desset, P. D. Doncker, P. Wambacq, and L. V. Biesen, "An ultra-wideband body area propagation channel model - from statistics to implementation," *IEEE Trans. Microwave Theory Tech.*, vol. 54, no 4, pp. 1820-1826, June 2006.

[22]   A. Fort, C. Desset, P. D. Doncker, J. Ryckaert, P. D. Doncker, L. V. Biesen, and P. Wambacq, "Characterization of the ultra wideband body area propagation channel," in *Proc. IEEE Internat. Conf. on Ultra-Wideband, (ICUWB 2005)*, Zurich, Switzerland, Sept. 5-8, 2005.

[23]   T. Zasowski, F. Althaus, M. Stager, A. Wittneben, and G. Troster, "UWB for noninvasive wireless body area networks: channel measurements and results," in *Proc. 2003 IEEE Conf. Ultra Wideband Syst. Tech. (UWBST 2003)*, Reston, Virginia, USA, pp. 285-289, Nov. 16-19, 2003.

[24]   A. Alomainy, A. Sani, A. Rahman, J. G. Santas, and Y. Hao, "Transient characteristics of

wearable antennas and radio propagation channels for ultrawideband body-centric wireless communications," *IEEE Trans. Antennas Propag.*, vol. 57, no. 4, pp.875-884, April 2009.

[25] P. S. Hall and Y. Hao (eds.), *Antennas and Propagation for Body-Centric Wireless Communications*, Boston, MA: Artech House, 2006.

[26] Q. H. Abbasi, A. Sari, A. Alomainy, and Y. Hao, "Arm movements effect on ultra wideband on-body propagation channel and radio systems," in *Loughborough Antennas Propagat. Conf. (LAPC) 2009*, Loughborough, UK, Nov. 16-17, 2009.

[27] T. Kumpuniemi, T. Tuovinen, M. Hämäläinen, K. Y. Yazdandoost, R. Vuohtoniemi, and J. Iinatti, "Measurement-based on-body path loss modelling for UWB WBAN communications," in *7nd Internat. Symp. on Medical Information and Commun. Tech. (ISMICT 2013)*, Tokyo, Japan, Mar. 6-8, 2013.

[28] P. M. Izdebski, H. Rajagopalan, and Y. Rahmat-Samii, "Conformal ingestible capsule antenna: a novel chandelier meandered design," *IEEE Trans. Antennas Propag.*, vol. 57, no. 4, pp. 900-909, Apr. 2009.

[29] K. M.S. Thotahewa, J.-M. Redouté, and M. R. Yuce, "A UWB wireless capsule endoscopy device," in *36th Annual Internat. Conf. of the IEEE Engineering in Medicine and Biology Society (EMBC)*, pp. 6977-6980, Chicago, IL, USA, Aug. 26-30, 2014.

[30] T. Aoyagi, K. Takizawa, T. Kobayashi, J. Takada, K. Hamaguchi, and R. Kohno, "Development of an implantable WBAN path-loss model for capsule endoscopy," *IEICE Trans. Commun.*, vol. E93-B, no. 4, pp. 846-849, Apr. 2010.

[31] A. Khaleghi, R. Chavez-Santiago, and I. Balasingham, "Ultra-wideband statistical propagation channel model for implant sensors in the human chest," *IET Microw., Antennas, Propag.*, vol. 5, no. 15, pp. 1805-1812, Dec. 2011.

[32] A. Khaleghi, R. Chavez-Santiago, and I. Balasingham, "An improved ultra wideband channel model including the frequency-dependent attenuation for in-body communications," in *34th Annual Internat. Conf. of the IEEE Engineering in Medicine and Biology Society (EMBC)*, pp. 1631-1634, San Diego, CA, USA, Aug. 28-Spet. 1, 2012.

[33] D. Anzai, K. Katsu, R. Chavez-Santiago, Q. Wang, D. Plettemeier, J. Wang, and I. Balasingham, "Experimental evaluation of implant UWB-IR transmission with living animal for body area networks," *IEEE Trans. Microw. Theory Tech.*, vol. 62, no. 1, pp. 183-192, Jan. 2014.

[34] http://www.ntt-at.co.jp/product/sar/pdf/sar-p_141106.pdf (In Japanese).

[35] T. Onishi, R. Ishido, T. Takimoto, K. Saito, S. Uebayashi, M. Takahashi, and K. Ito,

"Biological tissue-equivalent agar-based solid phantoms and SAR estimation using the thermographic method in the range of 3-6 GHz," *IEICE Trans Commun.*, vol. E88-B, no. 9, pp. 3733-3741, Sept. 2005.

[36] D. Hara and T. Kobayashi, "Development of ultra wideband electromagnetic phantom materials for antennas and propagation studies," in *13th Conference on Microwave Techniques 2005*, Prague, Czech Republic, pp. 64-67, Sept. 26-28, 2005.

[37] S. Gabriel, R. W. Lau, and C. Gabriel, "The dielectric properties of biological tissues: II. Measurements in the frequency range 10 Hz to 20 GHz," *Phys. Med. Biol.*, vol. 41, no. 11, pp. 2251-2269, Nov. 1996.

[38] S. S. Stuchly, M. A. Rzepecka, and M. F. Iskander, "Permitivity measurements at microwave frequencies using lumped elements," *IEEE Trans. Instrum. Meas.*, vol. IM-23, no. 1, pp. 56-62, March 1974.

[39] J. J. Bowman, T. B. A. Senior and P. L. E. Uslenghi, *Electromagnetic and Acoustic Scattering from Simple Shapes*, Amsterdam, North-Holland, 1969.

[40] H. Yamamoto, J. Zhou, and T. Kobayashi, "Ultra wideband electromagnetic phantoms for antennas and propagation studies," *IEICE Trans. Fundamentals*, vol. E91-A, no. 11, pp. 3173-3182, Nov. 2008.

[41] Product information on 11 GHz MDD Fiber Optic Link, MITEQ Inc. http://amps.miteq.com/datasheets/MITEQ-MDD_-100M_11G.PDF.

[42] H. Yamamoto and T. Kobayashi, "Effects of feeding cable configurations on propagation measurements between small ultra wideband antennas for WBAN applications," in *Internat. Workshop on Future Wellness and Medical ICT Systems (FEELIT 2008)*, Lapland, Finland, Sept. 9, 2008.

[43] Skycross, Inc., Antenna Products, "3.1 - 10 GHz ultra-wideband antenna," http://www.skycross.com/Products/PDFs/SMT-3TO10M-A.pdf.

[44] T. Taniguchi, A. Maeda, and T. Kobayashi, "Development of an omnidirectional and low-VSWR ultra wideband antenna," *Internat. Journal on Wireless and Optical Commun.*, vol. 3, no. 2, pp. 145-157, Aug. 2006.

[45] Z. Kovacs, G. F. Pedersen, P. C. F. Eggers, and K. Olesen, "Ultra wideband radio propagation in body area network scenarios," *in 8th IEEE Int. Symp. on Spread Spectrum Techniques and Applications (ISSSTA 2004)*, Sydney, Australia, Aug. 30-Sep. 2, 2004.

[46] H. Ghannoum, C. Robin, and W. Bories, "Effects of antennas characteristics on UWB body area propagaton channel," *Int. J. on Wireless and Optical Commun.*, vol. 3, no. 2, pp. 203-212, 2006.

[47] H. Yamamoto, M. Koiwai, and T. Kobayashi, "Measurements and modeling of ultra-

wideband propagation losses around the human body dependent on room volume," *IEICE Trans. Fundamentals*, vol. E93-A, no. 12, pp. 2624-2633, Dec. 2010.

[48]   H. Yamamoto and T. Kobayashi, "Measurements and characterization of ultra wideband propagation channels between a base station and on-body antennas," in *2nd Internat. Symp. on Medical Information and Commun. Tech. (ISMICT 2007)*, Oulu, Finland, Dec. 11-13, 2007.

[49]   A. J. Goldsmith, *Wireless Communications*, New York: Cambridge Univ. Press, 2005.

[50]   H. Akaike, "Information theory as an extension of the maximum likelihood principle," in *Proc. 2nd Int. Inf. Theory Symp.*, pp. 267–281, 1973.

[51]   K. P. Burnham and D. R. Anderson, *Model Selection and Multi-Model Inference: A Practical Information – Theoretic Approach, 2nd ed.* New York, NY: Springer, 2002.

[52]   M. Hirose, H. Yamamoto, and T. Kobayashi, "Statistical modeling of ultra-wideband body-centric wireless channels considering room volume," *Intl. J. Antennas and Propag.*, vol. 2012, Dec.14, 2012.

[53]   A. F. Molisch et al., "IEEE 802.15.4a channel model - final report. Submitted to IEEE 802.15 WPAN low rate alternative PHY task group 4a (TG4a)," doc: IEEE 802.15.04-0662-01-004a, Nov., 2004.

[54]   C. Roblin, "On the separability of "on-body" and "off-body" clusters in the modeling of UWB WBAN channels for various indoor scenarios", in *Proc. of the 5th European Conference on Antennas and Propagation* (*EuCAP'11*), pp. 3148-3152, Apr. 2011.

[55]   A. M. Saleh and A. Valenzuela, "A statistical model for indoor multipath propagation," *IEEE J. Select. Areas Commun.*, vol. SAC-5, no 2, pp. 128-137, Feb. 1987.

[56]   Q. Wang, T. Tayamachi, I. Kimura, and J.Wang, "An on-body channel model for UWB body area communications for various postures," *IEEE Trans. Antennas Propag.*, vol. 57, no. 4, pp. 991-998, Apr. 2009.

[57]   Q. H. Abbasi, A. Sani, A. Alomainy, and Y. Hao, "Experimental characterization and statistical analysis of the pseudo-dynamic ultrawideband on-body radio channel," *IEEE AntennasWireless Propag. Lett.*, vol. 10, pp. 748-751, 2011.

[58]   Y. Qi, C. B. Soh, E. Gunawan, K.-S. Los, and A. Maskooki, "Measurement of knee flexion/extension angle using wearable UWB," in *35th Annual Internat. conf. of the IEEE Engineering in Medicine and Biology Society (EMBS)*, Osaka, Japan, July, 3-7, 2013.

[59]   D. Gaetano, P. McEvoy, M. J. Ammann, C. Brannigan, L. Keating, and F. Horgan, "On-body fidelity factor for footwear antennas over different ground materials," in *Proc. of the 8th European Conference on Antennas and Propagation* (*EuCAP'14*), pp. 1410-1414, Apr. 2014.

[60]   H. Yamamoto and T. Kobayashi, "Ultra wideband propagation loss model around the human body considering impact of room volume," in *32nd Internat. Conf. Telecommunications and Signal Processing (TSP)*, Dunakiliti, Hungary, Aug. 26-27, 2009.

[61]   M. M. Khan, M. A. Rahman, A. Alomainy, and C. Parini, "Ultra wideband on-body radio radio propagation channels study for different real human test subjects with various sizes and shapes," in *Proc of 2013 2nd Internat. Conf. on Advances in Electrical Engineering (ICAEE 2013)*, Dhaka, Bangladesh, Dec. 19-21, 2013.

[62]   M. Hirose and T. Kobayashi, "Wideband body-centric channels depending on bandwidths in various environments," in *IEEE Internat. Workshop onAntenna Technology (iWAT 2014)*, Sydney, Australia, Mar. 4-6, 2014.

Acknowledgments

I would like to acknowledge and thank all the people with whom I have had the sincere pleasure to collaborate in my academic pursuits. First and foremost, I would like to thank my supervisor, Professor Takehiko Kobayashi for his vision, support and encouragement. I would like to thank Professor Takao Matsumoto, Professor Yutaka Kaneda, Professor Tsuyoshi Suzuki, and Dr. Naohiko Iwakiri, who as the referees of my thesis, discussed the appropriateness of its contents. I would also like to thank the members of the Medical-ICT Group, the National Institute of Information and Communications Technology, Japan, for valuable input. I would like to thank Associate Professor David Ruzicka for correcting the English text.

I am grateful to the following students at Tokyo Denki University: Miyuki Hirose, Masato Koiwai, and Jian Zhou for valuable help in the experiments and discussions; and Yusuke Sekiwa, Tomonori Usami, Hideyuki Furumai, Keita Hisamori, and Masaki Toda for supporting measurements. I also would like to thank Dr. Satoshi Kouya and the other members of the Wireless Systems Laboratory.

Finally, I want to thank my grandparents, my parents, my brother and his family, my wife, Akiha Yamamoto, and her family, for their continued support. This dissertation is dedicated to them.

Appendix A
# Numerical Evaluation of Effects of Errors in the Complex Relative Permittivity of Phantom Materials

The effects of errors in the $\dot{\varepsilon}$ of phantom materials in comparison with muscle on reflection were numerically evaluated [36]. First, the UWB power reflection coefficients were calculated with and without errors in $\dot{\varepsilon}(f) = \varepsilon'(f) - j\varepsilon''(f)$ against $\dot{\varepsilon}_{\text{muscle}}(f) = \varepsilon'_{\text{muscle}}(f) - j\varepsilon''_{\text{muscle}}(f)$, where $\dot{\varepsilon}_{\text{muscle}}(f)$ denotes the relative permittivity of high-water-content tissues, including muscle, for which data were tabulated by Gabriel et al. [37].

When $\varepsilon' = (1 + z_1) \varepsilon'_{\text{muscle}}$ and/or $\varepsilon'' = (1 + z_2) \varepsilon''_{\text{muscle}}$, where z_1 and z_2 represent errors, the maximum and rms errors in the UWB power reflection coefficients were calculated, as shown in Fig. A.1. The maximum errors for TM and TE incidence occurred near the Brewster angle and at the incident angle of 0°, respectively. While the TM maximum errors near the Brewster angle ($\approx 82°$) were relatively large, the TE maximum errors and the TM and TE rms errors (over the incident angle through 0° to 90°) were notably small, when $|z_1|$ and $|z_2|$ were less than 30%. Tolerable margins of error in ε' were smaller than those in ε''. When $\varepsilon'(f) = (1 + z_3 \, g(f)) \, \varepsilon'_{\text{muscle}}(f)$ and/or $\varepsilon'' = (1 + z_4 \, g(f)) \, \varepsilon''_{\text{muscle}}(f)$, where $g(f) = ((f - 6.85 \text{ GHz}) / 3.75 \text{ GHz})$; namely the curves for ε' and/or ε'' crossed those for $\varepsilon'_{\text{muscle}}$ and/or $\varepsilon''_{\text{muscle}}$, and the resulting errors in the UWB reflection coefficients were almost negligible when $|z_3|$ and $|z_4|$ were less than 30%.

Next, the distortions of UWB waveforms reflected from a planar infinite medium with errors in $\dot{\varepsilon}$ were evaluated. The incident waveform was a Gaussian modulated impulse, as shown in Fig. 2.4. Representative correlation coefficients between the reflected waveforms from the medium with and without errors in $\dot{\varepsilon}$ are shown in Fig. A.2. The correlation coefficients were greater than 0.995 when $|z_i| < 30\%$ ($i = 1, 2, 3, 4$). The waveform distortion was therefore substantially negligible.
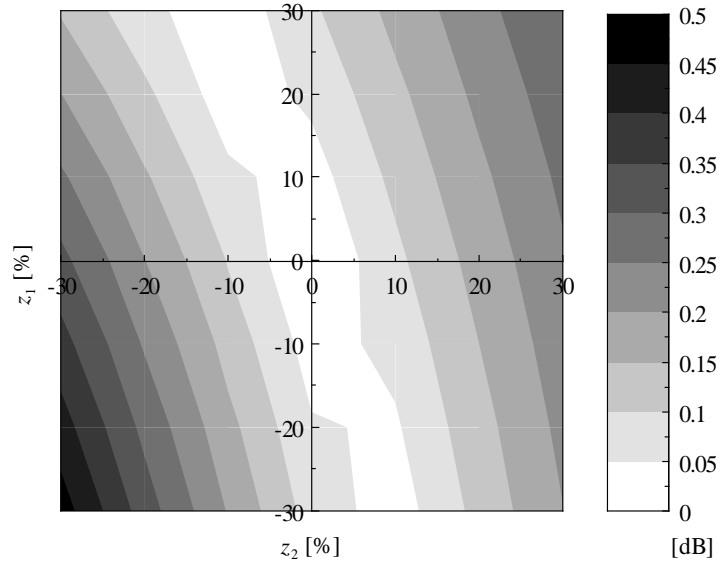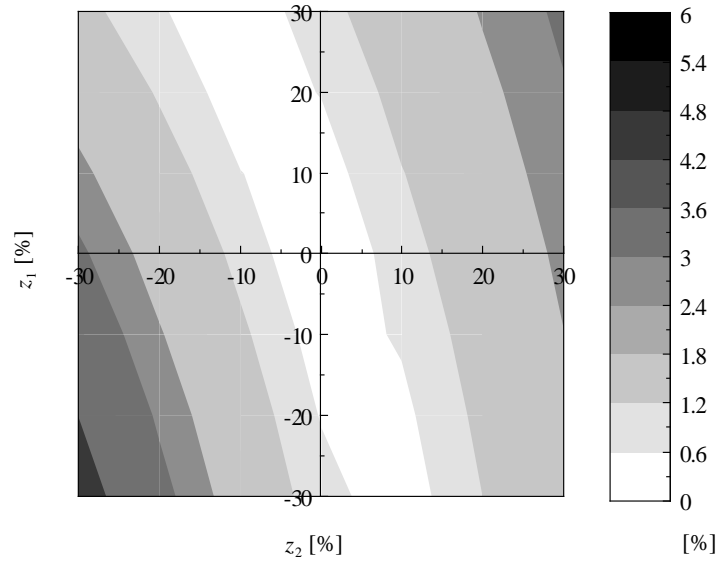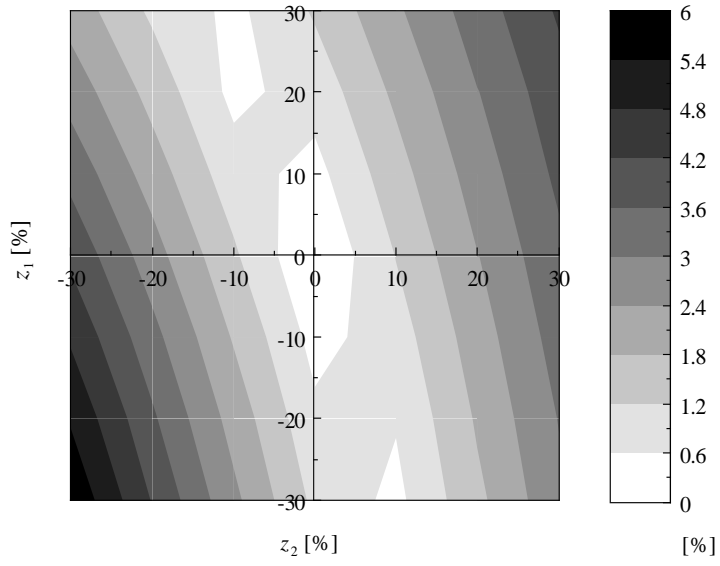
(a)
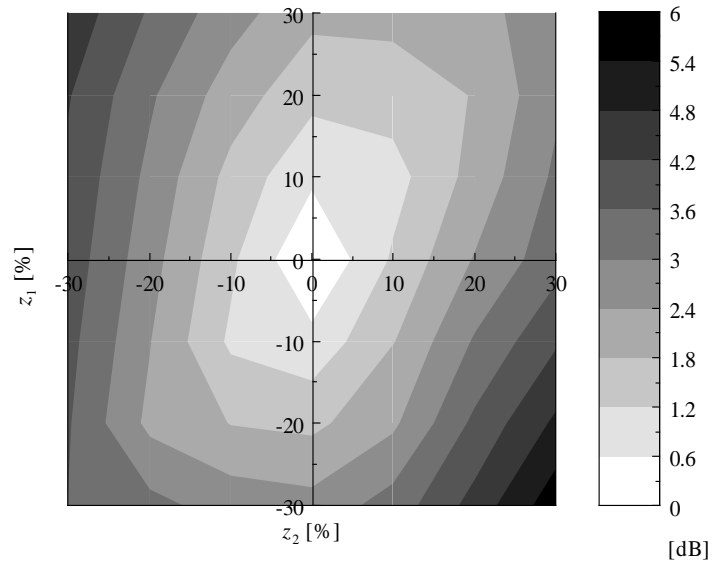
(b)

Fig. A.1.   Errors in plane-wave UWB power reflection coefficients from planar infinite homogeneous media with errors in $\dot{\varepsilon}$: maximum errors: (a) TE and (b) TM incidence; and rms errors: (c) TE and (d) TM incidence.
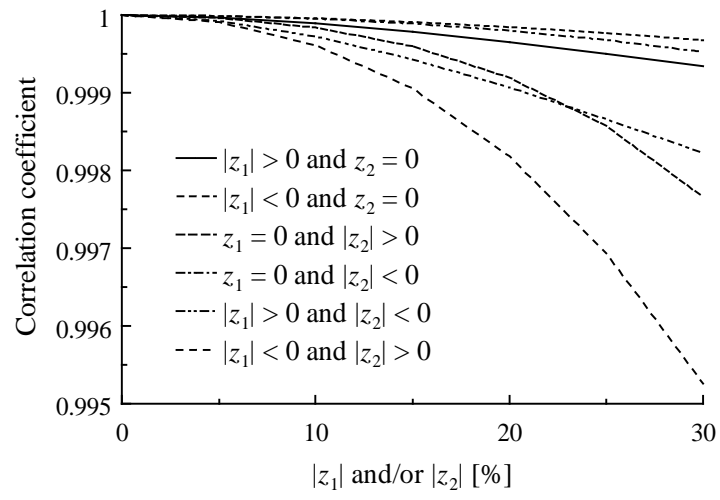
(c)

(d)

Fig. A.1.   Continued.

Fig. A.2. The correlation coefficients of the reflected waveforms from media with and without errors in $\dot{\varepsilon}$.

The legend in the figure reads:

— $|z_1| > 0$ and $z_2 = 0$

--- $|z_1| < 0$ and $z_2 = 0$

---- $z_1 = 0$ and $|z_2| > 0$

—·— $z_1 = 0$ and $|z_2| < 0$

—··— $|z_1| > 0$ and $|z_2| < 0$

--- $|z_1| < 0$ and $|z_2| > 0$

The y-axis is labeled "Correlation coefficient" and the x-axis is labeled $|z_1|$ and/or $|z_2|$ [%].

Appendix B
Examples of Propagation Losses along the Center Axes of the Human Body

This chapter describes frequency- and time-domain propagation losses along the center axis of the human torso. Figure B.1 presents the propagation losses corresponding with the measured positions. The UWB propagation losses were calculated by Eq. (4.1), and listed as follows:

· In the case of $n = 0$

	UWB propagation loss [dB]				
	Room A	Room B	Room C	Room D	Room E
NLOS	81	70	70	57	51
LOS	59	60	59	49	46

· In the case of $n = 1$

	UWB propagation loss [dB]				
	Room A	Room B	Room C	Room D	Room E
NLOS	79	70	69	57	51
LOS	54	55	49	45	45

· In the case of $n = 2$

	UWB propagation loss [dB]				
	Room A	Room B	Room C	Room D	Room E
NLOS	76	70	66	55	50
LOS	42	56	42	42	43

· In the case of $n = 3$

	UWB propagation loss [dB]				
	Room A	Room B	Room C	Room D	Room E
NLOS	81	68	66	49	51
LOS	40	36	32	35	36

・ In the case of $n = 4$

	UWB propagation loss [dB]				
	Room A	Room B	Room C	Room D	Room E
NLOS	74	64	64	56	53
LOS	-	-	-	-	-

・ In the case of $n = 5$

	UWB propagation loss [dB]				
	Room A	Room B	Room C	Room D	Room E
NLOS	74	65	65	54	52
LOS	28	35	35	37	34

・ In the case of $n = 6$

	UWB propagation loss [dB]				
	Room A	Room B	Room C	Room D	Room E
NLOS	78	63	63	54	52
LOS	43	51	39	48	45

The UWB propagation losses decreased with the decreasing room volume regardless of the measured positions and of whether it was a case of NLOS or LOS, as described in Section 4.3.
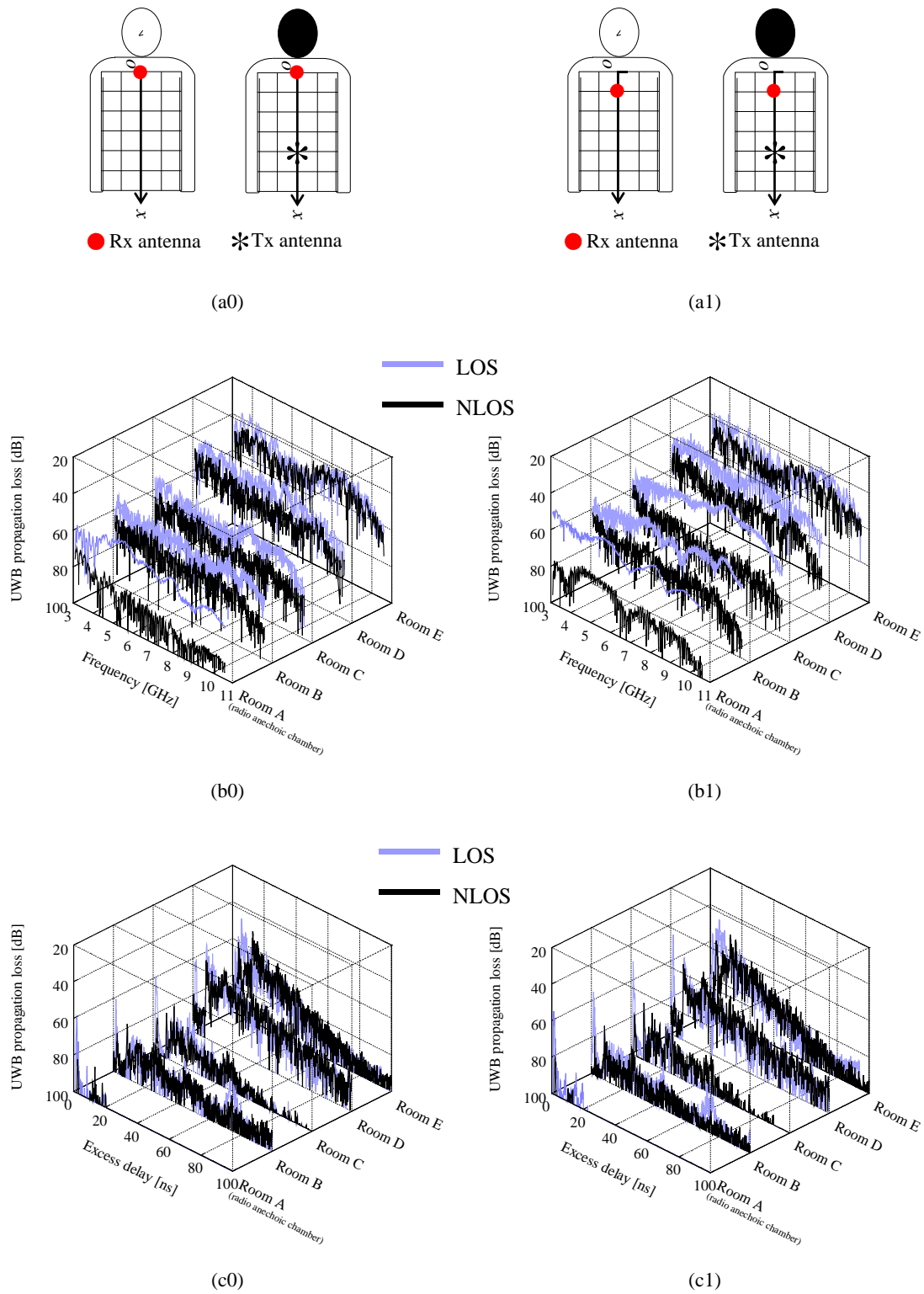
Fig. B.1.   Propagation losses at the front (NLOS) and the back (LOS) bodies on the center axes: (a*n*) Tx and Rx positions, (b*n*) frequency and (c*n*) time domains for $x = n \times 100$ mm.
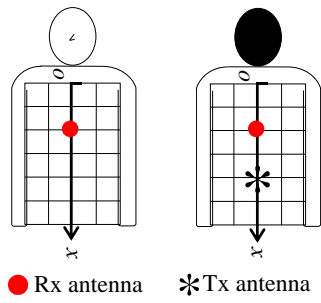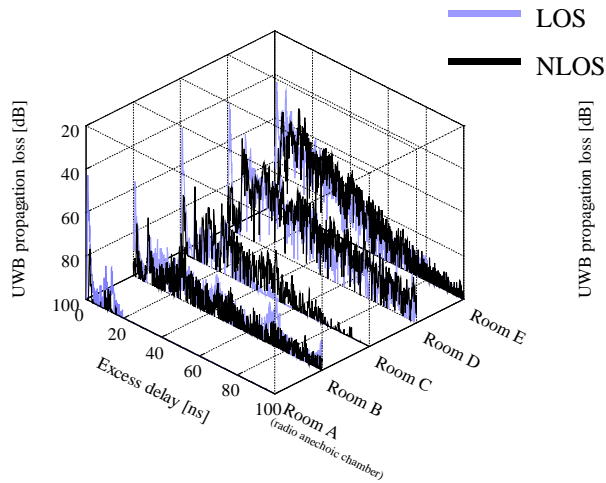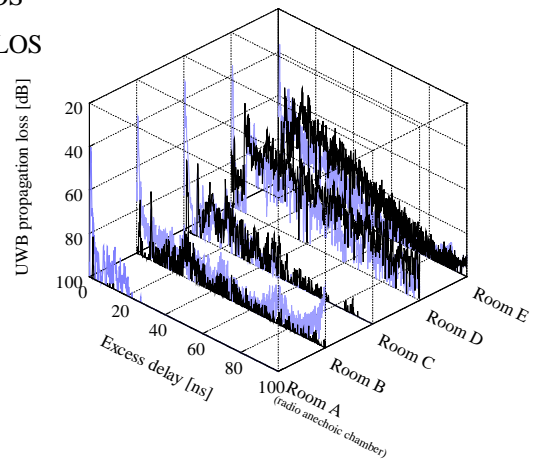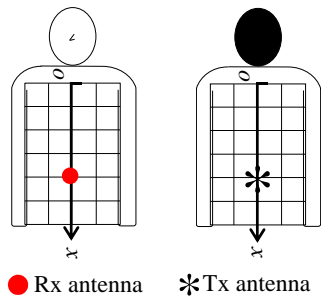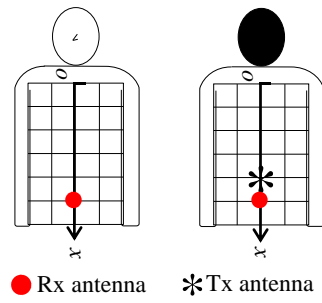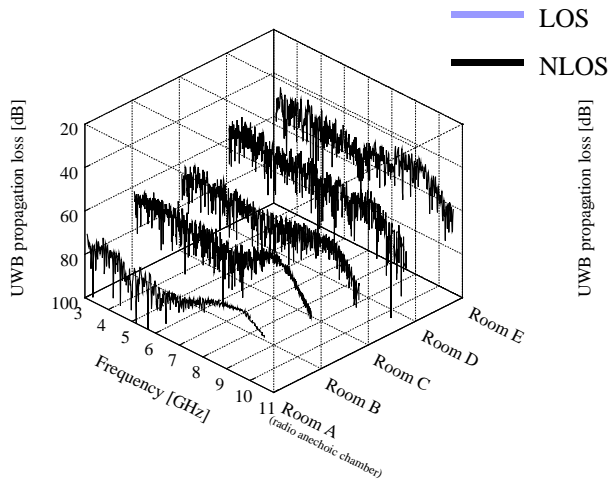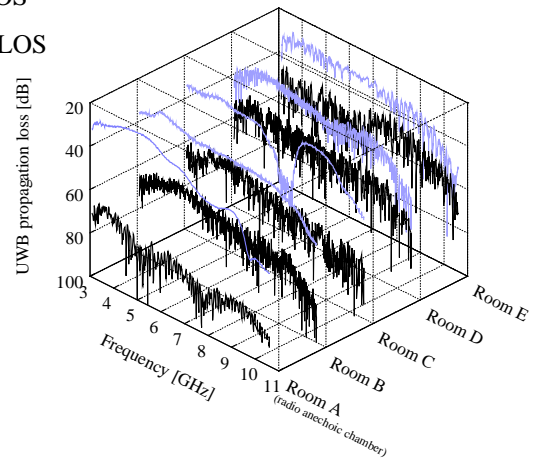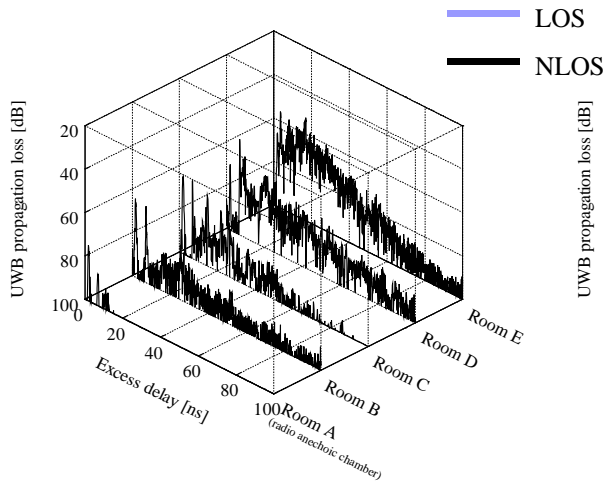
(a2)
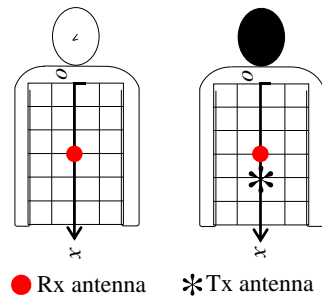
(a3)
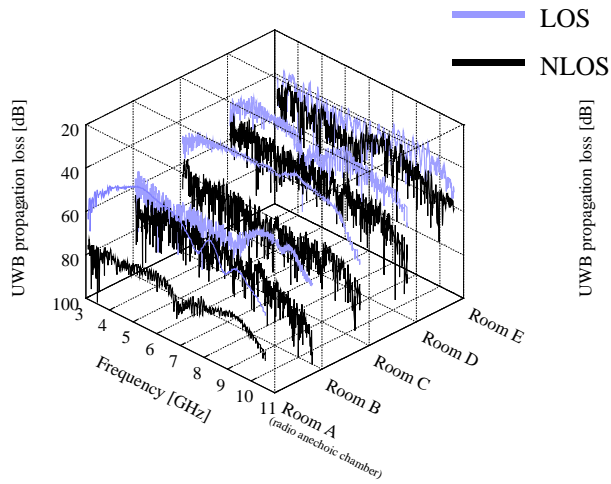
(b2)
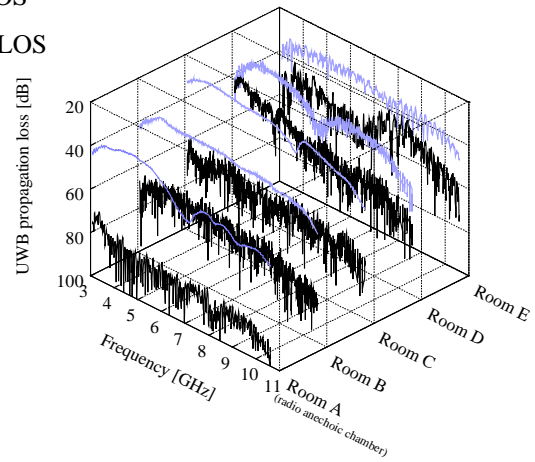
(b3)

(c2)

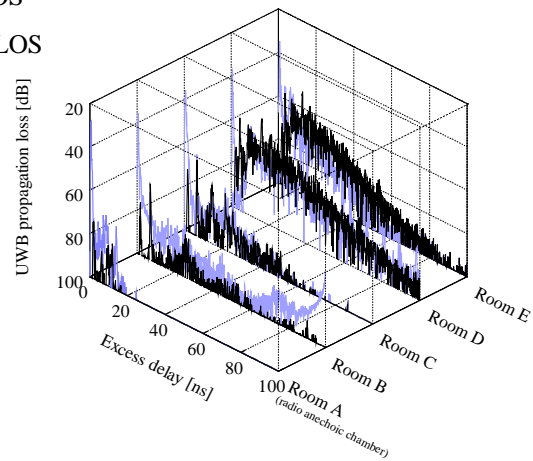(c3)

Fig. B.1.   Continued.

(a4)

(a5)

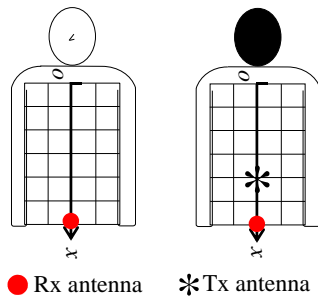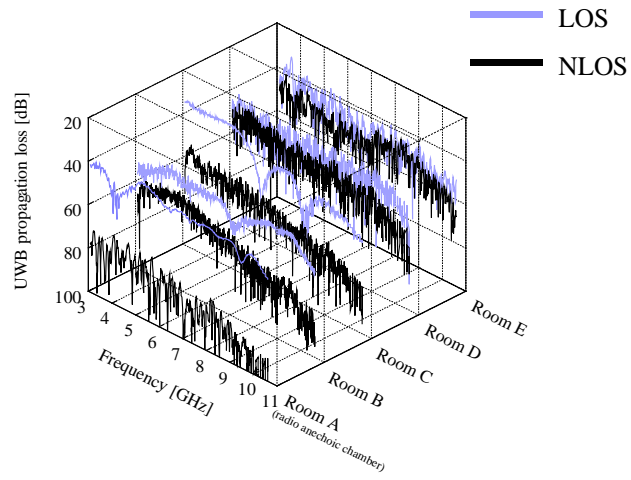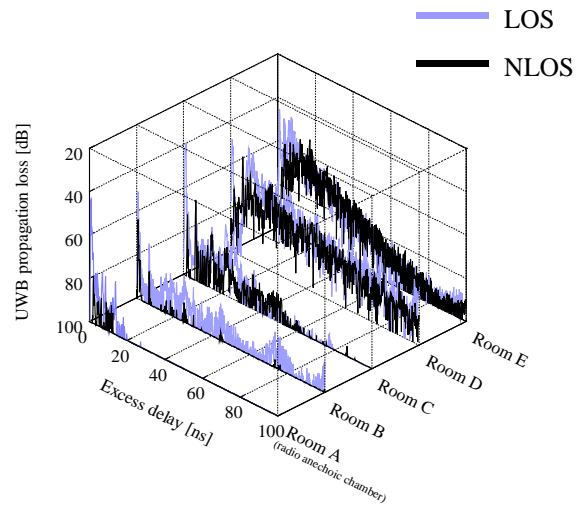(b4)

(b5)

(c4)

(c5)

Fig. B.1.   Continued.

(a6)

(b6)

(c6)

Fig. B.1.   Continued.

Appendix C
Reception Power Versus Occupied Bandwidth

UWB transmission is expected to alleviate the frequency variation in reception power. In this chapter, UWB propagation losses around the human body were characterized in comparison with narrowband. The UWB propagation loss was calculated by integrating the power frequency response from 5.35 to 8.35 and 3.1 to 10.6 GHz, and continuous wave (CW) at 6.85 GHz was extracted therefrom. The spatial distributions of CW (6.85 GHz), and UWB (5.35 to 8.35 and 3.1 to 10.6 GHz) propagation losses in the five environments are shown in Figs. C.1 and C.2. The performances of the propagation loss were as follows:

In the case of LOS:

- In Room A (a radio anechoic chamber), the maximum, minimum, and median propagation losses of CW differed to within 2 dB in comparison with UWB (5.35 to 8.35 and 3.1 to 10.6 GHz).
- In Rooms B to E (multipath environments), while CW generated dead spots at several points caused by multipath, UWB yielded no dead spots.

In the case of NLOS:

- In Room A, CW resulted in more than 90-dB propagation loss at several points. The maximum propagation losses for UWB (5.35 to 8.35 and 3.1 to 10.6 GHz) were 86 and 81 dB, respectively.
- In Rooms B to E, while CW generated dead spots at several points caused by multipath, UWB yielded no dead spots.

Next, fading depth versus frequency bandwidth at the deepest dead spot in each room was derived from the measured data, as shown in Fig. C.3. The center frequency was fixed at 6.85 GHz and the bandwidth changes at 0.5 (from 6.6 to 7.1), 1 (from 6.35 to 7.35), 1.5 (from 6.1 to 7.6), 3 (from 5.35 to 8.35), and 7.5 (from 3.1 to 10.6) GHz. The 7.5-GHz bandwidth propagation loss was set to the 0-dB reference. The wider bandwidth yielded higher reception power regardless of the room volume, or whether the propagation was NLOS or LOS. In [62], fading depth was also evaluated. The center frequency was fixed at 6.85 GHz and the bandwidth changes at 0.01, 0.02, 0.05, 0.1, 0.15, 0.5, and 1 GHz. The wider bandwidth also yielded higher

reception power. These results indicated that UWB technologies are advantageous over narrowband from the viewpoint of reducing fading margins.
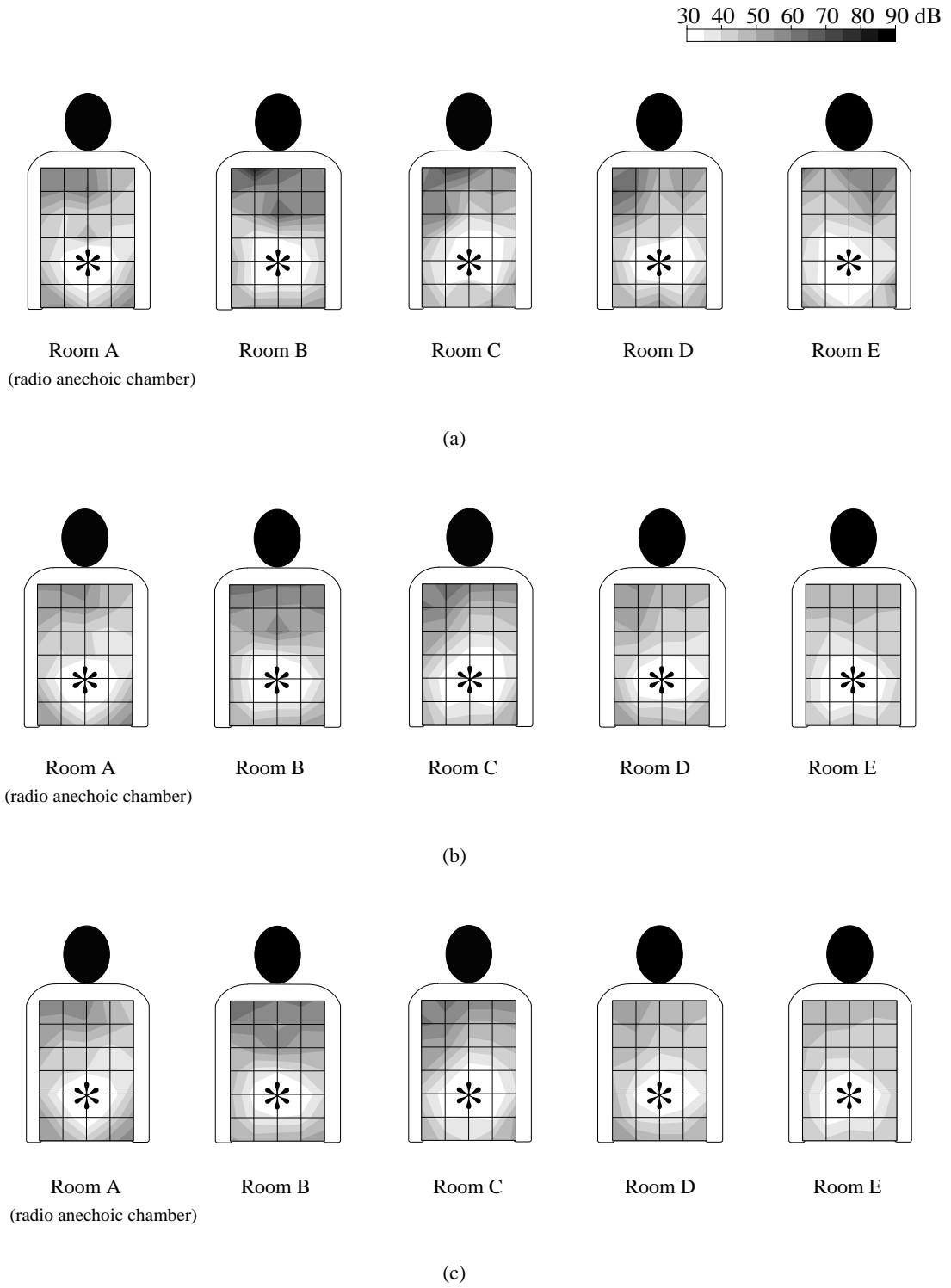
Fig. C.1.   Spatial distributions of UWB propagation losses for LOS in the five environments: (a) CW (6.85 GHz), (b) UWB (5.35 to 8.35 GHz), and (f) UWB (3.1 to 10.6 GHz). The transmitting antenna was placed at a point denoted by *.

113

Room A
(radio anechoic chamber)

Room B

Room C

Room D

Room E

(a)

Room A
(radio anechoic chamber)

Room B

Room C

Room D

Room E

(b)

Room A
(radio anechoic chamber)
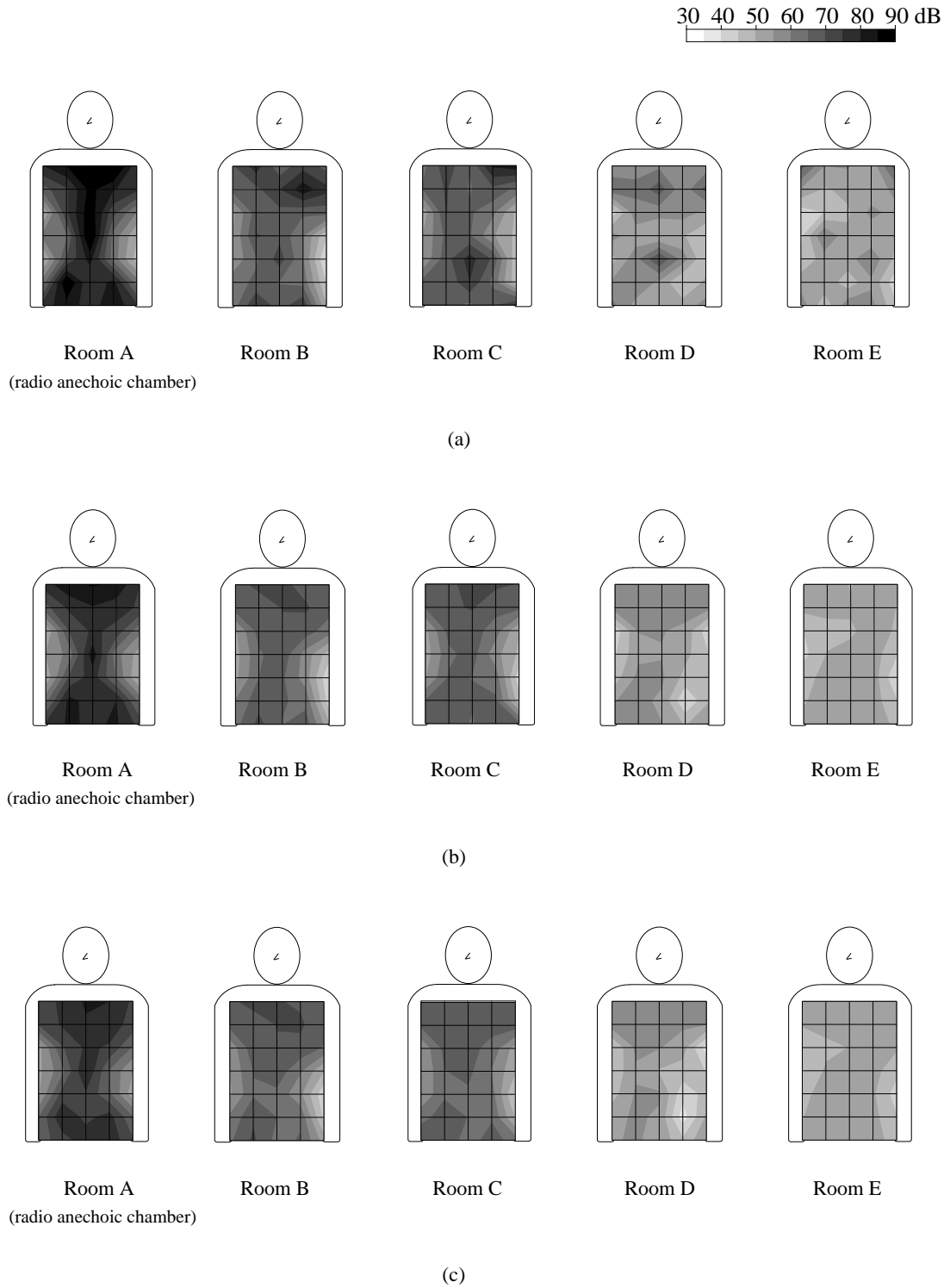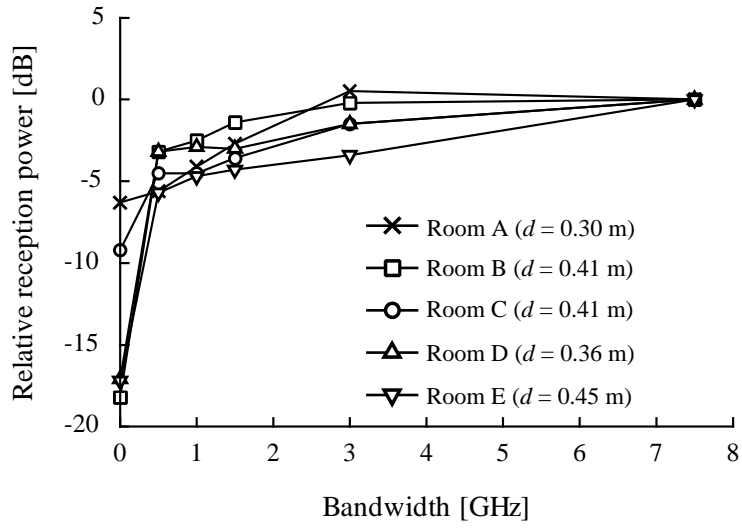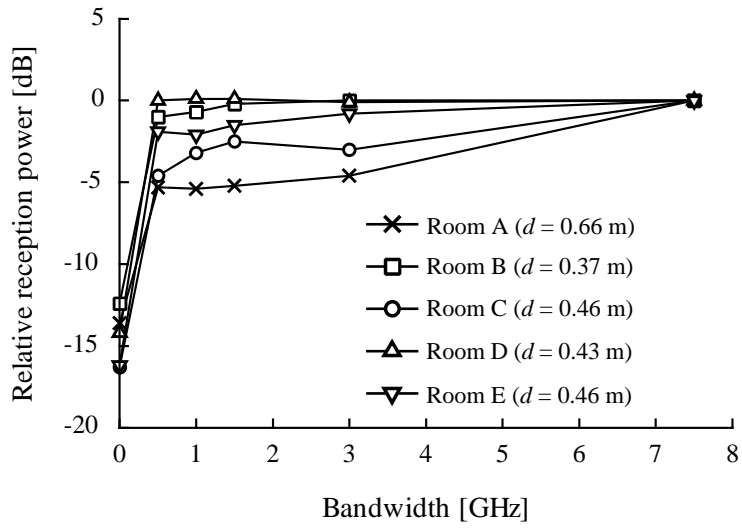
Room B

Room C

Room D

Room E

(c)

Fig. C.2. Spatial distributions of UWB propagation losses for NLOS in the five environments: (a) CW (6.85 GHz), (b) UWB (5.35 to 8.35 GHz), and (f) UWB (3.1 to 10.6 GHz). The transmitting antenna was placed at a point denoted by *.

(a)

(b)

Fig. C.3.   Fading depth versus occupied bandwidth at the deepest dead spot: (a) LOS and (b) NLOS.

Appendix D
List of Publications and Awards

Journal Papers

[1] M. Hirose, H. Yamamoto, and T. Kobayashi, "Statistical modeling of ultra-wideband body-centric wireless channels considering room volume," *Intl. J. Antennas and Propag.*, vol. 2012, Dec.14, 2012.

[2] H. Yamamoto, M. Koiwai, and T. Kobayashi, "Measurements and modeling of ultra-wideband propagation losses around the human body dependent on room volume," *IEICE Trans. Fundamentals*, vol. E93-A, no. 12, pp. 2624-2633, Dec. 2010.

[3] H. Yamamoto, J. Zhou, and T. Kobayashi, "Ultra wideband electromagnetic phantoms for antennas and propagation studies," *IEICE Trans. Fundamentals*, vol. E91-A, no. 11, pp. 3173-3182, Nov. 2008.

Book Chapter

[1] H. Yamamoto and T. Kobayashi, "Ultra wideband propagation loss around a human body in various surrounding environments," in F. Sabath et al. (eds.), *9th Ultra-Wideband, Short-Pulse Electromagnetics 9 (UWB SP9)*, Springer, New York, NY, USA, Apr. 2010.

International Conferences

[1] H. Yamamoto and T. Kobayashi, "Ultra wideband propagation loss models dependent on room volume for wireless body area networks," in *the 4th Internat. Symp. on Medical Information and Commun. Tech. (ISMICT 2010)*, Taipei, Taiwan, Mar. 22-25, 2010.

[2] H. Yamamoto and T. Kobayashi, "Ultra wideband propagation loss model around the human body considering impact of room volume," in *32nd Internat. Conf.*

Telecommunications and Signal Processing (TSP), Dunakiliti, Hungary, Aug. 26-27, 2009.

[3] H. Yamamoto and T. Kobayashi, "Ultra wideband radio propagation around a human body in various surrounding environments," in *IEEE Antennas Propagat. Soc. Symp. (AP-S 2009)*, Charleston, SC, USA, Jun. 1-5, 2009.

[4] H. Yamamoto and T. Kobayashi, "Effects of feeding cable configurations on propagation measurements between small ultra wideband antennas for WBAN applications," in *Internat. Workshop on Future Wellness and Medical ICT Systems (FEELIT 2008)*, Lapland, Finland, Sep. 9, 2008.

[5] H. Yamamoto and T. Kobayashi, "Ultra wideband propagation loss around a human body in various surrounding environments," in *9th Ultra-Wideband, Short-Pulse Electromagnetics Conference (UWB SP9)*, Lausannne, Switzerland, Jul. 21-25, 2008.

[6] H. Yamamoto and T. Kobayashi, "Measurements and characterization of ultra wideband propagation channels between a base station and on-body antennas," in *the 2nd Internat. Symp. on Medical Information and Commun. Tech. (ISMICT 2007)*, Oulu, Finland, Dec. 11-13, 2007.

Domestic Conferences (all in Japanese)

[1] 山本浩延, 小林岳彦, "測定環境の体積の影響を考慮した人体周辺の UWB 伝搬損失モデル," 信学ソ大, A-5-14, Sep. 15-18, 2009.

[2] 山本浩延, 小林岳彦, "測定環境の体積の影響を含む人体周辺の UWB 伝搬損失モデル," 電子情報通信学会医療情報通信技術時限研究専門委員会, no. 9, pp. 139-148, Jul. 28, 2009.

[3] 山本浩延, 小林岳彦, "様々な実環境における人体周辺の UWB 電波伝搬ロスモデル," 信学総大, BS-1-5, Mar. 17-20, 2009.

[4] 山本浩延, 小林岳彦, "WBAN アプリケーションのための小型 UWB アンテナ間の電波伝搬実験におけるケーブル配置の影響," 電子情報通信学会医療情報通信技術時限研究専門委員会, no. 7, pp. 39-45, Jan. 13, 2009.

[5] 山本浩延, 小林岳彦, "基地局および人体装着アンテナ間伝搬チャネルの実測と等価アンテナ利得による評価," 電子情報通信学会医療情報通信技術時限研究専門委員会, no. 4, pp. 80-86, Jan. 11, 2008.

[6] 山本浩延, 西出剛彦, 小林岳彦, "車載レーダに検知されやすい遊戯用ボールの提案," 第 5 回 TDU アイディアコンテスト, 東京電機大学, Dec. 8, 2007.

[7] 山本浩延, 西出剛彦, 小林岳彦, "自動車レーダに検知されやすい遊戯用ボール," IEEE Tokyo Young Researchers Workshop, 東京工業大学 大岡山キャンパス, Dec. 7, 2007.

Patent

特許:　　　「遊戯用ボール」
　　　　　　登録番号: 特許第 5142366 号, 平成 24 年 11 月 30 日登録
米国:　　　「Game Ball」
　　　　　　登録番号: U. S. Patent No. US7,976,416B2, 平成 21 年 7 月 12 日登録

Awards

[1] WBS Student Paper Award, IEICE Transactions on Fundamentals, Special Section on Wideband Systems, Dec. 2010.
　　　　Journal Paper [2] に対する受賞

[2] 東京電機大学平成 21 年度学長賞(工学研究科修士課程情報通信工学専攻総代), Mar. 18, 2010.

[3] 東京電機大学平成 19 年度学長賞(工学部第一部情報通信工学科総代), Mar. 18, 2008.

[4] 東京電機大学工学部平成 19 年度学部長賞, Mar. 14, 2008.

    International Conference [6] に対する受賞

[5] 東京電機大学工学部平成 19 年度学部長賞, Mar. 14, 2008.

    Award [7] に対する受賞

[6] 第 5 回 TDU アイディア・コンテスト奨励賞, Dec. 8, 2007.

    Domestic Conference [6] に対する受賞

[7] The 4th IEEE Tokyo Young Researchers Workshop 三菱電機(株) Changes for the Better 賞, Dec. 7, 2007.

    Domestic Conference [7] に対する受賞